Title
Spiral Shock and Feathering Instability in Spiral Arms /

Author
Lee, Wing Kit

Publication Date
2013

Peer reviewed|Thesis/dissertation

UNIVERSITY OF CALIFORNIA, SAN DIEGO

Spiral Shock and Feathering Instability in Spiral Arms

A dissertation submitted in partial satisfaction of the
requirements for the degree
Doctor of Philosophy

in

Physics

by

Wing Kit Lee

Committee in charge:

Professor Frank H. Shu, Chair
Professor Leo Blitz
Professor Patrick H. Diamond
Professor Michael L. Norman
Professor William R. Young

2013

The dissertation of Wing Kit Lee is approved, and it is acceptable in quality and form for publication on microfilm and electronically:

Chair

University of California, San Diego

2013

DEDICATION

To my family and my cats.

EPIGRAPH

If you wish to make an apple pie from scratch,
you must first invent the universe.
—Carl Sagan

TABLE OF CONTENTS

LIST OF FIGURES

LIST OF TABLES

ACKNOWLEDGMENTS

It is my pleasure to have the opportunity to meet many great scientists, astronomers, and astrophysicists during my years in the graduate school. I would like to thank my advisor, Frank Shu for his guidance and support. Although part of my thesis work was done after his retirement, his teaching went beyond academic meetings. I am very grateful to have had the opportunity to learn part of his accomplishments in Astrophysics. In addition, I would like to acknowledge various kinds of support from Academia Sinica's Institute of Astronomy and Astrophysics (ASIAA), Taiwan.

I would also like to thank Pat Diamond for his patient and trust on an average student in his class. His class in Plasma is truly an enlightenment to me. I also thank Mike Norman for introducing me to the high-performance and parallel computing.

There are also many great teachers at UCSD that I would like to thank: David Tytler, Art Wolfe, Kim Griest, George Fuller, and Hans Paar. I met some of them when I was an undergraduate exchange student in 2005. They were my teachers when I first came to the United States and had a great influence on me to pursue graduate study.

I am very thankful to Ron Allen for his help, support, and encouragement.

In these years, I enjoyed very much the discussion with Aaron Day, Pei-Chun Hsu, Geoffery So, Woong-Tae Kim, Steve Lubow, Hsiang-Hsu Wang, Lien-Hsuan Lin, and Ka-Hei Law.

I would like to thank my friend Sze-Leung Cheung, who introduced me to Astronomy when I was 12 and had a great influence on me to be an astronomer. I cannot imagine I would go this far in academia without meeting him. Because of him, stargazing becomes my life-long hobby, if not considered as a professional skill in this field. I also thank a few people I met during the high-school years: O.S. Yan, Kennith Hui, C.K. Man, Mr P.K. Fung, and Mr S.K. Leung.

Special thanks to my unofficial undergraduate advisor, Dr M.-C. Chu for his tremendous support during my college years. He becomes a role model for many of us at CUHK because of his patient and generosity in spending time with students. I also thanks many friends from the college years who give unconditional support in various ways when we are studying in a foreign country.

I have enjoyed many friendships I developed during my years in San Diego.

Although I could not list all the names here, they certainly made my life much easier in the graduate school. In particular, I thank Steven O.S. Pak for bring all fun and joy into any kind of technical and non-technical discussions. Lastly, I would like to thank Mandy Cheung who taught me how to cook and how to enjoy many aspects in life.

Finally, I am deeply grateful to my parents.

Chapter 2, in full, is a reprint of the material as it appears in Astrophysical Journal, 2012, 756, 45. Lee, Wing-Kit; Shu, Frank. The dissertation author was the primary investigator and author of this paper.

Chapter 3, in full, is currently being prepared for submission for publication of the material. Lee, Wing-Kit. The dissertation author was the primary investigator and author of this material.

VITA

2007	B. Sc. in Physics, Chinese University of Hong Kong
2007-2013	Teaching Assistant, University of California, San Diego
2009	M. Sc. in Physics, University of California, San Diego
2013	Ph. D. in Physics, University of California, San Diego

PUBLICATIONS

Wing-Kit Lee and Frank H. Shu, "Feathering Instability in Spiral Arms. I. Formulation of the Problem.", ApJ, 2012, 756, 45

FIELDS OF STUDY

Major Study: Physics

Studies in Stellar Structure and Interstellar Medium
Professor Frank Shu

Studies in Plasma Physics
Professor Patrick Diamond

Studies in General Relativity
Professors Kim Griest and George Fuller

Studies in Parallel Computing
Professor Michael Norman

Studies in Cosmology
Professor David Tytler

Studies in Quantum Mechanics and Quantum Field Theory
Professors Lu Sham and Elizabeth Jenkins

ABSTRACT OF THE DISSERTATION

Spiral Shock and Feathering Instability in Spiral Arms

by

Wing Kit Lee

Doctor of Philosophy in Physics

University of California, San Diego, 2013

Professor Frank H. Shu, Chair

A theoretical framework is developed to understand the feathering substructures along spiral arms by considering the perturbational gas response to a spiral shock. Feathers are density fluctuations that jut out from the spiral arm to the interarm region at large pitch angles. In a localized asymptotic approximation, related to the shearing sheet except that the inhomogeneities occur in space rather than in time, we derive the linearized perturbation equations for a razor-thin disk with turbulent interstellar gas, frozen-in magnetic field, and gaseous self-gravity. In the addition to the formulation, we investigate how individual normal modes of the system depend on seven dimensionless quantities that characterize the underlying time-independent axisymmetric state plus its steady, nonlinear, two-armed spiral-shock response to a hypothesized background density wave supported by the disk stars of the galaxy. In a particular case using galactic

parameters at the inner part of M51 galaxy, we show that the normal mode with the maximum growth rate has the wavelength along the spiral arm that matches the observation of spacing of the feathers at around 500 pc. We also demonstrate that the self-gravity is an important parameter governing the feathering instability.

Chapter 1

Overview

1.1 Spiral Shocks in Galaxies

The large scale gas flow in a grand-design spiral galaxy is mostly circular, except in regions near some non-axisymmetric structures such as spiral arms or bar. The gaseous streaming motion, which is the deviation of the gas velocity from the circular flow, can be used to measure the effects of the spiral density wave. Roberts (1969) first showed in his time-independent non-linear calculation that, depending on the strength of the stellar component of the spiral density wave, the gas can be accelerated into supersonic speed and eventually form a shock when the gas streamlines are assumed to be closed as it circulates around the galaxy. This gaseous shock in galactic scale, which is located near the stellar spiral arm in most situations, allows great compression of gas and is thought to have an important role in the formation of the giant molecular clouds (GMCs) around the spiral arm (Shu et al. 2007). Shu et al. (1973) investigated the gas response due to the static, tight-winding stellar spiral gravitational forcing of various strengths, and found that the galactic spiral shock can be formed even if the amplitude of such spiral forcing is small. This is because the effective sound speed of the gas is of the same order as the velocity perturbation of the gas due the spiral arm. Such a scenario is illustrated in Figure 1.1. In the rotating frame of the stellar spiral pattern, the gas enters the spiral arm, accelerates into supersonic speed under the gravitational attraction due to the concentration of stars and gas, and eventually forms a shock. The post-shock gas is subsonic and gradually accelerates again when leaving from one spiral arm and moving towards the next. The relative gas surface density is inversely proportional to the perpendicular gas velocity due to the mass continuity, and so it has the highest compression downstream of the shock.

The research on the spiral shock in this thesis is based on the framework in Shu et al. (1973) and it is extended to incorporate the effects of magnetic field and self-gravity of the gas. In the scale of spiral arms, the mean interstellar ordered magnetic field is a few micro-gauss and provides additional pressure to thermal and/or turbulent pressure because of its alignment with the spiral arm (Roberts & Yuan 1970). The steady-state magnetized spiral shock profile is similar, but decreases in strength when the Alfv́en's speed is high (c.f., Chapter 2, Lee & Shu (2012)). On the other hand, the calculation of the gaseous self-gravity is more complex due to the requirement to obtain a self-consistent solution of the Poisson equation and magnetohydrodynamics equations. Nevertheless, we are able to show in Lee & Shu (2012) that the self-gravity enhances the compression of the gas at the shock and also pushes the shock location downstream, which is consistent with quasi-one-dimensional numerical simulations (e.g., Kim & Ostriker 2002). Therefore, in general, the spiral shock compression is enhanced with higher mean gas surface density or weaker magnetic field.

1.2 Spiral Substructure and Feathers

Advances in the imaging technology allow us to explore the substructure of spiral arms. In addition to the primary dust lane which indicates the gas shock in the spiral arm, thin dark dust lanes are found jutting out at a large angle or perpendicularly into the interarm region and are called feathers (Lynds 1970). These feathers have little or no massive star formation as opposed to the self-luminous "spurs" and "pearls" that are found to associate with OB associations and HII regions in the spiral arm (Elmegreen 1980). Feathers, an extinction feature in the optical images (e.g., dark dust lanes seen in the *HST* image of M51), are found to be common among spiral galaxies (La Vigne et al. 2006) and coincide with molecular gas from studies of CO emissions (Corder et al. 2008). Therefore, it is interesting to find out how these density fluctuations relate to the dynamics of the spiral arm where they originate, and ultimately to other substructures

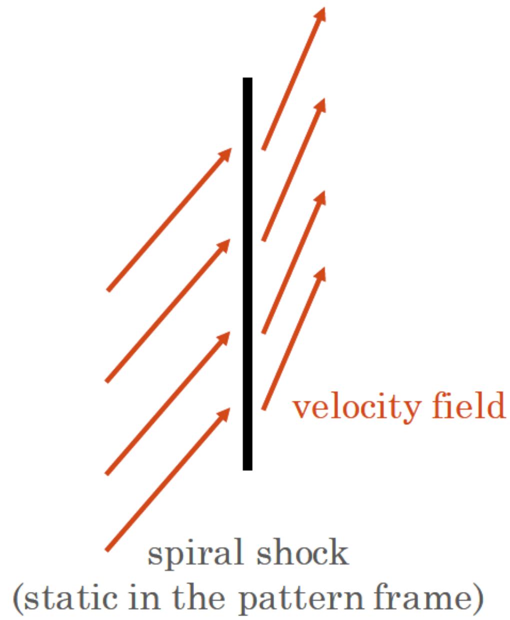

Figure 1.1: A cartoon of spiral shock: the gas flows into the spiral arm and changes its direction.

such as spurs and pearls. This thesis work is to understand the relation between the spiral arm and feathers using the theory we have developed to understand the spiral shock.

In Chapter 2, we set up a theoretical formulation to calculate analytically the gas dynamics in the interarm region. The calculation solves for five variables: gas surface density, two-dimensional gas velocity, and two-dimensional magnetic field in the two directions that are perpendicular and parallel to the spiral arm. We consider perturbations in the system such that the shock front is distorted and results in diverging and converging flows near the shock (Figure 1.2). By studying the normal mode of linearized perturbation, we find that there are unstable, growing modes that reassemble the shape of feathers in the post-shock region. This implies the existence of intrinsic instability of the spiral shock that will lead to feathers. Similar substructures were also found in the numerical magnetohydrodynamic simulations with self-gravity (e.g., Kim & Ostriker 2002, 2006) that study the gas flow passing a spiral shock under local analysis.

We show that there are at least 7 dimensionless parameters in the problem. Each of them can in principle vary independently for different galaxies, or at different loca-

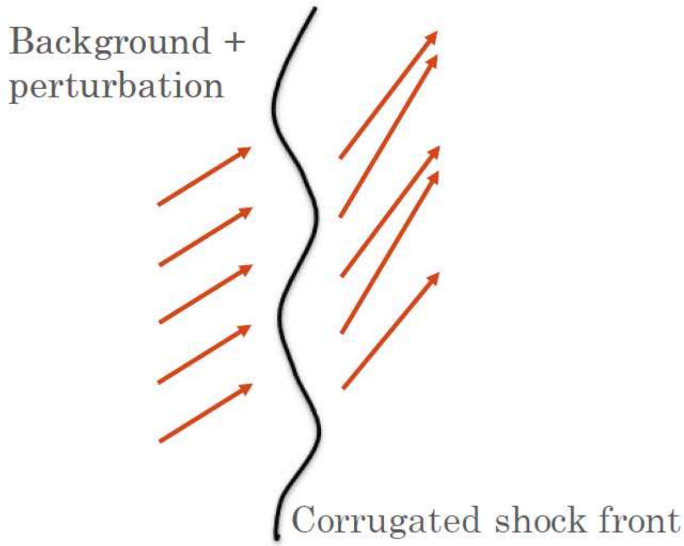

Figure 1.2: A cartoon of the feathering instability. The instability causes the corrugation on the shock front and distorts the post-shock flow.

tions in the same galaxy. Such a large parameter space not only poses a challenge for time-consuming numerical simulations, but also indicates that the physics in the problem is complex. For example, it has been shown that Jean's length, λ_J from simple gravitational collapse argument (e.g., Elmegreen 1994) cannot fully account for the length scale (e.g., spacing $\sim$ 3 to 10 λ_J) of the feathers found in observations (La Vigne et al. 2006) and numerical simulations (e.g., Kim & Ostriker 2002, 2006, etc). Therefore, the analytic calculation in this thesis is a significant step from order-of-magnitude argument to any meaningful comparisons between observations and numerical simulations.

Using the formalism developed in our first paper (Lee & Shu 2012), we investigate how the formation and dynamics of feathers depend on different physics in Chapter 3. A parameter study is very useful to find out general rules and interplay among parameters, compared to the limited number of cases in previous full-scale numerical simulations (e.g., Kim & Ostriker 2002, 2006; Chakrabarti et al. 2003; Shetty & Ostriker 2006; Dobbs & Bonnell 2006; Dobbs 2008).

The parameter study in Chapter 3 demonstrates that self-gravity is important for the feathering instability. If we decrease the strength of self-gravity, the growth rate of feathering stability decreases as well. We also identify that the most unstable mode (e.g., fastest growing mode) matches the spacing of feathers found in the inner part of M51 galaxy (La Vigne et al. 2006).

In Chapter 4, we give a summary of the findings and the future work.

Chapter 2

Formulation of the Problem

Abstract

In this paper, we study the feathering substructures along spiral arms by considering the perturbational gas response to a spiral shock. Feathers are density fluctuations that jut out from the spiral arm to the interarm region at pitch angles given by the quantum numbers of the doubly periodic structure. In a localized asymptotic approximation, related to the shearing sheet except that the inhomogeneities occur in space rather than in time, we derive the linearized perturbation equations for a razor-thin disk with turbulent interstellar gas, frozen-in magnetic field, and gaseous self-gravity. Apart from the modal quantum numbers, the individual normal modes of the system depend on seven dimensionless quantities that characterize the underlying time-independent axisymmetric state plus its steady, nonlinear, two-armed spiral-shock response to a hypothesized background density wave supported by the disk stars of the galaxy. We show that some of these normal modes have positive growth rates. Their over density contours in the post-shock region are very reminiscent of observed feathering substructures in full magnetohydrodynamic simulations. The feathering substructures are parasitic instabilities intrinsic to the system; thus, their study not only provides potential diagnostics for important parameters that characterize the interstellar medium of external galaxies, but also yields a deeper understanding of the basic mechanism that drives the formation of the giant molecular clouds and the OB stars that outline observed grand-design spirals.

2.1 Introduction

Spiral structures in nearby galaxies have fascinated astronomers since Lord Rosse's observations of M51 in 1845. The underpinning for a theoretical understanding of the phenomenon in terms of density waves has existed about 50 years (see Lin & Shu 1964 and references therein). Improved imaging technology and techniques reveal many substructures associated with the spiral arms. Here, we focus on the quasi-regularly spaced density fluctuations identified in the literature as feathers (Lynds 1970) or spurs (Elmegreen 1980). Observationally, the feathers are extinction substructure commonly found in the optical band images among spiral galaxies (e.g., La Vigne et al. 2006). For example, a Hubble Heritage image of M51 (Scoville & Rector 2001) shows many feathers (i.e., darkened dust lane in the optical image) projected into the interarm region from the primary dust lane. There are also examples showing the feathers in infrared (e.g., the 8 μm image of M81 from *Spitzer Space Telescope*) or submillimeter wavelengths, such as the detection of CO emission in M51 feathers (Corder et al. 2008). Therefore, the relationship between the feathers and the underlying interstellar medium (ISM; molecular and atomic gas, dust, magnetic field, etc.) may hold the key to an understanding of the formation of the giant molecular clouds (GMCs) and OB stars that delineate the arms of spiral galaxies.

There are two points of view regarding the background structures of spiral galaxies. The first is the hypothesis of quasi-stationary spiral structure (QSSS) that attributes the origin of spiral structure to the normal modes of the disk stars of a flattened galaxy. This point of view seems consistent with the observational finding that spiral galaxies, which look fragmentary, multi-armed, and even flocculent at optical or blue wavelengths, nevertheless have, in 2.1 μm images, the grand-design two-armed spiral structure (TASS) that underlies the QSSS hypothesis (e.g., Block & Wainscoat 1991; Block et al. 1994; Block, Elmegreen, & Wainscoat 1996). The second comes from numerical simulations that show nonlinear effects saturating the growth of unstable normal modes (e.g., Sellwood 2012) that lead to spiral patterns that are locally transient. These are dichotomies of long standing that we do not address in the present paper, which focuses on the substructures that arise from the response of the self-gravitating and magnetized ISM even to the steady forcing associated with the classic QSSS hypothesis.

Theoretical understanding of the substructures is also confused. Explanations encompass both irregular causes such as swing-amplified shearing instabilities (e.g., Goldreich & Lynden-Bell 1965), and regular causes such as gravitational instabilities (e.g., Balbus 1988; Kim & Ostriker 2002) initiated by a TASS pattern (Roberts 1969; Roberts & Yuan 1970). Another possibility is that spurs arise as response of the disk stars to over-dense regions like GMCs (e.g., Julian & Toomre 1966; D'Onghia et al. 2013). The last possibility will lead, however, to spurs with characteristic inclinations that co-rotate with the local material velocity of the GMCs, which would not have an obvious correlation with the spiral pattern of the older disk stars. Elmegreen's (1980) conclusion that spurs have characteristic inclinations that correlate with *I*-band images of the older disk stellar population suggests that feathering is best described as a long-lived phenomenon, intimately connected with the underlying spiral structure of disk galaxies. We adopt this hypothesis for the analysis of the present paper, and do not speculate on the changes necessary if spiral patterns are short-lived with spiral arms persistent only in a statistical sense.

The QSSS hypothesis implicitly underlies many numerical simulations in recent years on this subject (e.g., Kim & Ostriker 2002; Chakrabarti et al. 2003; Kim & Ostriker 2006; Shetty & Ostriker 2006; Dobbs & Bonnell 2006; Dobbs 2008). These sophisticated simulations include magnetohydrodynamics (MHD), self-gravity, ISM phases, etc. They provide a detailed time evolution of how GMCs can be formed by the fragmentation and agglomeration of interstellar gas by local Jeans instability. However, due to computational limitations, the behavior of the system is followed for only a few orbital times. Also, as we shall see, given that seven dimensionless numbers form the irreducible set that characterizes the instability of the system, a comprehensive survey of parameter space by numerical simulation is clearly out of the question for the foreseeable future. On the other hand, most theoretical linearized-stability analyses along the same line of thought include restrictive assumptions such as an arbitrary background profile, and/or a shearing-sheet approach, and/or a lack of gaseous self-gravity and/or magnetic fields (e.g., Dwarkadas & Balbus 1996). These simplifications compromise the applicability of the analysis if we wish ultimately to use the theory as a diagnostic of the physical conditions in real systems. Our aim here is to rectify these shortcomings.

In this paper, we formulate and solve the basic equations that govern the formation of feathers through the instability of a galactic spiral shock when the roles of gaseous self-gravity and magnetic field are included within the original TASS framework of Roberts (1969). We work in the frame that corotates with pattern speed $\Omega_{\rm p}$ of the spiral gravitational field of the background stellar disk, in which the TASS pattern is independent of time t and asymptotically one-dimensional (i.e., variations only in the direction perpendicular to spiral arms). By transforming the governing nonlinear equations to a spiral coordinate system (η, ξ) with η varying perpendicular to spiral arms, and ξ along them, we write down the asymptotic equations that govern nonlinear behavior in which the underlying TASS pattern varies only in η but the parasitic perturbations above the TASS pattern can vary in all three variables (η, ξ, t). The self-consistency of the asymptotic approximation then requires us to impose that single-valued perturbations are doubly periodic in (η, ξ) when we linearize in the amplitude of the perturbations relative to the TASS state. This double periodicity is characterized by two integers (quantum numbers): m, the number of stellar spiral arms in a complete circle around the galaxy with m assumed to equal to 2 in practice; and l, the number of feathers as we go along a spiral arm that would take us to the next spiral arm (half-way circumferentially around the galaxy if $m = 2$) if we were to go instead in the direction perpendicular to a spiral arm.

Our calculation on the TASS part of the problem differs from the original Roberts work in that we include frozen-in magnetic fields (as did Roberts & Yuan 1970) and gaseous self-gravity (Kim & Ostriker (2002) analysis included only the self-gravity of the feathering perturbations, and not its effect on the underlying TASS state). When we also include the effect of turbulent motions of the interstellar gas, modeled as a "logatropic" gas (pressure P proportional to the logarithm of the density ρ), there are seven dimensionless, irreducible, numbers that characterize the TASS state: (1) the ratio of the circular frequency to the epicyclic frequency Ω/κ; (2) the sine of the inclination of the stellar spiral arms, $\sin i$; (3) the dimensionless Doppler-shifted frequency at which gas rotating at its circular angular speed Ω meets m stellar spiral arms that each rotate at angular speed $\Omega_{\rm p}$, $-\nu = m(\Omega - \Omega_{\rm p})/\kappa$; (4) the amplitude of the stellar spiral gravitational field as a fraction of the axisymmetric radial gravitational field, F; (5) the dimensionless measure of the gas surface density, α; (6) the dimensionless measure of the mean gas turbulent speed, x_t; and (7) the dimensionless measure of the mean Alfvén speed of the magnetized ISM, x_A.

The paper is organized as follows. In Section 2.2, we write down the basic MHD equations in the spiral coordinates. In Section 2.3, we obtain by the shooting method the one-dimensional nonlinear TASS solution in η (across the spiral arm) modified from the Roberts-style analysis by the inclusion of magnetic fields and gaseous self-gravity. In Section 2.4, we derive the equations that govern linearized, time-dependent, two-dimensional perturbations on top of the background TASS pattern. Because the basic reference state depends only on η and not ξ nor t, the linearized perturbations can be taken to be oscillatory (with complex frequency $\omega_R + i\omega_I$) in time t and (with real dimensionless wavenumber l) in the spatial dimension ξ, but with dependences on the spatial dimension η that satisfy ordinary differential equations. Generality requires us to consider oscillatory perturbations in the position of the shock. When the appropriate jump conditions (due to the corrugation of the shock front) are imposed on top of the condition of double periodicity, we obtain the real and imaginary parts of the perturbation frequency, ω_R and ω_I, as eigenvalues of the problem when the quantum numbers m and l are specified, together with the numerical values of Ω/κ, ν, $\sin i$, F, α, x_t, and x_A. In Section 2.5, we give a sample result. In Section 2.6, we discuss the physical meaning of the result and give our conclusions.

2.2 Basic Equations and Geometry

We first write down the basic equations for the problem from the two-dimensional, time-dependent, ideal MHD equations in the rotating frame. We identify the axisymmetric, time-independent solution as the zeroth order state. We then introduce the tight-winding spiral arm approximation and obtain the first order (in term of $\sin i$) nonlinear TASS state in the sense of Roberts (1969), modified for gaseous self-gravity and the presence of frozen-in magnetic fields.

2.2.1 Basic Equations

In cylindrical polar coordinates (ϖ, φ, z), we denote Σ, u_ϖ, and u_φ as, respectively, the gas surface density, ϖ-, and φ-components of the fluid velocity in a razor-thin flat disk. The continuity and momentum equations, in a rotating frame with angular rate of the spiral pattern, $\Omega_{\rm p}$, can be written as

$$\frac{\partial \Sigma}{\partial t} + \frac{1}{\varpi}\frac{\partial}{\partial \varpi}(\varpi \Sigma u_\varpi) + \frac{1}{\varpi}\frac{\partial}{\partial \varphi}(\Sigma u_\varphi) = 0; \tag{2.1}$$

$$\frac{\partial u_\varpi}{\partial t} + u_\varpi \frac{\partial u_\varpi}{\partial \varpi} + \frac{u_\varphi}{\varpi}\frac{\partial u_\varpi}{\partial \varphi} - \frac{u_\varphi^2}{\varpi} = \mathcal{F}_\varpi - \frac{1}{\Sigma}\frac{\partial \Pi}{\partial \varpi} - \frac{\partial \mathcal{V}_{\rm eff}}{\partial \varpi} + 2\Omega_{\rm p} u_\varphi; \tag{2.2}$$

$$\frac{\partial u_\varphi}{\partial t} + u_\varpi \frac{\partial u_\varphi}{\partial \varpi} + \frac{u_\varphi}{\varpi}\frac{\partial u_\varphi}{\partial \varphi} + \frac{u_\varpi u_\varphi}{\varpi} = \mathcal{F}_\varphi - \frac{1}{\varpi \Sigma}\frac{\partial \Pi}{\partial \varphi} - \frac{1}{\varpi}\frac{\partial \mathcal{V}_{\rm eff}}{\partial \varphi} - 2\Omega_{\rm p} u_\varpi; \tag{2.3}$$

where Π is the vertically integrated gas pressure, $\mathcal{F}_\varpi$ and $\mathcal{F}_\varphi$ are the two horizontal components of the Lorentz force per unit mass. The last terms in Equations (2.2) and (2.3) are the Coriolis accelerations associated with being in a frame of reference that rotates at angular speed $\Omega_{\rm p}$. We write the effective potential as

$$\mathcal{V}_{\rm eff} \equiv \mathcal{V} - \frac{1}{2}\Omega_{\rm p}^2 \varpi^2, \tag{2.4}$$

where the second term is the centrifugal contribution and the first term is the total gravitational potential of dark matter, stars, and gas evaluated in the plane of the disk $z = 0$:

$$\mathcal{V} = \mathcal{V}_0(\varpi) + \mathcal{V}_* + (\varpi, \varphi) + \mathcal{V}_{\rm g}(\varpi, \varphi, t). \tag{2.5}$$

The axisymmetric part $\mathcal{V}_0(\varpi)$ arises from the mass distribution of all three components (dark matter, stars, and interstellar gas). It yields an angular speed $\Omega(\varpi)$ and an associated epicyclic frequency $\kappa(\varpi)$ defined by the gradient of the specific angular momentum, an expression that is also sometimes called the Rayleigh discriminant:

$$\kappa^2 \equiv \frac{1}{\varpi^3}\frac{d}{d\varpi}\left[\left(\varpi^2 \Omega\right)^2\right]. \tag{2.6}$$

The role of Ω and κ are well known in galactic dynamics, and their ratio Ω/κ is one of the fundamental dimensionless parameters in the current theory.

The quantity $\mathcal{V}_*$ is the (specified) spiral potential provided by the disk stars:

$$\mathcal{V}_* = -A(\varpi)\cos\left[m\varphi - \Phi(\varpi)\right], \tag{2.7}$$

with $A(\varpi)$ and $\Phi(\varpi)$ being the amplitude and radial phase of the spiral gravitational potential, both of which are regarded here as given functions of galactocentric radius ϖ from stellar density wave theory. In the convention of density wave theory, the radial wavenumber $k_\varpi \equiv \Phi'(\varpi)$ is negative for trailing spiral waves. The asymptotic (or WKBJ) approximation of spiral density wave theory assumes a small tilt angle i of the spiral arms, i.e., that $\tan i = m/|k_\varpi|\varpi$ is small compared to unity. To justify the use of linear theory of a sinusoidal shape factor for the stellar spiral, the radial forcing amplitude of the stellar spiral arms, $|k_\varpi|A$, should be a small fraction of the axisymmetric gravitational acceleration:

$$F \equiv \frac{|k_\varpi|A}{\varpi\Omega^2}. \tag{2.8}$$

A typical number quoted in the literature is $F = 5\%$-10%. Although infrared images may indicate stronger fractions compared to the background stellar disk, especially in the outer disk, it should be recalled that the denominator in the definition of F includes the force contribution from the dark matter halo. Shu et al. (1973, hereafter SMR) show, however, that the real measure of nonlinearity of the gaseous forcing is given by the combination,

$$f \equiv \left(\frac{\Omega}{\kappa}\right)^2 \frac{mF}{\sin i}, \tag{2.9}$$

which is not a small parameter because the large factor $m/\sin i$ compensates for the small factor F. A physical way of stating the same conclusion is that the spiral gravitational field only needs to produce radial velocities comparable to the turbulent or Alfvén speeds to have large effects (e.g., shock waves) in the ISM. The turbulent or Alfvén speeds are much smaller than the rotational velocities in giant spirals.

In this paper, we wish to study not only the effects of stellar forcing, but the enhancements produced by gaseous self-gravity. In three dimensions, the gaseous component of the gravitational potential, $\mathcal{V}_{\rm g}(\varpi, \varphi, z, t)$ is related to the gas surface density, Σ, by the Poisson equation for a razor-thin disk:

$$\frac{1}{\varpi}\frac{\partial}{\partial\varpi}\left(\varpi\frac{\partial\mathcal{V}_{\rm g}}{\partial\varpi}\right) + \frac{1}{\varpi^2}\frac{\partial^2\mathcal{V}_{\rm g}}{\partial\varphi^2} + \frac{\partial^2\mathcal{V}_{\rm g}}{\partial z^2} = 4\pi G\Sigma(\varpi, \varphi, t)\delta(z). \tag{2.10}$$

In Equations (2.2) and (2.3), the radial and tangential components of the Lorentz force per unit mass of the conducting fluid, $\mathcal{F}_\varpi$ and $\mathcal{F}_\varphi$, are given by

$$\mathcal{F}_\varpi = -\frac{z_0}{2\pi\Sigma}\frac{B_\varphi}{\varpi}\left[\frac{\partial\left(\varpi B_\varphi\right)}{\partial\varpi} - \frac{\partial B_\varpi}{\partial\varphi}\right], \tag{2.11}$$

$$\mathcal{F}_\varphi = \frac{z_0}{2\pi\Sigma}\frac{B_\varpi}{\varpi}\left[\frac{\partial\left(\varpi B_\varphi\right)}{\partial\varpi} - \frac{\partial B_\varpi}{\partial\varphi}\right], \tag{2.12}$$

where $z_0 \ll \varpi$ is the equivalent half-height of the gaseous disk over which the matter is realistically distributed. In this paper, we implicitly assume that z_0 is a constant, but Piddington (1973) pointed out that this state of affairs would lead to an enhancement of synchrotron radiation behind spiral arms that is larger than was subsequently observed (e.g., Mathewson, van der Kruit, & Brouw 1972). Mouschovias, Shu, & Woodward (1974) proposed that magnetic buckling of the field and its subsequent inflation by cosmic rays (Parker 1969) could solve this difficulty. In the current analysis, we ignore this complication as well as the role of cosmic rays, but we warn that more accurate feathering analyses will need modification when the feather spacing becomes comparable to the disk thickness.

On the large scales of interest to the problem, the interstellar magnetic field can be assumed to satisfy the condition of field freezing for a planar magnetic field:

$$\frac{\partial B_\varpi}{\partial t} + \frac{1}{\varpi}\frac{\partial}{\partial\varphi}\left(B_\varpi u_\varphi - B_\varphi u_\varpi\right) = 0; \tag{2.13}$$

$$\frac{\partial B_\varphi}{\partial t} - \frac{\partial}{\partial\varpi}\left(B_\varpi u_\varphi - B_\varphi u_\varpi\right) = 0. \tag{2.14}$$

Note that ϖ times the first equation followed by partial differentiation by ϖ added to the partial differentiation of the second equation by φ implies that the constraint of no magnetic monopoles,

$$\frac{1}{\varpi}\frac{\partial\left(\varpi B_\varpi\right)}{\partial\varpi} + \frac{1}{\varpi}\frac{\partial B_\varphi}{\partial\varphi} = 0, \tag{2.15}$$

holds for all time if it is satisfied initially.

Finally, to close our set of basic equations, we model the turbulent gas pressure with a logatropic equation of state (Lizano & Shu 1989):

$$\Pi_\mathrm{g} \equiv \Sigma_0 \mathrm{v}_{\mathrm{t}0}^2 \ln\left(\frac{\Sigma}{\Sigma_0}\right), \tag{2.16}$$

where v_{t0} is a characteristic turbulent speed. The square of the signal speed associated with this equation of state is given by

$$\mathrm{v}_\mathrm{t}^2 \equiv \frac{d\Pi_\mathrm{g}}{d\Sigma} = \mathrm{v}_{\mathrm{t}0}^2 \left(\frac{\Sigma_0}{\Sigma}\right), \tag{2.17}$$

which mimics the observed tendency for dense interstellar gas (e.g., molecular cloud complexes) to have lower turbulent speeds than rarified interstellar gas (e.g., HI clouds). The derivative of Π_g being positive and decreasing with increasing Σ are more important properties of the logarithmic law than the formal feature of having a negative turbulent pressure in the regions of low surface density, because the formal pressure can contain an arbitrary additive constant without having any physical effects on the analysis.

2.2.2 Axisymmetric State

We identify the axisymmetric quantities as the zeroth-order reference state, and denote them by the subscript “0”. With only circular velocities in the corotating frame, $u_\varphi = \varpi\left[\Omega(\varpi) - \Omega_\mathrm{p}\right]$, and toroidal magnetic fields, $B_\varphi = B_{\varphi 0}$, that depend on ϖ, the equation for radial force balance becomes

$$\varpi\Omega^2 = -\frac{d\mathcal{V}_0}{d\varpi} - \frac{1}{\Sigma_0}\frac{d\Pi_0}{d\varpi} - \frac{z_0}{2\pi\Sigma_0}\frac{B_{\varphi 0}}{\varpi}\frac{d}{d\varpi}\left(\varpi B_{\varphi 0}\right). \tag{2.18}$$

2.2.3 TASS State

In the corotating frame, the TASS state is also time-steady, so the field-freezing equation (2.13) can be satisfied, just as in the axisymmetric state, by assuming that the magnetic field is parallel to the vector velocity, which we can write in the form:

$$B_\varpi(\varpi,\varphi) = b\Sigma(\varpi,\varphi)u_\varpi(\varpi,\varphi); \tag{2.19}$$

$$B_\varphi(\varpi,\varphi) = b\Sigma(\varpi,\varphi)u_\varphi(\varpi,\varphi), \tag{2.20}$$

where the scalar factor of proportionally b is chosen to be a constant in order to satisfy the condition of zero monopoles when the equation of continuity for the gas also holds (i.e., $\mathbf{B}$ and $\Sigma\mathbf{u}$ both have zero two-dimensional divergence). Because the fluid velocity is mostly circular even in the TASS flow, the φ-component of the magnetic field is much larger than its ϖ-component, except near corotation where $\Omega(\varpi) = \Omega_\mathrm{p}$. Far from corotation, if we suppose the asymptotic approximation that the TASS flow produces radial variations that are large compared to tangential variations (or obtained by dividing perturbational quantities by ϖ), we may approximate the above expressions by

$$\mathcal{F}_\varpi \simeq -\frac{z_0}{2\pi\Sigma} B_\varphi \partial_\varpi (B_\varpi) \simeq -\mathrm{v}_{\mathrm{A0}}^2 \frac{\partial}{\partial\varpi}\left(\frac{\Sigma}{\Sigma_0}\right), \tag{2.21}$$

and,

$$\mathcal{F}_\varphi \simeq \frac{z_0}{2\pi\Sigma} B_\varpi \partial_\varpi (B_\varphi) \simeq \mathrm{v}_{\mathrm{A0}}^2 \frac{u_\varpi}{u_\varphi}\frac{\partial}{\partial\varpi}\left(\frac{\Sigma}{\Sigma_0}\right), \tag{2.22}$$

where we define the square of the unperturbed Alfv́en speed as

$$\mathrm{v}_{\mathrm{A0}}^2 \equiv \frac{B_{\varphi 0}^2}{4\pi\Sigma_0/2z_0},$$

and we have ignored the spatial variation of Σ_0 (axisymmetric part) in comparison with those of Σ.

In giant spiral galaxies, the squares of the characteristic turbulent and Alfvén speeds, $\mathrm{v}_{\mathrm{t0}}^2$ and $\mathrm{v}_{\mathrm{A0}}^2$ are small compared to the square of the flow velocity on the large scale, e.g., $\varpi^2\Omega^2$. In these circumstances, the second and third terms on the right-hand side of Equation (2.18) are small in comparison to the first, and the rotation speed $\varpi\Omega(\varpi)$ depends mostly on the gravitational potential $\mathcal{V}_0(\varpi)$ of the axisymmetric distribution of dark plus ordinary matter, which we shall henceforth assume to be fixed.

The adoption of the logarithmic equation of state allows us to write $\Sigma^{-1}\nabla\Pi_{\mathrm{g}} = \nabla\mathcal{H}_{\mathrm{g}}$, where $\mathcal{H}_{\mathrm{g}}$ is the specific enthalpy of the turbulent gas:

$$\mathcal{H}_{\mathrm{g}} = -\mathrm{v}_{\mathrm{t0}}^2 \left(\frac{\Sigma_0}{\Sigma}\right). \tag{2.23}$$

Similarly, we may identify the "specific enthalpy" associated with the dominant part of the magnetic "pressure" $\Pi_{\mathrm{m}} = (v_{A0}^2/2)\Sigma_0^{-1}\Sigma^2$:

$$\mathcal{H}_{\mathrm{m}} = \mathrm{v}_{\mathrm{A0}}^2 \left(\frac{\Sigma}{\Sigma_0}\right). \tag{2.24}$$

Nonlinear Perturbation

We now return to the rest of our equations and assume that the actual situation is a combination of an axisymmetric, time-independent state plus a nonlinear TASS response and further feathering perturbations. The subscript "1" in this section will refer to both the TASS response and the feathering instability, but in the Appendices we shall apply it only to the feathering perturbations and include the TASS response with the axisymmetric state (as unscripted variables when it will cause no confusion). In ensuing sections, we avoid confusion by attaching a ∼ when we mean the perturbations due to the feathering instability alone. Thus,

$$
\begin{aligned}
\Sigma &= \Sigma_0(\varpi) + \Sigma_1(\varpi, \varphi, t), \\
\mathcal{H} &= \mathcal{H}_0(\varpi) + \mathcal{H}_1(\varpi, \varphi, t), \\
u_\varpi &= u_{\varpi 0}(\varpi) + u_1(\varpi, \varphi, t), \\
u_\varphi &= \varpi(\Omega - \Omega_p) + \mathrm{v}_1(\varpi, \varphi, t), \\
\mathcal{F}_\varpi &= f_0(\varpi) + f_{\varpi 1}(\varpi, \varphi, t), \\
\mathcal{F}_\varphi &= f_{\varphi 1}(\varpi, \varphi, t),
\end{aligned}
\tag{2.25}
$$

where $\mathcal{H}$ is the enthalpy associated with the gas pressure and magnetic pressure. Note that only v_1 is small compared to its zeroth-order counterpart, with even the last approximation breaking down near corotation. Consistent with the approximation that the pressure gradients of the gas turbulent motions and magnetic fields contribute little to the axisymmetric force balance, we attribute their influence to the perturbations marked out by the subscript "1". Without linearization (because the TASS response is highly nonlinear), the substitution of Equations (2.25) yields the set

$$
\frac{\partial u_1}{\partial t} + u_1 \frac{\partial u_1}{\partial \varpi} + \left(\Omega - \Omega_\mathrm{p} + \frac{\mathrm{v}_1}{\varpi}\right) \frac{\partial u_1}{\partial \varphi} - \frac{\mathrm{v}_1^2}{\varpi} = 2\Omega \mathrm{v}_1 - \frac{\partial}{\partial \varpi}(\mathcal{H}_{\mathrm{g}1} + \mathcal{H}_{\mathrm{m}1} + \mathcal{U}), \tag{2.26}
$$

$$
\begin{aligned}
\frac{\partial \mathrm{v}_1}{\partial t} + u_1 \frac{\partial \mathrm{v}_1}{\partial \varpi} + \left(\Omega - \Omega_\mathrm{p} + \frac{\mathrm{v}_1}{\varpi}\right) \frac{\partial \mathrm{v}_1}{\partial \varphi} + \frac{u_1 \mathrm{v}_1}{\varpi} &= -\frac{\kappa^2}{2\Omega} u_1 - \frac{1}{\varpi}\frac{\partial}{\partial \varphi}(\mathcal{H}_{\mathrm{g}1} + \mathcal{U}) \\
&\quad + \frac{u_1}{\varpi(\Omega - \Omega_\mathrm{p}) + \mathrm{v}_1} \frac{\partial \mathcal{H}_{\mathrm{m}1}}{\partial \varpi}.
\end{aligned}
\tag{2.27}
$$

In the above, $\mathcal{U} \equiv \mathcal{V}_* + \mathcal{V}_\mathrm{g}$ is the perturbation of the gravitational potential beyond the axisymmetric state. Consistent with the approximation made above of ignoring the radius of curvature, the continuity equation becomes

$$
\frac{\partial \Sigma_1}{\partial t} + \frac{\partial}{\partial \varpi}[(\Sigma_0 + \Sigma_1) u_1] + \frac{\partial}{\partial \varphi}[\Sigma_1(\Omega - \Omega_\mathrm{p})] = 0. \tag{2.28}
$$

2.2.4 Spiral Coordinates and Asymptotic Approximation

We follow Roberts (1969) and SMR in introducing the local orthogonal coordinates (η, ξ) in the plane of the disk galaxy, where curves of ξ=constant and η=constant define, respectively, the directions perpendicular and parallel to a background stellar density waves with a locus of local gravitational potential minimum whenever the spiral phrase,

$$\eta(\varpi, \varphi) \equiv m\varphi - \Phi(\varpi) \tag{2.29}$$

that enters in Equation (2.7) equals zero or integer multiples of 2π. But the function $\eta(\varpi, \varphi)$ can increase by 2π either by φ increasing by π (for $m = 2$) with ϖ fixed (going around halfway the galaxy in a circle), or by $\Phi(\varpi)$ increasing by 2π with φ fixed (going out radially until the next spiral arm). We wish the solution to look the same in either case to lowest asymptotic order. In a local treatment, where we approximate the inclination angle i of the spiral arms with respect to the circular direction to be constant, then $\Phi(\varpi) = -(m/\tan i)\ln(\varpi/\varpi_0)$, which corresponds to the case when the stellar spiral arms are fitted by logarithmic spirals.

We now introduce the orthogonal spiral coordinates η and ξ used by SMR with $\hat{\mathbf{e}}_\eta \times \hat{\mathbf{e}}_\xi = \hat{\mathbf{e}}_z$ and

$$d\eta = -\Phi'(\varpi)d\varpi + md\varphi = m\left(\frac{1}{\tan i}\frac{d\varpi}{\varpi} + d\varphi\right), \tag{2.30}$$

$$d\xi = \frac{m}{\tan i}\left[\frac{m}{\Phi'(\varpi)}\frac{d\varpi}{\varpi^2} + d\varphi\right] = m\left(\frac{d\varpi}{\varpi} + \frac{1}{\tan i}d\varphi\right). \tag{2.31}$$

Note that if we move radially outward at fixed ϖ, ξ will increase by $2\pi \cot i$ for the same increase in ϖ that results in an increase of 2π for η. When we transform from (ϖ, φ) to (η, ξ) and draw rectangular boxes in (η, ξ), the coordinate system is similar to the one defined in Kim & Ostriker (2002), but there are two differences. (1) We do the calculations in a standard Eulerian manner, without mixing time and space coordinates as in the "shearing sheet" treatment. (2) The ratios of the axes are depicted in their correct geometric proportions, determined by the spiral pitch angle i (see Figure 2.2).

The two coordinate systems are related by the following metric:

$$ds^2 = d\varpi^2 + \varpi^2 d\varphi^2 = \frac{\varpi^2 \sin^2 i}{m^2}(d\eta^2 + d\xi^2), \tag{2.32}$$

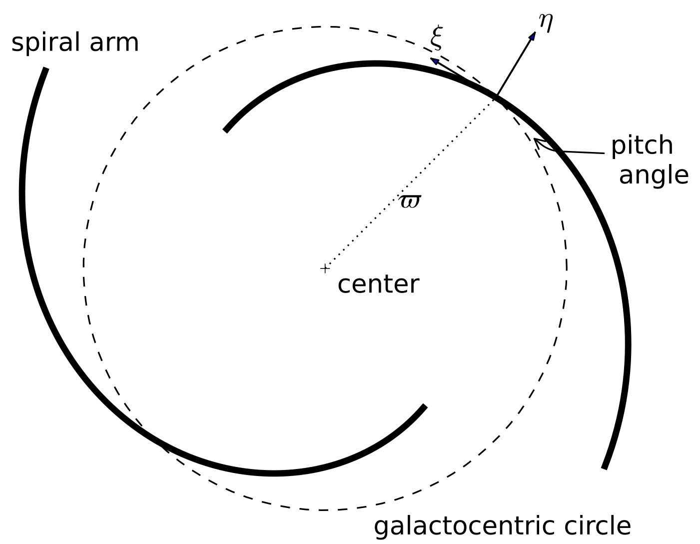

Figure 2.1: Spiral coordinates (η, ξ) are defined in the direction parallel and perpendicular to the spiral arm, locally at a galactocentric radius ϖ.

which corresponds to a local rotation through an angle i and rescaling of lengths by a common factor of $\varpi \sin i/m$.

2.2.5 Non-dimensionalization

After the transformation into the spiral coordinate (η, ξ), the equations of motion become

$$\frac{\varpi \sin i}{m}\left(\frac{\partial u_{\eta 1}}{\partial t} - 2\Omega u_{\xi 1}\right) + (u_{\eta 0} + u_{\eta 1})\frac{\partial u_{\eta 1}}{\partial \eta} + (u_{\xi 0} + u_{\xi 1})\frac{\partial u_{\eta 1}}{\partial \xi}$$
$$= -\frac{\partial}{\partial \eta}(\mathcal{H}_{\mathrm{g}1} + \mathcal{H}_{\mathrm{m}1} + \mathcal{U}), \tag{2.33}$$
$$\frac{\varpi \sin i}{m}\left(\frac{\partial u_{\xi 1}}{\partial t} + \frac{\kappa^2}{2\Omega}u_{\eta 1}\right) + (u_{\eta 0} + u_{\eta 1})\frac{\partial u_{\xi 1}}{\partial \eta} + (u_{\xi 0} + u_{\xi 1})\frac{\partial u_{\xi 1}}{\partial \xi}$$
$$= -\frac{\partial}{\partial \xi}(\mathcal{H}_{\mathrm{g}1} + \mathcal{U}) + \left(\frac{u_{\eta 0} + u_{\eta 1}}{u_{\xi 0}}\right)\frac{\partial \mathcal{H}_{\mathrm{m}1}}{\partial \eta}. \tag{2.34}$$

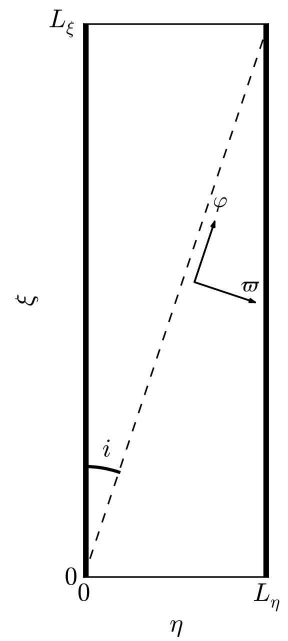

Figure 2.2: A diagram showing the local rectangular box for the spiral coordinates (η, ξ). The spiral arms are indicated by the bold vertical lines on two sides. The perpendicular distance between two arms is given by $L_{\rm arm} \equiv L_\eta = 2\pi\varpi \sin i/m$, and the dash diagonal is the line constant galactocentric radius. Since the solution is doubly-periodic in both the η and ξ directions, coordinates $(0, 0)$ and (L_η, L_ξ) represent the same location, and $\tilde{L} \equiv \cot i = L_\xi/L_\eta$.

The corresponding continuity equation reads

$$\frac{\varpi \sin i}{m}\frac{\partial \Sigma_1}{\partial t} + \frac{\partial}{\partial \eta}[(\Sigma_0 + \Sigma_1)(u_{\eta 0} + u_{\eta 1})] + \frac{\partial}{\partial \xi}[(\Sigma_0 + \Sigma_1)(u_{\xi 0} + u_{\xi 1})] = 0. \tag{2.35}$$

To write the equations in the dimensionless form, we start by picking relevant velocity scales for the problem:

$$u \equiv u_{\eta 1}/(2UV)^{1/2} \quad \text{and} \quad \text{v} \equiv u_{\xi 1}/V, \tag{2.36}$$

where we have followed SMR by defining

$$U \equiv \frac{\varpi \Omega \sin i}{m} \quad \text{and} \quad V \equiv \frac{\varpi \kappa^2 \sin i}{2\Omega m}, \tag{2.37}$$

such that the Coriolis terms become v and $-u$ for the η- and ξ-momentum equations, respectively. Similarly, we define $x_{t0}^2 \equiv \mathrm{v}_{t0}^2/2UV$ and $x_{A0}^2 \equiv \mathrm{v}_{A0}^2/2UV$ for the square of turbulent and Alfvén's speeds. For the record, we can rewrite the enthalpies into the dimensionless form:

$$h_g \equiv \mathcal{H}_{g1}/(2UV) = -x_{t0}/(1+\sigma), \tag{2.38}$$

$$h_m \equiv \mathcal{H}_{m1}/(2UV) = x_{A0}(1+\sigma), \tag{2.39}$$

where $\sigma \equiv \Sigma_1/\Sigma_0$ is the relative gas surface density between the perturbed and axisymmetric states. We also rewrite the perturbed gravitational potential $\mathcal{U} \equiv \mathcal{V}_* + \mathcal{V}_g$ as

$$\mathcal{U} = \left(\frac{\sin i}{m}\right)[-(\varpi^2\Omega^2)F\cos\eta + (2\pi\varpi G\Sigma_0)\phi], \tag{2.40}$$

where ϕ is the perturbed self-gravitational potential of the gas in units of $(\varpi \sin i/m)2\pi G\Sigma_0$. Finally, we measure time in units of inverse epicyclic frequency:

$$d\tau \equiv \kappa dt. \tag{2.41}$$

We introduce now the following additional dimensionless parameters:

$$\nu \equiv -u_{\eta 0}/(2UV)^{1/2} = m(\Omega_p - \Omega)/\kappa, \tag{2.42}$$

$$f \equiv \left(\frac{\Omega}{\kappa}\right)^2 \left(\frac{mF}{\sin i}\right), \tag{2.43}$$

$$\alpha \equiv \frac{(\varpi \sin i/m)2\pi G\Sigma_0}{2UV} = \frac{2\pi m G\Sigma_0}{\varpi\kappa^2 \sin i}, \tag{2.44}$$

where f is the afore mentioned true dimensionless measure of the nonlinearity of the stellar forcing, and α is a similar dimensionless measure of the strength of the self-gravity of the gas. Although $2\pi G\Sigma_0$ may be regarded as a small correction to the axisymmetric gravitational field of the galaxy, $\varpi\Omega^2$, nonlinear compressions behind galactic shocks make gas self-gravity a fierce contractional competitor to the vortical spin-up represented by $\varpi\kappa^2 \sin i$ when α is an order unity parameter.

The continuity and momentum equations now take the dimensionless form:

$$\frac{\partial\sigma}{\partial\tau} + \frac{\partial}{\partial\eta}[(1+\sigma)(-\nu+u)] + \frac{\partial}{\partial\xi}\left[(1+\sigma)\left(-\frac{\nu}{\tan i} + \frac{\kappa}{2\Omega}\mathrm{v}\right)\right] = 0, \tag{2.45}$$

$$\frac{\partial u}{\partial \tau} + (-\nu + u)\frac{\partial u}{\partial \eta} + \left(-\frac{\nu}{\tan i} + \frac{\kappa}{2\Omega}\mathrm{v}\right)\frac{\partial u}{\partial \xi} = \mathrm{v} - \frac{x_{\mathrm{t}0}}{(1+\sigma)^2}\frac{\partial \sigma}{\partial \eta} + f_\eta - \alpha\frac{\partial \phi}{\partial \eta} - f\sin\eta, \tag{2.46}$$

$$\frac{\partial \mathrm{v}}{\partial \tau} + (-\nu + u)\frac{\partial \mathrm{v}}{\partial \eta} + \left(-\frac{\nu}{\tan i} + \frac{\kappa}{2\Omega}\mathrm{v}\right)\frac{\partial \mathrm{v}}{\partial \xi} = -u + \frac{2\Omega}{\kappa}\left[-\frac{x_{\mathrm{t}0}}{(1+\sigma)^2}\frac{\partial \sigma}{\partial \xi} - \alpha\frac{\partial \phi}{\partial \xi}\right] + f_\xi, \tag{2.47}$$

where f_η and f_ξ are the components of the dimensionless Lorentz force per unit mass in the directions perpendicular and along the spiral arm, respectively:

$$f_\varpi = \frac{\mathcal{F}_\varpi}{(2UV)^{1/2}}, \qquad f_\varphi = \frac{\mathcal{F}_\varphi}{V}. \tag{2.48}$$

For the closure of the equations, we also need the solution of the Poisson's equation for the self-gravity of the gas and the equation of field freezing for the magnetic field.

2.3 One-dimensional Spiral Shock

In this section we revisit the steady, one-dimensional, TASS solution, adding in the consideration of the effects of magnetic field (see also Roberts & Yuan 1970) and self-gravity of the gas (see also Lubow et al. 1986). The TASS state, denoted by hats, gives the background flow of the feathering problem. All hatted quantities depend only on η, in the form $\hat{q} = \hat{q}(\eta)$.

The Lorentz force per unit mass now reads

$$\hat{f}_\eta = -x_{\mathrm{A}0}\frac{d\hat{\sigma}}{d\eta}, \tag{2.49}$$

and,

$$\hat{f}_\xi = \frac{2\Omega}{\kappa}x_{\mathrm{A}0}\left(\frac{\tan i}{1+\hat{\sigma}}\right)\frac{d\hat{\sigma}}{d\eta}. \tag{2.50}$$

Note that the Lorentz acceleration in two directions differ in scale by an extra factor of $2\Omega/\kappa$ ($= \sqrt{2UV}/V$) because of the difference in defining the dimensionless u and v. Nevertheless, f_ξ is smaller than f_η by the factor $\tan i$, and it can be dropped asymptotically in the dynamical equation for u_ξ. By also dropping the derivatives in τ and ξ, the governing equations for velocity in η- and ξ-directions now read as follows:

$$\frac{d\hat{u}}{d\eta} = (-\nu + \hat{u})\frac{\hat{\mathrm{v}} - \alpha d\hat{\phi}/d\eta - f\sin\eta}{(-\nu + \hat{u})^2 - \hat{x}}, \tag{2.51}$$

$$\frac{d\hat{\mathrm{v}}}{d\eta} = \frac{\hat{u}}{\nu - \hat{u}}, \tag{2.52}$$

where $\hat{x} \equiv x_{\mathrm{t0}}(1+\hat{\sigma})^{-1} + x_{\mathrm{A0}}(1+\hat{\sigma})$ is the square of the effective signal speed, and the parameters f and α measure the relative strength of the stellar and gaseous perturbation gravitational fields. We make use of the dimensionless mass flux as a conserved quantity along the flow by integrating the continuity equation and putting it into the form:

$$(1+\hat{\sigma})(-\nu + \hat{u}) = -\nu. \tag{2.53}$$

The self-gravity term can be obtained from a given surface density $\hat{\sigma}(\eta)$ by solving the Poisson equation under the WKBJ approximation. The derivation is standard and given in Appendix 2.A. The solution can be expressed in Fourier series form once $\hat{\sigma}(\eta)$ has been found by integrating the ODEs (Equations (2.51) and (2.52) for $\hat{u}$ and $\hat{\mathrm{v}}$, coupled with Equation (2.53) for $\hat{\sigma}$):

$$\hat{\sigma} = C_0 + \sum_{n=1}^{\infty} \left[C_n \cos(n\eta) + S_n \sin(n\eta) \right], \tag{2.54}$$

and

$$\frac{d\hat{\phi}}{d\eta} = \sum_{n=1}^{\infty} \left[-S_n \cos(n\eta) + C_n \sin(n\eta) \right], \tag{2.55}$$

where C_n and S_n are the nth Fourier components for even and odd solutions, respectively. On the other hand, the integration of Equation (2.51) requires knowledge of $\hat{\phi}$, so iteration (with a relaxation parameter) is required to find numerically a completely self-consistent solution. Apart from the added iteration and convergence steps for the self-gravity when α is nonzero, and a different expression for $\hat{x}$, Equations (2.51) and (2.52) have the same form as the set studied by SMR, and they can be solved by using the same shooting method with the matching of upstream and downstream flows satisfying the shock jump conditions discussed below.

2.3.1 Magnetosonic Point and Shock Jump Conditions

The spiral shock solution is periodic in the η-direction in the sense that when the flow passes through the shock front, it will accelerate from the submagnetosonic speed to supermagnetosonic speed, and eventually reach another shock at the next spiral arm.

Thus, the region between two consecutive shocks is transmagnetosonic and has a magnetosonic point location ($\eta = \eta_{\rm mp}$), where the speed of the flow equals the local speed of magnetosound. Solutions with multiple magnetosonic points and shocks are also possible, but their study is beyond the scope of this paper (see SMR and Chakrabarti et al. 2003 for discussions of the role of ultraharmonic resonances for producing spiral branches and their possible relationship to flocculence when overlapping resonance leads to chaotic nonlinear behavior). The magnetosonic point is located where the following condition is satisfied,

$$(-\nu + \hat{u})^2 - \hat{x} = 0, \tag{2.56}$$

which is also an apparent singular point of Equation (2.51). By substituting Equation (2.53) and the equation of state, we obtain

$$(-\nu + \hat{u})^3 + \frac{x_{\rm t0}}{\nu}(-\nu + \hat{u})^2 + x_{\rm A0}\nu = 0, \tag{2.57}$$

which is a cubic equation that gives only one positive value of $(-\nu + \hat{u}) = (-\nu + \hat{u}_{\rm mp})$ algebraically if ν is negative. A smooth solution across the magnetosonic point can be found by requiring both the numerator and denominator to be zero in Equation (2.51). Therefore, the derivatives of $\hat{u}$ and $\hat{\rm v}$ at the magnetosonic point can be evaluated as

$$\left.\frac{d\hat{u}}{d\eta}\right|_{\rm mp} = \frac{[-\hat{u}_{\rm mp}/\hat{y}_{\rm mp} - \alpha\hat{\phi}''|_{\rm mp} - f\cos\eta_{\rm mp}]^{1/2}}{\left[2 + x_{\rm t0}\nu^{-1}/\hat{y}_{\rm mp} - x_{\rm A0}\nu/\hat{y}^3_{\rm mp}\right]^{1/2}}, \tag{2.58}$$

$$\left.\frac{d\hat{\rm v}}{d\eta}\right|_{\rm mp} = \frac{\hat{u}_{\rm mp}}{\nu - \hat{u}_{\rm mp}}, \tag{2.59}$$

where $\hat{\phi}''$ is the second η-derivative of $\hat{\phi}$, and we define $\hat{y}_{\rm mp} \equiv -\nu + \hat{u}_{\rm mp}$. Note that the value of the derivatives can be evaluated by solving $\hat{u}_{\rm mp}$ in advance from Equation (2.57) with the background parameters given. In our implementation of the shooting method, we start the integration from the neighboring points of the magnetosonic transition to the shock front in both supermagnetosonic and submagnetosonic directions separately. The "initial" values of $\hat{u}$ and $\hat{\rm v}$ at these points are given by the following Taylor's series:

$$\begin{aligned} \hat{u} &= \hat{u}_{\rm mp} + \left.\frac{d\hat{u}}{d\eta}\right|_{\rm mp}(\eta - \eta_{\rm mp}) + \cdots \\ \hat{\rm v} &= \alpha\left.\frac{d\hat{\phi}}{d\eta}\right|_{\rm mp} + f\sin\eta_{\rm mp} + \left.\frac{d\hat{\rm v}}{d\eta}\right|_{\rm mp}(\eta - \eta_{\rm mp}) + \cdots . \end{aligned} \tag{2.60}$$

The derivatives of self-gravitational potential $\hat{\phi}$ are obtained from the solution of previous step. Since $d\hat{\phi}/d\eta$ is generally a smooth and continuous function, the value of $\hat{\phi}''|_{\rm mp}$ may be expressed in a finite difference form with little numerical error.

2.3.2 Matching Conditions

The physical problem is constrained by the fact that the downstream and upstream flows for a periodic solution must match the values that allow a shock jump conditions to connect the supermagnetosonic and submagnetosonic collision. These jump conditions are obtained by requiring the sum of gas (turbulent) and magnetic pressures and momentum fluxes to be continuous across the shock:

$$\left[(1+\hat{\sigma})(-\nu+\hat{u})\hat{u} + x_{\rm t0}\ln(1+\hat{\sigma}) + \frac{x_{\rm A0}}{2}(1+\hat{\sigma})^2\right]_1^2$$

and,

$$[(1+\hat{\sigma})(-\nu+\hat{u})\hat{\rm v}]_1^2$$

to vanish separately. We can identify the constant mass flux, $(1+\hat{\sigma})(-\nu+\hat{u}) = -\nu$ from the continuity equation above. Thus, we may obtain the corresponding post-shock (or pre-shock) values of $\hat{u}$ and $\hat{\rm v}$ for a given pair of values on the other side of the shock. In practice, we calculate the corresponding post-shock (submagnetosonic) values by using the pre-shock (supermagnetosonic) values, as if they were to satisfy the shock jump conditions. We postpone the discussion of the numerical results until Section 2.5.

2.4 Feathering Analysis

In the context of the feathering phenomenon, we need to consider variations in two dimensions and time. Because the reference TASS state is independent of ξ and τ, we may describe, in a linearized treatment, the additional feathering variations as oscillatory disturbances in ξ and τ. Such a treatment constitutes a standard linear-stability analysis and should be contrasted with prior treatments that supposed feathering to be a shearing, time-dependent, phenomenon that is imposed by the mathematics of a transformation that is useful only near corotation. In the current paper, we deliberately stay away from corotation. A complication that does appear is the oscillations introduced by a wiggling shock front, which leads to perturbed jump conditions that further affect the downstream flow. In any case, instead of solving a set of partial differential equations as in the numerical experiments (which do not need linearization), we obtain a set of ODEs for the feathering perturbation. Imposing double periodicity, for given m (=2 in the usual TASS picture) and l (the number of feathers strung out along the arms in the ξ-direction per spiral arm box), the (complex) oscillation frequency $\omega_R + i\omega_I$ in time becomes an eigenvalue of the overall problem.

2.4.1 Perturbational Equations

As the feathering perturbations are time dependent and vary along both η- and ξ-directions spatially, we define the variables as follows:

$$\begin{aligned} u &= \hat{u}(\eta) + \tilde{u}(\eta, \xi, t), \\ \mathrm{v} &= \hat{\mathrm{v}}(\eta) + \tilde{\mathrm{v}}(\eta, \xi, t), \\ \sigma &= \hat{\sigma}(\eta) + \tilde{\sigma}(\eta, \xi, t), \\ \phi &= \hat{\phi}(\eta) + \tilde{\phi}(\eta, \xi, t), \end{aligned} \tag{2.61}$$

where the hat states are the background TASS flow, and the tilde states are perturbations assumed to be small compared to the background. The perturbational magnetic field is time dependent, and we no longer assume its direction is parallel to the flow as was assumed for the TASS background. We will derive the perturbation induction equation in Appendix 2.B), where we show it corresponds simply to the conservation relation for the magnetic flux function A (the z-component of the vector potential for the magnetic field). For here, we simply record the resulting linearized perturbation fluid equations for the tilde quantities:

$$\frac{\partial \tilde{\sigma}}{\partial \tau} + (-\nu + \hat{u})\frac{\partial \tilde{\sigma}}{\partial \eta} + \tilde{u}\frac{d\hat{\sigma}}{d\eta} + \hat{\mathrm{v}}_{\mathrm{T}}\frac{\partial \tilde{\sigma}}{\partial \xi} = -(1+\hat{\sigma})\frac{\partial \tilde{u}}{\partial \eta} - \frac{d\hat{u}}{d\eta}\tilde{\sigma} - (1+\hat{\sigma})\frac{\kappa}{2\Omega}\frac{\partial \tilde{\mathrm{v}}}{\partial \xi}, \tag{2.62}$$

$$\begin{aligned} \frac{\partial \tilde{u}}{\partial \tau} + (-\nu + \hat{u})\frac{\partial \tilde{u}}{\partial \eta} + \tilde{u}\frac{d\hat{u}}{d\eta} + \hat{\mathrm{v}}_{\mathrm{T}}\frac{\partial \tilde{u}}{\partial \xi} =& \tilde{\mathrm{v}} - \left[\frac{x_{\mathrm{t0}}}{(1+\hat{\sigma})^2}\right]\frac{\partial \tilde{\sigma}}{\partial \eta} + \frac{d\hat{\sigma}}{d\eta}\frac{2x_{\mathrm{t0}}}{(1+\hat{\sigma})^3}\tilde{\sigma} \\ & - \alpha\frac{\partial \tilde{\phi}}{\partial \eta} + \tilde{f}_\eta, \end{aligned} \tag{2.63}$$

$$\frac{\partial \tilde{\mathrm{v}}}{\partial \tau} + (-\nu + \hat{u})\frac{\partial \tilde{\mathrm{v}}}{\partial \eta} + \tilde{u}\frac{d\hat{\mathrm{v}}}{d\eta} + \hat{\mathrm{v}}_{\mathrm{T}}\frac{\partial \tilde{\mathrm{v}}}{\partial \xi} = -\tilde{u} - \frac{2\Omega}{\kappa}\left[\frac{x_{\mathrm{t0}}}{(1+\hat{\sigma})^2}\frac{\partial \tilde{\sigma}}{\partial \xi} + \alpha\frac{\partial \tilde{\phi}}{\partial \xi}\right] + \tilde{f}_\xi, \tag{2.64}$$

where $\hat{\mathrm{v}}_{\mathrm{T}}$ is the total ξ-component of the background fluid velocity (i.e., axisymmetric plus TASS) in the frame that corotates with the stellar spiral. The perturbed Lorentz acceleration, $\tilde{f}_\eta$, and $\tilde{f}_\xi$ are given by

$$\tilde{f}_\eta = x_{\mathrm{A0}}\left(\frac{\partial^2}{\partial\eta^2} + \frac{\partial^2}{\partial\xi^2}\right)\tilde{A}_1 + x_{\mathrm{A0}}\frac{\hat{\sigma}'}{1+\hat{\sigma}}\frac{\partial\tilde{A}_1}{\partial\eta}, \tag{2.65}$$

and

$$\tilde{f}_\xi = -\frac{2\Omega}{\kappa}x_{\mathrm{A0}}\left(\frac{\tan i}{1+\hat{\sigma}}\right)\left(\frac{\partial^2}{\partial\eta^2} + \frac{\partial^2}{\partial\xi^2}\right)\tilde{A}_1 + \frac{2\Omega}{\kappa}x_{\mathrm{A0}}\frac{\hat{\sigma}'}{1+\hat{\sigma}}\frac{\partial\tilde{A}_1}{\partial\xi}, \tag{2.66}$$

respectively. In the above, $\tilde{A}_1$ is the dimensionless z-component of the perturbational magnetic potential. The perturbational evolutionary equation for it reads (see Appendix 2.B)

$$\frac{\partial\tilde{A}_1}{\partial\tau} + (-\nu+\hat{u})\frac{\partial\tilde{A}_1}{\partial\eta} + \hat{\mathrm{v}}_{\mathrm{T}}\frac{\partial\tilde{A}_1}{\partial\xi} = (1+\hat{\sigma})\tilde{u} - \left(\frac{\kappa}{2\Omega}\tan i\right)\tilde{\mathrm{v}}. \tag{2.67}$$

2.4.2 Perturbed Shock Jump Conditions

The perturbed shock jump conditions can be obtained by linearizing the jump conditions in the frame of perturbed shock front. The shock front is displaced and no longer parallel to the spiral arm. In Figure 2.3, we show the configuration of the perturbation. Inside corotation radius, the flow is entering the shock from the left in the frame of the shock. Hence, we must obtain the normal direction of the shock and the shock velocity in the current frame. The position of the perturbed shock is now given by

$$\eta = \eta_{\mathrm{sh}} + \epsilon(\xi, t), \tag{2.68}$$

where η_{sh} is the unperturbed position and ϵ is a small number. We define

$$s = \eta - \eta_{\mathrm{sh}} - \epsilon(\xi, t), \tag{2.69}$$

to be the displacement from the moving shock front. Thus, the locus of the shock front is $s = 0$ and the unit normal $\hat{\mathbf{n}}$ is given by

$$\begin{aligned}\hat{\mathbf{n}} &= \frac{1}{|\nabla s|}\left[\left(\frac{\partial s}{\partial\eta}\right)\hat{\mathbf{e}}_\eta + \left(\frac{\partial s}{\partial\xi}\right)\hat{\mathbf{e}}_\xi\right]\\ &= \frac{1}{|\nabla s|}\left[\hat{\mathbf{e}}_\eta - \left(\frac{\partial\epsilon}{\partial\xi}\right)\hat{\mathbf{e}}_\xi\right],\end{aligned} \tag{2.70}$$

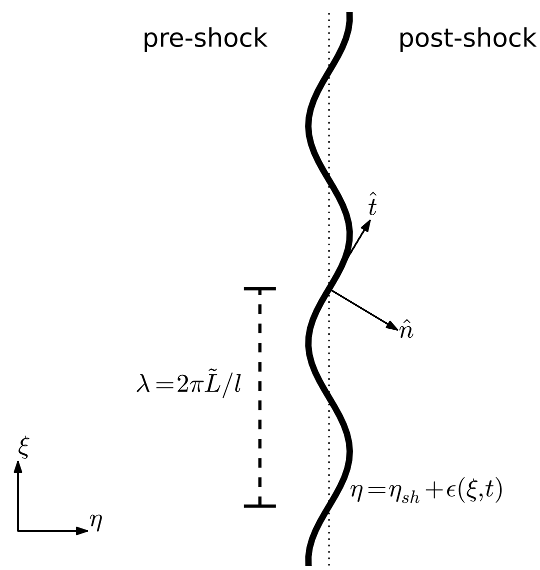

Figure 2.3: Corrugation of the shock front. The perturbation, ϵ, along the shock front is characterized by the wavelength $\lambda = 2\pi\tilde{L}/l$ and is assumed to have small amplitude. The vertical dotted line is equilibrium shock front at $\eta = \eta_{\mathrm{sh}}$. The unit normal and unit tangent are denoted by $\hat{n}$ and $\hat{t}$, respectively.

where $|\nabla s| = [1 + (\partial\epsilon/\partial\xi)^2]^{1/2} \simeq 1 + O(\epsilon^2)$ is the magnitude of the gradient normal. The velocity of the shock, $\mathbf{D}$, which is normal to the shock front, can be found by considering a normal displacement Δr of the locus at time Δt, i.e., $|\nabla s|\Delta r + \Delta t(\partial s/\partial t) = 0$, and thus, $\mathbf{D} = \hat{\mathbf{n}}\Delta r/\Delta t = (\partial\epsilon/\partial t)\hat{\mathbf{n}}$ in the first order of ϵ.

There are five shock jump conditions in the problem (see, Shu 1992, Equations 25.16-18,20,21). The linearized perturbation in the moving shock frame reads

$$[\rho\delta u_\perp + u_\perp\delta\rho]_1^2 = 0, \tag{2.71}$$

$$\left[u_\perp^2\delta\rho + 2\rho u_\perp\delta u_\perp + \left(\frac{\partial P}{\partial\rho}\right)\delta\rho + \frac{B_\parallel}{4\pi}\delta B_\parallel\right]_1^2 = 0, \tag{2.72}$$

$$\left[u_\perp u_\parallel\delta\rho + \rho u_\perp\delta u_\parallel + \rho u_\parallel\delta u_\perp - \frac{B_\perp}{4\pi}\delta B_\parallel - \frac{B_\parallel}{4\pi}\delta B_\perp\right]_1^2 = 0, \tag{2.73}$$

$$[\delta B_\perp]_1^2 = 0, \tag{2.74}$$

$$[B_\perp\delta u_\parallel - B_\parallel\delta u_\perp + u_\parallel\delta B_\perp - u_\perp\delta B_\parallel]_1^2 = 0, \tag{2.75}$$

where the variables with and without δ are in first and zeroth order of ϵ, respectively. The jump conditions are given in terms of variables parallel and perpendicular to the shock front locus, $s = 0$. Since the perturbation on the shock front is in first order of ϵ, the non-δ variables are simply their background counterpart. For the variables that are first order in ϵ, we include both Taylor's expansion at the perturbed shock front and the geometrical projection (i.e., in Lagrangian sense). Thus, by making use of the unit normal in Equation (2.70), and the corresponding unit tangent, we express the dimensional gas surface density, flow velocities, and magnetic fields into the following:

$$\rho \simeq \hat{\rho} + \tilde{\rho} + \epsilon d\hat{\rho}/d\eta, \tag{2.76}$$

$$u_\perp \simeq \hat{u}_\eta + \tilde{u}_\eta + \epsilon d\hat{u}_\eta/d\eta - D_\eta - \hat{u}_\xi\partial_\xi\epsilon, \tag{2.77}$$

$$u_\parallel \simeq \hat{u}_\xi + \tilde{u}_\xi + \epsilon d\hat{u}_\xi/d\eta + \hat{u}_\eta\partial_\xi\epsilon, \tag{2.78}$$

$$B_\perp \simeq \hat{B}_\eta + \tilde{B}_\eta + \epsilon d\hat{B}_\eta/d\eta - \hat{B}_\xi\partial_\xi\epsilon, \tag{2.79}$$

$$B_\parallel \simeq \hat{B}_\xi + \tilde{B}_\xi + \epsilon d\hat{B}_\xi/d\eta + \hat{B}_\eta\partial_\xi\epsilon, \tag{2.80}$$

where we evaluate the variables at $\eta = \eta_{\rm sh}$, and we define D_η and D_ξ as the η- and ξ-components of the shock velocity, respectively. Note that $D_\eta = (\partial\epsilon/\partial t)/|\nabla s|^2 \simeq (\partial\epsilon/\partial t)$, and we exclude $D_\xi = O(\epsilon^2)$. To make the equations dimensionless, we measure the surface density, velocities and magnetic fields in term of Σ_0, $\sqrt{2UV}$, and $B_{\xi 0}$, respectively. We now write the boundary conditions (2.71)-(2.75) a more compact form

$$\mathbf{Q}(1)\mathbf{V}(1) = \mathbf{Q}(2)\mathbf{V}(2), \tag{2.81}$$

where $\mathbf{Q} = \mathbf{Q}(\eta)$ is a 5×5 matrix is given by the coefficients in Equations (2.76)-(2.80) in terms of the background variables and $\mathbf{V} = [\delta\sigma, \delta u, (\kappa/2\Omega)\delta \mathrm{v}, \delta B_\perp/B_{\xi 0}, \delta B_\parallel/B_{\xi 0}]^T$ is a column vector of the δ variables.

2.4.3 Stability Analysis

As the governing equations for the perturbed variables do not have explicit dependence in τ and ξ, we can simplify the equations by assuming that the tilde variables have $e^{i\omega\tau - il\xi/\tilde{L}}$ dependences. The perturbed shock front must have the same sinusoidal dependence in time and space (see Figure 2.3). The instability condition follows when $\mathrm{Im}(\omega) = \omega_\mathrm{I} < 0$. To treat the perturbational self-gravity, we use a simplified solution to the Poisson equation obtained in Appendix 2.A:

$$\tilde{\phi}_{\omega,l}(\eta) = -\frac{\tilde{L}}{|l|}\tilde{\sigma}_{\omega,l}(\eta), \tag{2.82}$$

appropriate to the assumption (motivated by the observations) that the important feathering corresponds to large l (many individual feathers in the ξ-direction for the equivalent spiral box where we only have one TASS arm becoming another in the η direction).

After rearranging the terms, we obtain

$$(-\nu + \hat{u})\frac{d\tilde{\sigma}_{\omega,l}}{d\eta} + (1+\hat{\sigma})\frac{d\tilde{u}_{\omega,l}}{d\eta} = (-\hat{u}' - i\omega_\mathrm{T})\tilde{\sigma}_{\omega,l} - \hat{\sigma}'\tilde{u}_{\omega,l} + \frac{il}{\tilde{L}}\frac{\kappa}{2\Omega}(1+\hat{\sigma})\tilde{\mathrm{v}}_{\omega,l}, \tag{2.83}$$

$$\begin{aligned}
&\left[\frac{x_{\mathrm{t}0}}{(1+\hat{\sigma})^2} - \alpha\frac{\tilde{L}}{|l|}\right]\frac{d\tilde{\sigma}_{\omega,l}}{d\eta} + (-\nu + \hat{u})\frac{d\tilde{u}_{\omega,l}}{d\eta} - \frac{x_{\mathrm{A}0}\hat{\sigma}'}{1+\hat{\sigma}}\frac{d\tilde{A}_{1\omega,l}}{d\eta} - x_{\mathrm{A}0}\frac{d\tilde{A}'_{1\omega,l}}{d\eta} \\
=&\frac{2x_{\mathrm{t}0}\hat{\sigma}'}{(1+\hat{\sigma})^3}\tilde{\sigma}_{\omega,l} + (-\hat{u}' - i\omega_\mathrm{T})\tilde{u}_{\omega,l} + \tilde{\mathrm{v}}_{\omega,l} - x_{\mathrm{A}0}\left(\frac{l}{\tilde{L}}\right)^2\tilde{A}_{1\omega,l},
\end{aligned} \tag{2.84}$$

$$\begin{aligned}
&(-\nu + \hat{u})\frac{d\tilde{\mathrm{v}}_{\omega,l}}{d\eta} + \frac{2\Omega}{\kappa}x_{\mathrm{A}0}\left(\frac{\tan i}{1+\hat{\sigma}}\right)\frac{d\tilde{A}'_{1\omega,l}}{d\eta} \\
=& -\left(-\frac{il}{\tilde{L}}\right)\left(\frac{2\Omega}{\kappa}\right)\left[\frac{x_{\mathrm{t}0}}{(1+\hat{\sigma})^2} - \alpha\frac{\tilde{L}}{|l|}\right]\tilde{\sigma}_{\omega,l} - (1+\hat{\sigma})\tilde{u}_{\omega,l} - i\omega_\mathrm{T}\tilde{\mathrm{v}}_{\omega,l} \\
&+ \frac{2\Omega}{\kappa}x_{\mathrm{A}0}\left[\frac{\tan i}{1+\hat{\sigma}}\left(\frac{l}{\tilde{L}}\right)^2 - \frac{\hat{\sigma}'}{1+\hat{\sigma}}\left(\frac{il}{\tilde{L}}\right)\right]\tilde{A}_{1\omega,l},
\end{aligned} \tag{2.85}$$

where we define $\omega_{\rm T} \equiv \omega - (l/\tilde{L})\hat{\rm v}_{\rm T}$ to be the dimensionless Doppler-shifted frequency in the moving frame of the background flow along the spiral arm. The transformed induction equation reads,

$$(-\nu + \hat{u})\tilde{A}'_{1\omega,l} = -i\omega_{\rm T}\tilde{A}_{1\omega,l} + (1+\hat{\sigma})\tilde{u}_{\omega,l} - \left(\frac{\kappa}{2\Omega}\tan i\right)\tilde{\rm v}_{\omega,l}. \tag{2.86}$$

Similarly, by taking the Fourier transform and matching the first order terms in the perturbational jump conditions (2.76)-(2.80), we can express the δ terms in the in terms of the tilde (Eulerian) variables:

$$\begin{aligned}
\delta\sigma &= \tilde{\sigma} + \epsilon d\hat{\sigma}/d\eta, \\
\delta u &= \tilde{u} + \epsilon d\hat{u}/d\eta - i\omega_{\rm T}\epsilon, \\
\delta v &= \tilde{\rm v} + \epsilon d\hat{\rm v}/d\eta - \frac{2\Omega}{\kappa}\frac{il}{\tilde{L}}\hat{u}\epsilon, \\
\delta B_\perp/B_{\xi 0} &= -\frac{il}{\tilde{L}}\tilde{A}_1 + \frac{il}{\tilde{L}}(1+\hat{\sigma})\epsilon, \\
\delta B_\parallel/B_{\xi 0} &= -\tilde{A}'_1 + \epsilon d\hat{\sigma}/d\eta,
\end{aligned} \tag{2.87}$$

where we drop the subscripts (ω, l) for clarity, and we have used $d\hat{B}_\eta/d\eta \propto d(\Sigma u_\eta)/d\eta = 0$,

$$\frac{\epsilon}{B_{\xi 0}}\frac{d\hat{B}_\xi}{d\eta} = \frac{\epsilon}{\Sigma_0}\frac{d\Sigma}{d\eta} \simeq \epsilon\frac{d\hat{\sigma}}{d\eta},$$

$$\frac{B_\parallel^{(0)}}{B_{\xi 0}} \simeq \frac{\hat{B}_\xi}{B_{\xi 0}} = (1+\hat{\sigma}) \quad \text{and} \quad \frac{B_\perp^{(0)}}{B_{\xi 0}} \simeq \frac{\hat{B}_\eta}{B_{\xi 0}} = \tan i,$$

and we neglect the term with $\partial_\xi \epsilon(\hat{B}_\eta/B_{\xi 0}) = O(\epsilon \tan i)$.

2.4.4 Method of Solution

We try to solve the *four* perturbed equations (2.83)-(2.86) as a set of ODEs. Since the Lorentz force contains a second derivative of the scalar magnetic potential, it might seem that we require one more differential equation for its derivative, $d\tilde{A}_1/d\eta = \tilde{A}'_1$. However, the induction equation (2.86) is in fact an algebraic equation for $\tilde{u}$, $\tilde{\rm v}$, $\tilde{A}_1$, and $\tilde{A}'_1$, and does not involve $d\tilde{A}'_1/d\eta$. The physical reason is that field freezing implies that the tilde magnetic potential must yield a magnetic field structure that corresponds to the TASS magnetic field stretched in time by the motion of the electrically conducting matter in the feathering instability (see Appendix B). In other words, the field freezing equation (2.86) must hold in space simultaneously with the other differential equations, and so, the system is a set of differential algebraic equations, where $d\tilde{A}_1'/d\eta$ is obtained by *differentiation* after we make the set self-consistent by treating ω not as an arbitrary constant, but as a (complex) eigenvalue of the time-dependent transformation of the TASS state to one that contains (exponentially growing) feathering perturbations. Fortunately, the problem so posed can be solved by following the procedure discussed below.

First, we should reduce the order of the perturbed equations such that it solves for the tilde variables $(\tilde{\sigma}, \tilde{u}, \tilde{\mathrm{v}}, \tilde{A}_1)$ (and their first derivatives on the right-hand side) only. The solution of $\tilde{A}_1'$ can be obtained algebraically from the induction equation once we have solved for other variables. The elimination of $\tilde{A}_1''$ may then be done by numerically differentiation of the induction equation, i.e.,

$$\begin{aligned} &-(1+\hat{\sigma})\frac{d\tilde{u}_{\omega,l}}{d\eta} + \frac{\kappa}{2\Omega}\tan i\frac{d\tilde{\mathrm{v}}_{\omega,l}}{d\eta} + (-\nu+\hat{u})\frac{d\tilde{A}_{1\omega,l}'}{d\eta} \\ =&\hat{\sigma}'\tilde{u}_{\omega,l} + \left(\frac{il}{\tilde{\bar{L}}}\right)\left(\frac{\kappa}{2\Omega}\right)(1+\hat{\sigma})\tilde{A}_{1\omega,l} - (\hat{u}'+i\omega_{\mathrm{T}})\tilde{A}_{1\omega,l}'. \end{aligned} \tag{2.88}$$

Second, we should reduce the number of perturbational jump conditions to *four*, as we have *four* differential equations after the reduction above. In fact, the fifth jump condition, Equation (2.75), is satisfied automatically by the "algebraic" induction equation. In other words, if the complex frequency ω has the correct eigenvalue, we can impose both double periodicity and match all the requisite jump conditions, with Equation (2.75) being consistent with the induction equation with which we use to calculate $\tilde{A}_1'$. We can eliminate $\tilde{A}_1'$ in the connection conditions by using Equation (2.86), which is valid for both sides of the shock separately. Therefore, the dimension of the coefficient matrix $\mathbf{Q}$ in Equation (2.81) is reduced to 4×4.

After we "separate" the induction equation from the differential equations in the above manner, we may solve the system as a *two-point boundary value problem with eigenvalues*. Standard methods of attack exist in the literatures (e.g., Ascher et al. 1995). One difficulty of using the publicly available numerical packages is that they do not treat the embedded jump conditions present in our system. To solve this problem, we can artificially modify our jump conditions in the following form:

$$\mathbf{Q(1)V(1)} = \mathbf{C}_1 \quad \text{and} \quad \mathbf{Q(2)V(2)} = \mathbf{C}_2, \tag{2.89}$$

where the two vectors $\mathbf{C}_1$ and $\mathbf{C}_2$ are varied until they are equal to each other. The procedure leads to the ability to use standard packages at the numerical expense of solving four more equations. There are also standard methods to solve a system with complex variables as in our problem, and we do not discuss the numerical issues further here.

2.5 Numerical Results

In this section, we present results of the calculation with input parameters based on the Sofue et al. (1999) rotation curve of the M81 Galaxy. Table 2.1 lists the relevant numerical values used for the feathering calculation, and Table 2.2 gives the seven dimensionless parameters needed for solving the governing equations in that calculation. The listed mean gas surface density Σ_0, gas turbulent velocity v_{t0}, and interstellar magnetic field are all too high for an Sb spiral galaxy of luminosity class II like M81, but we adopt these extreme values to illustrate a point that will become apparent in our closing discussion.

In any case, the mean plasma β is $\beta_0 \equiv x_{t0}/x_{A0} = 1$ for the choice $x_{t0} = x_{A0}$, and implies that turbulent stresses $\propto x_{t0}/(1+\hat{\sigma})$ dominate in the interarm region where $\hat{\sigma} < 0$) while magnetic stresses $\propto x_{A0}(1+\hat{\sigma})$ dominate in the arm region where $\hat{\sigma} > 0$. We define a mean Toomre's Q parameter for the gas accounting for mean turbulent motions and magnetic field (with mean effective sound speed, $a_0 \propto \sqrt{x_0}$) as

$$Q \equiv \frac{\kappa a_0}{\pi G \Sigma_0} = \frac{2}{\alpha}(x_{t0} + x_{A0})^{1/2}. \tag{2.90}$$

With $x_{t0} = x_{A0} = 0.1$ and $\alpha = 0.35$, we have $Q = 2.55$, so the gas is stable on average to all axisymmetric self-gravitational perturbations.

2.5.1 TASS Profiles with Self-gravity and Magnetic Field

The dimensionless parameter α characterizes the gaseous self-gravity. In general, it is an order unity quantity for spiral galaxies of not too early a Hubble type. Figure

Table 2.1: Typical Galactic Parameters for the Feathering Example of This Paper

Rotation curve	Sofue et al. (1999)
Galactocentric radius [a]	5.0 kpc
L_{arm}	3.8 kpc
Turbulent speed	13.4 km s^{-1}
Alfvén's speed	13.4 km s^{-1}
Magnetic field [b,c]	14.8 μG
Mean gas surface density [c]	38.6 $M_{\odot}$ pc^{-2}
Inclination of stellar spiral arm [d]	14°
Pattern speed [e]	23.4 km s^{-1} kpc^{-1}

[a] The distance from the modeling region to the galactic center

[b] Value of $B_{\varphi 0}$ for scale height $z_0 = 200$ pc

[c] For $\alpha = 0.35$

[d] Adopted from Kendall et al. (2008)

[e] Adopted from Westpfahl (1998)

Table 2.2: Typical Set of Local Parameters (ϖ = 5.0kpc) for the Feathering Example of This Paper.

Ω/κ	0.666
$\tan i$	0.249
F	11.5%
α	0.35
ν	-0.666
x_{A0}	0.1
x_{t0}	0.1

2.4 shows the surface density in the perpendicular direction to the arm. The plot is similar to the Roberts (1969) calculation, except the surface density is no longer arbitrarily scalable when we include self-gravity. The shock strength increases with increasing α (with all other parameters held fixed as in Table 2) because the gaseous self-gravity deepens the minimum of the spiral gravitational potential. More of the support for the total spiral gravitational potential coming from the gas also pulls the shock front downstream closer to the potential minimum. Increases in α also rounds out the density peak. These effects were also seen in the one-dimensional numerical simulations of Kim & Ostriker (2002).

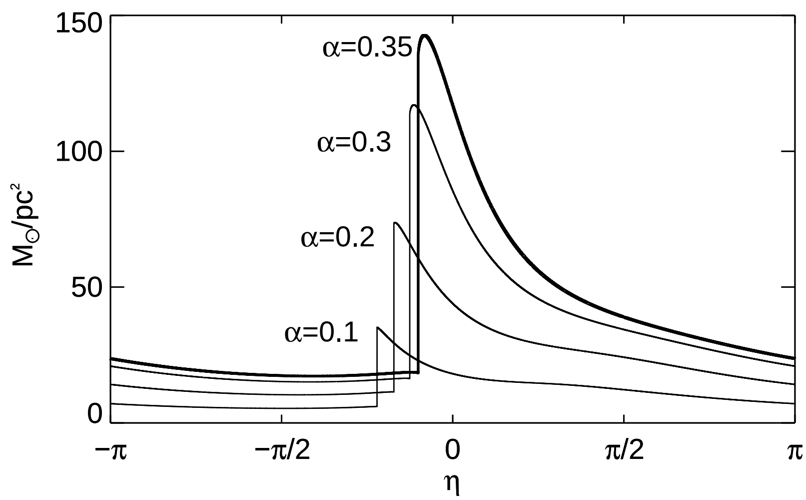

Figure 2.4: Surface density of the gas for α from 0.1 to 0.35 (corresponding to 11 to 39 $\mathrm{M}_{\odot}\,\mathrm{pc}^{-2}$ for the mean surface density) and $F = 11.5\%$. The minimum stellar gravitational potential is located at $\eta = 0$. The thick line ($\alpha = 0.35$) is the background density profile used for the feathering perturbation example.

On the other hand, the full width at half maximum (FWHM) of the density profile is approximately constant. If the FWHM is taken as a representative value, the width of the arm with spiral galactic shocks is about 12% of the distance between two arms, or about 480 pc in the current model.

Magnetic Field

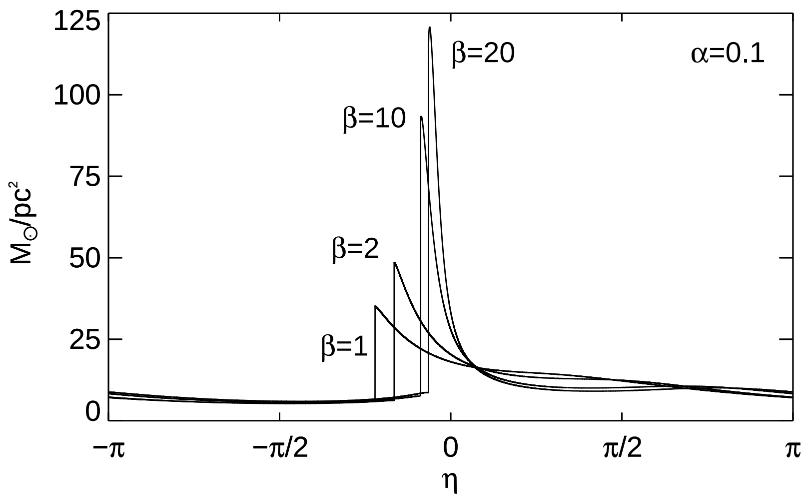

Figure 2.5: Surface density of the gas for plasma β, $\beta_0 = 1.0, 2.0, 10$ and 20 (corresponding to $B_{\varphi 0} = 7.9, 5.6, 2.5$ and 1.8 μG, respectively). The mean surface gas density is set to 11 $M_\odot/pc^2$ ($\alpha = 0.1$).

Contrary to previous assertions (cf. Dobbs & Bonnell 2006), the magnetic field plays an important role in spiral galactic shocks and the resultant feathering instabilities (see, e.g., Kim & Ostriker 2002). Figure 2.5 shows some different choices for the magnetization parameter $x_{A0} = x_{t0}/\beta_0$, when the turbulent and self-gravity parameters are kept fixed at $x_{t0} = 0.1$ and $\alpha = 0.1$ with all other dimensionless parameters held at the values given in Table 2. In general, the increase in x_{A0} (or decrease in β_0) suppresses the compression of gas in the post-shock region and lowers the shock strength. Conversely, the peak surface density rises very rapidly with increasing β_0 (i.e., decreasing magnetic field strength), and there is no steady solution possible for β_0 much larger than 20, i.e., the spiral arms would go into continued gravitational collapse with $\alpha = 0.1$ if the magnetic field is too weak. The magnetic field cannot be ignored either for the structure of the TASS density pattern or for the development of the feathering instability when self-gravity is important. The dependences of the background profile and the feathering perturbation on the dimensionless parameters of the problem will be investigated in

Paper II.

2.5.2 Feathering Perturbation

Taking the TASS one-dimensional solution as the background for the feathering phenomenon, we solve the perturbed equations for each l-mode and obtain the two-dimensional solution using inverse Fourier transforms. A larger survey of parameter space is undertaken in Paper II. Here, we just show a typical result for the total surface density and magnetic field lines in Figures 2.6. To obtain sufficient contrast, we have arbitrarily scaled the linear perturbations so that they are no longer small compared to the background. Figure 2.6 compares the flow solutions with and without the feathering perturbation for $l = 8$. For better viewing of the post-shock region, the horizontal axis is not really η, but $\eta - \eta_{\mathrm{sh}}$. For the background flow on the left, the magnetic field reaches peak compression behind the shock but becomes weaker for increasing η as the expansional flow out of the spiral arm pulls apart the frozen-in field lines. With the development of the feathering perturbation with $l = 8$ on the right (i.e., eight feathers in a distance, L_ξ), over dense regions jut out from the spiral arm toward the interarm region downstream. In this particular case, the Doppler-shifted frequency is $\omega_{\mathrm{T}} = -0.113 - 0.174i$ in unit of κ. The non-zero real part of ω_{T} implies that the pattern of feathers moves along the *outward* ξ-direction with the passage of time, a result also seen in the numerical calculations of the Ostriker group. The negative value of the imaginary part of ω_{T} implies that this mode is unstable and can be expected indeed to grow to nonlinear amplitudes with the passage of time. With $\kappa = 70.2$ km s^{-1} kpc^{-1}, the e-folding growth time scale t_g is

$$t_g = -\frac{1}{\kappa \, \mathrm{Im}\, \omega_T} = \frac{1}{0.174\kappa} \simeq 80 \times 10^6 \mathrm{yr}. \tag{2.91}$$

In Figure 2.7, we show the velocity field (arrows) superimposed on the surface density profile (colored contours) of the feathering perturbation at a single instant of time. The perturbed flow follows closely to the background spiral shock profile because the background circular motion is dominant over all other motions. Nevertheless, significant convergence toward density peaks and divergences from density troughs can still be found *along* the spiral arm, especially toward the beginning of the feathers. The behavior can be profitably compared to the zoom-in plot of Shetty & Ostriker (2006). It is tempting to speculate whether the velocity fluctuations in the nonlinear development of the instability can be mistaken for turbulent velocities in insufficiently angularly resolved images of spiral galaxies.

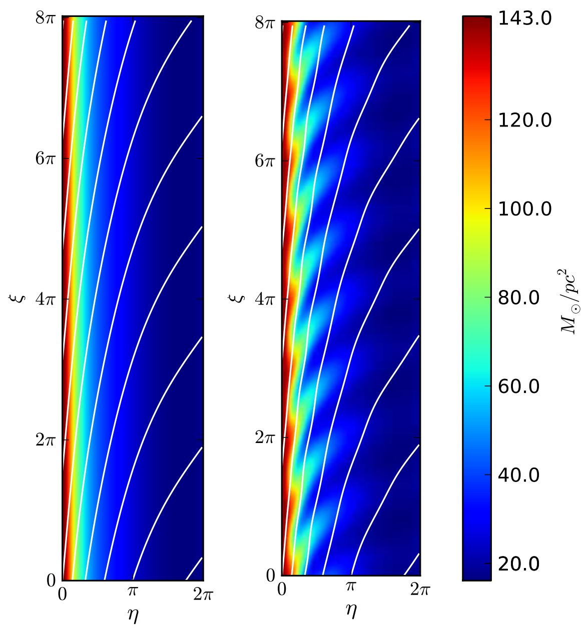

Figure 2.6: Comparison between the background flow with $\alpha = 0.35$ (*left*) and the flow with feathering perturbation of the $l = 8$ mode (*right*). The color shows the surface density of the gas in linear scale, and the white lines are the magnetic field lines. Since $\tilde{L} = \cot i \simeq 4$ in the model, the periodicity of ξ is approximately 8π.

2.6 Discussions and Conclusion

It is illuminating to compare the numerical result (Equation (2.91)) with a simple model of one-dimensional Jeans instability. The Jeans instability cannot occur in one-dimensional equilibrium states if the compression occurs isothermally because the increase in pressure forces keeps pace with the increase in self-gravitation (cf. Spitzer 1968), but if the (turbulent) equation of state is softer than isothermal, as it is for the

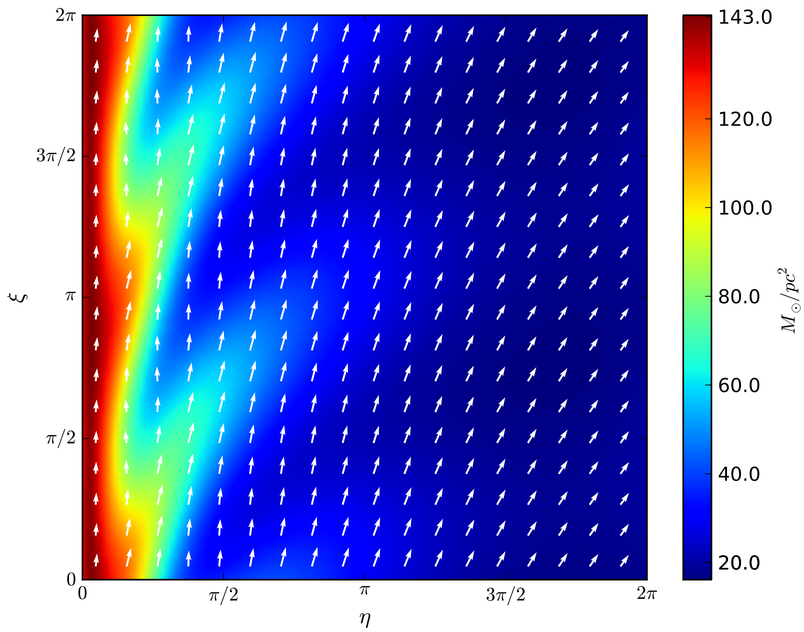

Figure 2.7: Velocity field of the feathering perturbation ($l = 8$) with the background spiral shock. Without feathering perturbation, the velocity is expected to have no variation along ξ.

adopted logatropic law of the current paper, then it is possible for the self-gravity of condensations parallel to the galactic shock to overwhelm the declining resistance of the turbulent motions. According to the estimate by Shu et al. (2007), the feathering instability is then basically the self-gravitational contraction of over dense gas along post-shock magnetic field lines, which is almost aligned along the density ridge of the TASS pattern. A rough estimate of the contraction time is then

$$t_c \simeq \frac{\pi}{4}\left(\frac{G\Sigma_g W}{L^2}\right)^{-1/2}, \tag{2.92}$$

where W is the half-width of the TASS spiral arm, which we shall take to equal the 0.48 kpc mentioned previously, and $L = L_{\text{arm}}(\tilde{L}/l)/4$ is the quarter-wavelength of the feathering instability (the center to edge distance of over dense regions) and also equals, by coincidence, 0.48 kpc. If we replace Σ_g with the mean surface density *in the spiral arm*, which is a few times denser than the average including the interarm region, for

$l = 8$ and $\alpha = 0.35$, we have

$$\begin{aligned} t_c &= \frac{\pi}{4}\left[\frac{(4.302\times10^{-6})(71\times10^{6})(0.48)}{(0.48)^2}\right]^{-1/2} \\ &= 0.031(\mathrm{km\,s^{-1}\,kpc^{-1}})^{-1} \\ &= 31\times10^{6}\mathrm{yr}, \end{aligned} \tag{2.93}$$

where we have chosen Σ_g to have its half-peak value, 71 $M_\odot$ pc^{-2}, in the feather.

The rough estimate (2.93) underestimates the accurate computation of Equation (2.91) by a factor of 2.6, suggesting that differential expansion and magnetic stresses in the post-shock region play stabilizing influences in the actual feathering phenomenon. Nevertheless, although the correct mathematical calculation of the feathering instability is complex, the basic mechanism behind its operation is roughly quasi-one-dimensional contraction along magnetic field lines roughly parallel to the spiral arm while the background flow is swept downstream roughly perpendicular to the spiral arm. Numerical simulation then demonstrates that the full nonlinear development of the instability results, not in permanent collapse for most of the gas in the over dense regions, but to a redispersal in between the spiral arms as the expanding set of background magnetic fields helps to tear apart the dense condensations that might in a nonmagnetic context have experienced overall continued gravitational collapse. Shu et al. (2007) suggest that this is the reason why OB star formation, as prominently as they seem to delineate spiral structure and substructure, is actually quite inefficient in its operation in the present, relatively strongly magnetized, universe of ISMs. This mental construct, coupled with the visual display of Figure 2.7, suggests that GMC associations are, not permanent material entities, but a manifestation of the parasitic formation and dissolution of the feathers at the crests of the nonlinear density waves that we call gaseous spiral arms. With this point of view (which we recognize will not be universally accepted), the pattern is long-lived; the individual condensations are not.

Acknowledgments

This research is part of the PhD Thesis Dissertation of W.K.L. in the Physics Department of UCSD. The authors also acknowledge the support of the National Science Council (NSC) of Taiwan for its support of the Theoretical Institute for Advanced Research in Astrophysics (TIARA) based in Academia Sinica's Institute of Astronomy and Astrophysics (ASIAA).

Chapter 2, in full, is a reprint of the material as it appears in Astrophysical Journal, 2012, 756, 45. Lee, Wing-Kit; Shu, Frank. The dissertation author was the primary investigator and author of this paper.

Appendix

2.A WKBJ Approximation of Self-gravity

The self-gravity of the gas is governed by the Poisson equation in the thin-disk geometry,

$$\nabla^2 \mathcal{V}_{\rm g} = 4\pi G \Sigma \delta(z), \tag{2.A.1}$$

where $\mathcal{V}_{\rm g}$ and Σ are the gravitational potential and surface density of the gas, respectively. We use the above equation for both quasi-one-dimensional spiral shock and the two-dimensional feathering perturbation. In the asymptotic approximation (quasi-rectangular) of the spiral coordinates introduced in this paper, we can write the Laplacian in the following form:

$$\nabla^2 = \left(\frac{\varpi \sin i}{m}\right)^{-2} \left(\frac{\partial^2}{\partial \eta^2} + \frac{\partial^2}{\partial \xi^2} + \frac{\partial^2}{\partial \zeta^2}\right), \tag{2.A.2}$$

where $\zeta \equiv z/(\varpi \sin i/m)$ and z is the physical coordinate perpendicular to the plane of the razor-thin disk. Consistent with Equation (2.40), we define

$$\mathcal{V}_{\rm g} \equiv 2\pi G \Sigma_0 (\varpi \sin i/m) \phi,$$

so that ϕ is the dimensionless gaseous self-gravitational potential. The dimensionless Poisson equation now reads

$$\left(\frac{\partial^2}{\partial \eta^2} + \frac{\partial^2}{\partial \xi^2} + \frac{\partial^2}{\partial \zeta^2}\right)\phi = 2\sigma\delta(\zeta), \tag{2.A.3}$$

and is subject to the following boundary conditions: $\partial_\zeta \phi|_{-\epsilon}^{+\epsilon} = 2\sigma$ as the integrability condition across the midplane $\zeta = 0$; $\phi \to 0$ when $\zeta \to \pm\infty$; periodic boundary conditions for η-and ξ-directions. Note that both ϕ and $\partial_\eta \phi$ are continuous across the spiral shock, but the term $\partial_\eta^2\phi$ requires special treatment because of the delta function on the right-hand side. If we Fourier transform in η and ξ, we have $[-n^2-(l/\tilde{L})^2+\partial_\zeta^2]\tilde{\phi}_{n,l} = 2\tilde{\sigma}_{n,l}\delta(\zeta)$, where n and $l/\tilde{L}$ are the corresponding wavenumbers for these directions. By integrating the last expression across $\zeta = 0$ and requiring exponentially decaying solutions in the ζ-direction for both positive and negative values of ζ, we get the familiar WKBJ result:

$$\tilde{\phi}_{n,l} = -\frac{\tilde{\sigma}_{n,l}}{\sqrt{n^2 + (l/\tilde{L})^2}}. \tag{2.A.4}$$

For a one-dimensional TASS density profile, we take $l = 0$ and get $\tilde{\phi}_{n,0} = -2\tilde{\sigma}_{n,0}/|n|$. Then, it is straight forward to obtain Equations (2.54) and (2.55) by considering the real and imaginary parts of $\tilde{\sigma}_n$.

For the two-dimensional feathering perturbation, we adopt a simplification of the complete treatment. For feathering perturbations reminiscent of the substructures observed in real spiral galaxies, $l/\tilde{L}$ is appreciably larger than the n values needed to reconstruct a reasonable accurate surface density profile of the TASS background state. To be sure, a formally infinite number of n's are required if we wish to recover the sharp jump of the background shock front, but this is a feature of the background state and not of the smoother perturbations that we are ascribing to the feathering instability. Correcting for the finite thickness of the disk would also lead to smoother relations between the perturbed self-gravitational potential and the perturbational surface density. With the assumption that $l/\tilde{L}$ is much larger than the n in any of the important Fourier coefficients $\tilde{\phi}_{n,l}$ and $\tilde{\sigma}_{n,l}$, we adopt the following approximation:

$$\tilde{\phi}_l(\eta) = -\frac{1}{|l/\tilde{L}|}\tilde{\sigma}_l(\eta) \quad \text{and} \quad \tilde{\phi}'_l(\eta) = -\frac{1}{|l/\tilde{L}|}\tilde{\sigma}'_l(\eta). \tag{2.A.5}$$

In the actual example shown in Figure 2.7, the validity of the approximation is questionable, as it amounts to the assumption that $(l/\tilde{L})^2 = 2^2$ is a large number. But the feathering displayed in that figure also has too large a spacing between condensations; better examples will be given in Paper II where the approximation used in Equation (2.A.5) has more justification.

2.B Perturbation on the Lorentz Force and Induction Equation

Because the interstellar magnetic field is free of monopoles, it is derivable as the curl of a vector potential $\mathbf{A}$. For a field that lies entirely in a plane, the vector potential can have a single component, $\mathbf{A} = A(\varpi, \varphi, t)\hat{\mathbf{e}}_z$. Under these circumstances,

$$\mathbf{B} = \nabla \times (A\hat{\mathbf{e}}_z) = -\hat{\mathbf{e}}_z \times \nabla A. \tag{2.B.1}$$

The equation for field freezing can now be written as

$$\nabla \times \left[\frac{\partial A}{\partial t}\hat{\mathbf{e}}_z - (\hat{\mathbf{e}}_z \times \nabla A) \times \mathbf{u}\right] = 0. \tag{2.B.2}$$

With a proper choice of gauge (namely an initial time-independent state in which $\mathbf{B}$ is parallel to $\mathbf{u}$, or ∇A is perpendicular to $\mathbf{u}$), we can "uncurl" the above equation, expand the triple vector product, and derive an evolutionary equation for A:

$$\frac{\partial A}{\partial t} + \mathbf{u} \cdot \nabla A = 0. \tag{2.B.3}$$

In other words, field freezing in this context is simply the statement of the conservation of A as we follow the motion of fluid elements.

If we write $A = A_0 + A_{\text{TASS}} + A_1$, and $\mathbf{u} = \mathbf{u}_0 + \mathbf{u}_{\text{TASS}} + \mathbf{u}_1$, the satisfaction of the condition of field freezing by the zeroth order axisymmetric and TASS states implies to linear order that

$$\frac{\partial A_1}{\partial t} + (\mathbf{u}_0 + \mathbf{u}_{\text{TASS}}) \cdot \nabla A_1 = -\left[\nabla (A_0 + A_{\text{TASS}})\right] \cdot \mathbf{u}_1. \tag{2.B.4}$$

The elimination of one spatial derivative in the evolutionary equation for A_1 (or $\tilde{A}_1$) explains why there is no equation for $d\tilde{A}_1'/d\eta$ in Section 2.4.4.

If we use tilde to denote dimensionless perturbational variables,

$$\tilde{A}_1 \equiv \frac{m}{\varpi \sin i}\frac{A_1}{B_{\xi 0}}, \tag{2.B.5}$$

we then obtain from equation (2.B.4)

$$\frac{\varpi \sin i}{m}\frac{\partial \tilde{A}_1}{\partial t} + u_\eta \frac{\partial \tilde{A}_1}{\partial \eta} + u_\xi \frac{\partial \tilde{A}_1}{\partial \xi} = \frac{\varpi \sin i}{m}\left(B_\xi u_{\eta 1} - B_\eta u_{\xi 1}\right). \tag{2.B.6}$$

Again, we have used unscripted variables to denote the axisymmetric state (denoted with a zero) plus the TASS value (denoted with a hat), and a subscript "1" to denote the dimensioned quantity associated with the feathering perturbations (when non-dimensionalized, these are given a tilde). Using the definition of $\tilde{A}_1$ in Equation (2.B.5) and dividing Equation (2.B.6) by $\sqrt{2UV}$, we obtain the dimensionless induction equation:

$$\frac{1}{\kappa}\frac{\partial \tilde{A}_1}{\partial t} + (-\nu + \hat{u})\frac{\partial \tilde{A}_1}{\partial \eta} + \left(\frac{-\nu}{\tan i} + \frac{\kappa}{2\Omega}\hat{\mathrm{v}}\right)\frac{\partial \tilde{A}_1}{\partial \xi} = (1+\hat{\sigma})\tilde{u} - \left(\frac{\kappa}{2\Omega}\tan i\right)\tilde{\mathrm{v}}, \tag{2.B.7}$$

where we have used $\tilde{u} \equiv u_{\eta 1}/\sqrt{2UV}$, $\tilde{\mathrm{v}} \equiv u_{\xi 1}/V$, $\hat{B}_\xi/B_{\xi 0} = (1+\hat{\sigma})$ and $\hat{B}_\eta/B_{\xi 0} = \tan i$. In practice, we also need the governing equation of $\tilde{A}_1' \equiv \partial \tilde{A}_1/\partial\eta$, which can be obtained by taking the η-derivative of Equation (2.67):

$$\begin{aligned}&\frac{1}{\kappa}\frac{\partial \tilde{A}_1'}{\partial t} + (-\nu + \hat{u})\frac{\partial \tilde{A}_1'}{\partial \eta} + \frac{d\hat{u}}{d\eta}\tilde{A}_1' + \frac{-\nu}{\tan i}\frac{\partial \tilde{A}_1'}{\partial \xi} + \frac{\kappa}{2\Omega}\frac{d\hat{\mathrm{v}}}{d\eta}\frac{\partial \tilde{A}_1'}{\partial \xi}\\ =&(1+\hat{\sigma})\frac{\partial \tilde{u}}{\partial \eta} + \frac{d\hat{\sigma}}{d\eta}\tilde{u} - \left(\frac{\kappa}{2\Omega}\tan i\right)\frac{\partial \tilde{\mathrm{v}}}{\partial \eta}.\end{aligned} \tag{2.B.8}$$

To compute the linearized Lorentz force, we use the expression

$$\mathbf{f} = -\frac{2z_0}{4\pi\Sigma}\left[\left(\nabla^2 A\right)\nabla A_1 + \left(\nabla^2 A_1\right)\nabla A\right]. \tag{2.B.9}$$

Again, we have used A as a short hand for $A_0 + A_{\mathrm{TASS}}$. We also ignore the linearized contribution that comes from expanding $\Sigma = \Sigma_0 + \Sigma_{\mathrm{TASS}} + \Sigma_1$ in the denominator because we are interested the feathering effect in the post-shock region, where the perturbation surface density Σ_1 is very small relative to the axisymmetric and TASS contributions. More explicitly, then, we have to lowest asymptotic order for small $\sin i$:

$$\nabla\left(A_0 + A_{\mathrm{TASS}}\right) \simeq \frac{m}{\varpi \sin i}\left(\frac{\partial A}{\partial \eta}\hat{\mathbf{e}}_\eta + \frac{\partial A}{\partial \xi}\hat{\mathbf{e}}_\xi\right) = -B_\xi \hat{\mathbf{e}}_\eta + B_\eta \hat{\mathbf{e}}_\xi,$$

and,

$$\nabla^2\left(A_0 + A_{\mathrm{TASS}}\right) \simeq \frac{m}{\varpi \sin i}\left(-\frac{\partial B_\xi}{\partial \eta} + \frac{\partial B_\eta}{\partial \xi}\right) = -\frac{m}{\varpi \sin i}\frac{d\hat{B}_\xi}{d\eta},$$

where on the right-hand sides we have used $A = A_0 + A_{\mathrm{TASS}}$ as a shorthand. Therefore, the perturbed Lorentz force per unit mass can be written as

$$\mathbf{f} = -\frac{2z_0}{4\pi\Sigma}\left(\nabla^2 A_1\right)\nabla A - \frac{2z_0}{4\pi\Sigma}\left(\nabla^2 A\right)\nabla A_1, \tag{2.B.10}$$

where we define the perturbed magnetic field, $\mathbf{B}_1 = -\hat{\mathbf{e}}_z \times \nabla A_1$. For notational convenience, we write the perturbation Lorentz acceleration as coming from two parts: $\mathbf{f}_1 = \mathbf{f}^{(1)} + \mathbf{f}^{(2)}$, where

$$\begin{aligned}\mathbf{f}^{(1)} &= \frac{2z_0}{4\pi\Sigma}\left(\nabla^2 A_1\right)\left(\hat{B}_\xi \hat{\mathbf{e}}_\eta - \hat{B}_\eta \hat{\mathbf{e}}_\xi\right) \\ &\simeq \frac{m}{\varpi \sin i} \mathrm{v}_{\mathrm{A}0}^2 \left(\frac{\partial^2 \tilde{A}_1}{\partial \eta^2} + \frac{\partial^2 \tilde{A}_1}{\partial \xi^2}\right)\left(\hat{\mathbf{e}}_\eta - \frac{\hat{u}_\eta}{\hat{u}_\xi}\hat{\mathbf{e}}_\xi\right),\end{aligned} \tag{2.B.11}$$

and

$$\begin{aligned}\mathbf{f}^{(2)} &\simeq \frac{2z_0}{4\pi\Sigma}\left(\frac{m}{\varpi \sin i}\right)^2 \frac{d\hat{B}_\xi}{d\eta}\left(\frac{\partial A_1}{\partial \eta}\hat{\mathbf{e}}_\eta + \frac{\partial A_1}{\partial \xi}\hat{\mathbf{e}}_\xi\right) \\ &\simeq \frac{m}{\varpi \sin i}\frac{v_{\mathrm{A}0}^2}{1+\hat{\sigma}}\frac{d\hat{\sigma}}{d\eta}\left(\frac{\partial \tilde{A}_1}{\partial \eta}\hat{\mathbf{e}}_\eta + \frac{\partial \tilde{A}_1}{\partial \xi}\hat{\mathbf{e}}_\xi\right).\end{aligned} \tag{2.B.12}$$

In the above, we have approximated $\cos^2 i \simeq 1$ for small $\sin i$. The dimensionless components of the Lorentz force (f_η, f_ξ) can be found by rearranging the terms:

$$\begin{aligned}f_\eta =& \left(\frac{\varpi \sin i/m}{2UV}\right)\mathrm{f}_{1\eta} \\ =& x_{\mathrm{A}0}\left(\frac{\partial^2}{\partial \eta^2} + \frac{\partial^2}{\partial \xi^2}\right)\tilde{A}_1 + x_{\mathrm{A}0}\frac{\hat{\sigma}'}{1+\hat{\sigma}}\frac{\partial \tilde{A}_1}{\partial \eta}\end{aligned}$$

and,

$$\begin{aligned}f_\xi =& \left(\frac{\varpi \sin i/m}{V\sqrt{2UV}}\right)\mathrm{f}_{1\xi} \\ =& -\frac{2\Omega}{\kappa}x_{\mathrm{A}0}\left(\frac{\tan i}{1+\hat{\sigma}}\right)\left(\frac{\partial^2}{\partial \eta^2} + \frac{\partial^2}{\partial \xi^2}\right)\tilde{A}_1 + \frac{2\Omega}{\kappa}x_{\mathrm{A}0}\frac{\hat{\sigma}'}{1+\hat{\sigma}}\frac{\partial \tilde{A}_1}{\partial \xi},\end{aligned}$$

where the factor $(\varpi \sin i/m)$ is included for consistency with the convention in our dimensionless variables (which will be eventually canceled).

2.C Matrices

Here we list out the coefficient matrices for the ODEs (see, Equations (2.83)-(2.86)) involved in the calculation (in the form of $\mathbf{A}(\eta)\mathbf{V}'(\eta) = \mathbf{B}(\eta)\mathbf{V}(\eta)$) before the reduction procedure in the Section 2.4.4. The *four* ODEs and the *five* tilde variables correspond to the columns and rows, respectively. We obtain the square matrices by eliminating the fifth column with the use of induction equation (see the text). Basically the matrices are collections of the background terms in the equations and boundary conditions. For the purpose of clarity, we define the following: $u_{\rm T} \equiv -\nu + \hat{u}$, $\sigma_{\rm T} \equiv 1 + \hat{\sigma}$, and $\omega_{\rm T} \equiv \omega - (l/\tilde{L})\hat{\rm v}_{\rm T}$. The "mass matrix", $\hat{\mathbf{A}}_{\omega,l}$:

$$\begin{pmatrix} u_{\rm T} & \sigma_{\rm T} & 0 & 0 & 0 \\ \hat{b} & u_{\rm T} & 0 & -x_{\rm A0}\hat{\sigma}'/\sigma_{\rm T} & -x_{\rm A0} \\ 0 & 0 & u_{\rm T} & 0 & \hat{h}x_{\rm A0} \\ 0 & 0 & 0 & u_{\rm T} & 0 \end{pmatrix}, \tag{2.C.1}$$

where

$$\hat{b} \equiv \frac{x_{\rm t0}}{(1+\hat{\sigma})^2} - \alpha\frac{\tilde{L}}{|l|} \quad \text{and} \quad \hat{h} \equiv \frac{2\Omega}{\kappa}\left(\frac{-\nu+\hat{u}}{-\nu/\tan i}\right) = \frac{2\Omega}{\kappa}\frac{\tan i}{1+\hat{\sigma}}. \tag{2.C.2}$$

The matrix $\hat{\mathbf{B}}_{\omega,l}$ is given by

$$\begin{pmatrix} -\hat{u}' - i\omega_{\rm T} & -\hat{\sigma}' & i(l/\tilde{L})(\kappa/2\Omega)\sigma_{\rm T} & 0 & 0 \\ 2x_{\rm T0}\hat{\sigma}'/\sigma_{\rm T}^3 & -\hat{u}' - i\omega_{\rm T} & 1 & -x_{\rm A0}(l/\tilde{L})^2 & 0 \\ (2\Omega/\kappa)(il/\tilde{L})\hat{b} & -(1+\hat{\rm v}') & -i\omega_{\rm T} & (2\Omega/\kappa)x_{\rm A0}/\sigma_{\rm T}\left[\tan i(l/\tilde{L})^2 - \hat{\sigma}'(il/\tilde{L})\right] & 0 \\ 0 & \sigma_{\rm T} & -(\kappa/2\Omega)\tan i & -i\omega_{\rm T} & 0 \end{pmatrix}. \tag{2.C.3}$$

Chapter 3

Parameter Study

3.1 Introduction

We previously formulated the problem of galactic feather formation by solving the instabilities in the spiral arms (Lee & Shu 2012, presented in Chapter 2) and presented a solution with typical galactic parameters based on the M81 galaxy. We showed that the feathers can be formed through the feathering instability of the spiral arm. In this chapter, we perform a parameter study of the feathering instability by examining the dependence of the two-dimensional gas response on the relevant free dimensionless parameters of the problem.

The feathering instability of the galactic spiral shock depends on 7 dimensionless parameters in the local analysis, namely: the background gas velocity perpendicular to the arm, ν; the strength of stellar spiral potential, f; the strength of self-gravity of the gas, α; the square of turbulent speed of the gas, x_{t0}; the square of Alfvén's speed, x_{A0}; the ratio of the rotational and epicyclic frequency, Ω/κ; and the tangent of pitch angle of the spiral arm, $\tan i$.

We investigate how different parameters affect the spiral shock and the corresponding feathering perturbations. The parameters are separated into 3 groups according to their roles: Group I is the set of dimensionless parameters that sets the problem of the spiral shock profile; Group II is the set of dimensionless parameters that sets the problem of the feathering perturbation, given a set of Group I parameters; Group III is the set of dimensional scales that sets the physical scales and units. The meanings of parameter groups I, II and III are presented in the Table 3.1. These groups of parameters are defined in a way that 1) the first two groups characterize the flow; and 2) the third group gives the physical scale so that the dimensionless calculations can be scaled to match different physical conditions. We adopt the same notation of variables as Chapter 2.

3.2 Basic Equations

The basic equations in the parameter study are the same as presented in Chapter 2. We study the magnetohydrodynamic (MHD) response of a self-gravitating razor-thin gas disk under the influence of a static two-arm spiral pattern of stars. We work in the pattern frame of the spiral structure and assume that the spiral arms are tight-winding. In short, there are two parts of the calculation. First, we obtain the basic state by solving the quasi-one-dimensional spiral shock problem (Roberts 1969; Roberts & Yuan 1970; Shu et al. 1973; Lubow et al. 1986). Second, we perform the stability analysis by considering the two-dimensional perturbations with corrugated shock front.

We study the stability problem by transforming the system into a local rectangular box that is tilted along the spiral arm. The axes are defined by the local spiral coordinates (η, ξ) used by Shu et al. (1973). The η-coordinate goes from 0 to 2π, which corresponds to the perpendicular displacement from one spiral arm to the next. The ξ-coordinate has the same scale as η but runs in the parallel direction to the spiral arm. Since the arm-to-arm distance is $L_{\rm arm} = 2\pi\varpi \sin i/m$, where m is the number of spiral arms, the physical length scale of η- and ξ-coordinates is

$$L_0 = \varpi \sin i/m. \tag{3.1}$$

We express the MHD equations in a rotating pattern frame with frequency, $\Omega_{\rm p}$ in terms of a velocity perturbation due to the spiral shock in the directions perpendicular and parallel to the stationary stellar spiral arm. Following the formulation in Shu et al. (1973), we introduce two velocity scales U and V for normalization. We define

$$U \equiv \frac{\varpi\Omega \sin i}{m} \quad \text{and} \quad V \equiv \frac{\varpi\kappa^2 \sin i}{2\Omega m}, \tag{3.2}$$

where Ω is the rotational frequency and κ is the epicyclic frequency. Thus, the normalization factors for velocity in η- and ξ-directions are given by

$$\sqrt{2UV} = \kappa L_0 \quad \text{and} \quad V = \frac{\kappa^2}{2\Omega} L_0. \tag{3.3}$$

We transform the η- and ξ-momentum equations into dimensionless variables by dividing $2UVL_0$ and $\sqrt{2UV}VL_0$, respectively. Consistent with the above normalization, the dimensionless time variable is defined by $\tau = \kappa t$.

Since the background circular velocity in η-direction is $u_{\eta 0} = \varpi(\Omega - \Omega_{\rm p}) \sin i$, its dimensionless counterpart is $-\nu \equiv u_{\eta 0}/\sqrt{2UV} = m(\Omega - \Omega_{\rm p})/\kappa$, which is the ratio of the frequency of Doppler-shifted circular flow and that of the radial oscillations. This parameter together with a pressure term determines the ultra-harmonic resonance locations which was studied in Shu et al. (1973). In this paper, we concern the region inside the corotation radius, where $\Omega > \Omega_{\rm p}$ and $\nu < 0$.

In addition to the MHD equations, we also solve for the self-gravity of the gas. The Poisson equation of a razor-thin gas disk in the dimensionless form is

$$\nabla^2 \phi = 2(1 + \sigma)\delta(\zeta), \tag{3.4}$$

where ϕ is the dimensionless gravitational potential; $1 + \sigma \equiv \Sigma/\Sigma_0$ and $\zeta \equiv z/L_0$ are the dimensionless surface density and z-coordinate, respectively. The dimensional unit of ϕ is $2\pi G \Sigma_0 L_0$. Here we assume the gas does not affect the spiral structure of stars and only concern the gas response due to the stellar spiral structure.

3.3 Physical Scales

In this section, we provide the conversion formulas for some physical variables from parameters in Group I, II and III. In particular, we use the perpendicular distance between spiral arms, $L_{\rm arm}$ and the pattern speed, $\Omega_{\rm p}$ to obtain the physical scale for length and time, respectively. Except for the background magnetic field, $B_{\varphi 0}$ (which also depends on the half-height of gas disk, z_0), most of the variables can be scaled with a physical unit accordingly using $L_{\rm arm}$ and $\Omega_{\rm p}$.

Table 3.1: Description of Parameters

Group I	
ν	background gas velocity perp. to the arm
f	spiral shock strength
α	strength of self-gravity of the gas
x_{t0}	square of turbulent speed of the gas
x_{A0}	square of Alfvén's speed

Group II	
Ω/κ	ratio of rotational and epicyclic freq.
$\tan i$	tangent of pitch angle of the spiral arm

Group III	
$L_{\rm arm}$	perpendicular separation of spiral arms
z_0	half-height of the gas disk
$\Omega_{\rm p}$	pattern speed

Group I The dimensionless parameters in Group I define the problem of spiral shock which is the basic state of the feathering perturbation. They are defined by the following:

$$\nu \equiv m(\Omega_{\rm p} - \Omega)/\kappa, \tag{3.5}$$

$$f \equiv \left(\frac{\Omega}{\kappa}\right)^2 \left(\frac{mF}{\sin i}\right), \tag{3.6}$$

$$\alpha \equiv \frac{2\pi m G \Sigma_0}{\varpi \kappa^2 \sin i}, \tag{3.7}$$

$$x_{t0} \equiv \frac{{\rm v}_{t0}^2}{2UV}, \tag{3.8}$$

$$x_{A0} \equiv \frac{{\rm v}_{A0}^2}{2UV}, \tag{3.9}$$

where ${\rm v}_{t0}$ and ${\rm v}_{A0}$ are the dimensional turbulent speed of the gas and the Alfvén's speed, respectively, and $\sqrt{2UV} = \varpi\kappa \sin i/m$ is the normalization factor for velocities in the perpendicular direction to the spiral arm. Note that we adopt a logaroptic equation of state, such that the vertically integrated pressure has the form, $\Pi_{\rm turb} = \Sigma_0 {\rm v}_{t0}^2 \ln(\Sigma/\Sigma_0)$ in this paper.

Group II The dimensionless parameters in Group II are $\tan i$ and Ω/κ. In general, these two parameters are not arbitrary in a sense that we usually have good measurements of the pitch angle of a spiral arm and the rotation curve.

Group III and Other Dimensional Variables This group of parameters consists of the perpendicular separation between spiral arms, $L_{\rm arm}$, the pattern speed, $\Omega_{\rm p}$ and the half-height of the gas disk, z_0. They are the length and time scales of the problem. Note that the selection of parameters is not unique. Equivalently, one can specify other dimensional parameters, such as galacto-centric radius, ϖ, and rotational frequency $\Omega(\varpi)$ (or, $\kappa(\varpi)$) for the purpose of obtaining the dimensional values in length and time. These dimensional parameters also fix the scales of gas surface density and magnetic field. From Equation (3.7), we can write the gas surface density as $\Sigma_0 = \alpha\Sigma_{\rm A}$, where

$$\Sigma_{\rm A} \equiv \left(\frac{\varpi \sin i}{m}\right)\frac{\kappa^2}{2\pi G} = \frac{\kappa^2 L_{\rm arm}}{4\pi^2 G} \tag{3.10}$$

is a scale of gas surface density set by the galactic parameters. In general, $\Sigma_{\rm A}$ is large compared to the realistic gas surface density. Using the typical numbers for the Solar neighborhood[1], we have $\Sigma_{\rm A} = 26\,{\rm M}_\odot\,{\rm pc}^{-2}$. Thus, we expect the value of α to be around 0.5 or less. For the background magnetic field in the azimuthal direction, we have

$$B_{\varphi 0} = (\alpha x_{\rm A0})^{1/2}\left(\frac{\varpi \sin i}{m}\right)^{3/2}\frac{\kappa^2}{(G z_0)^{1/2}}, \tag{3.11}$$

where z_0 is the scale-height of the gas disk. In the Solar neighborhood, we have

$$B_{\varphi 0} = 20.3\,(\alpha x_{\rm A0})^{1/2}\mu{\rm G}, \tag{3.12}$$

where we take $z_0 = 100\,{\rm pc}$. For comparison to previous numerical simulations, such as Kim & Ostriker (2002, 2006), we provide the conversion formulae for the Toomre's parameter, Q_0, plasma beta, β_0, and an alternate definition of the strength of spiral potential, F (c.f., Equation 8 of Paper I):

$$Q_0 \equiv \frac{\kappa a_0}{\pi G \Sigma_0} = \frac{2}{\alpha}(x_{\rm t0} + x_{\rm A0})^{1/2}, \tag{3.13}$$

$$\beta_0 \equiv x_{t0}/x_{A0}, \tag{3.14}$$

$$F = \left(\frac{\kappa}{\Omega}\right)^2 \frac{\sin i}{m} f, \tag{3.15}$$

where we denote $a_0^2 = {\rm v}_{\rm t0}^2 + {\rm v}_{\rm A0}^2$, as the average value of effective sound speed.

[1] Here we use $\varpi_0 = 8\,{\rm kpc}$, $i = 15^o$, $m = 4$ and $\kappa = 37\,{\rm km\,s^{-1}kpc^{-1}}$.

3.4 Basic State

The basic state of the problem is the large scale spiral shock that has been investigated extensively in the literature. In our formulation, the spiral shock solution depends on the five galactic parameters in Group I. The purpose of this section is to investigate the dependence of the basic state on these parameters and lay the foundation to study the feathering instability. In particular, we focus on the effects of gas self-gravity and magnetic field.

3.4.1 Self-gravity of the Gas

The self-gravity of the gas can be important when the gas surface density Σ_0 is high. However, the implementation of the self-gravity into the nonlinear gas response calculation is not easy. One of the complications is due to the Poisson equation, in which the perturbation on the gravitation potential at one point depends on the perturbed density at all locations. The presence of the shock and sonic point in the solution of purely hydrodynamical calculation suggests that any spectral methods require special care, which would not otherwise be able to handle those special points. For example, Lubow et al. (1986) were able to obtain smoothed shock solutions with both viscosity and self-gravity. In our inviscid theory, we demonstrated in Paper I that self-gravitating solution can be found using iteration technique. In particular, we start our calculations for the non-self-gravitating case and increase gradually the value of the self-gravity parameter, α, until a maximum value with converged solution is obtained.

On the other hand, when the gas surface density is extremely high, it may have an effect on the stellar spiral density wave and alter the stellar gravitational potential. For example, Lubow et al. (1986) includes the higher order modes of the stellar spiral density-wave in their formation. Although we include only the fundamental mode of the stellar wave, it is instructive to calculate the gas density profile in their paper using the galactic parameters in the Solar neighborhood. In particular, we study the model C in their paper, in which the gas surface density is 10% of the stellar surface density at the spiral arm. The importance of the self-gravity of the gas is generally depending on the gas surface density. In our formulation, the parameter α compares the free-fall time scale and the corresponding time scale of flow in the η-direction (which is set by κ). To keep things simple, we study only the gas response, but do not include the back-reaction of the gas to the stellar spiral density-wave.

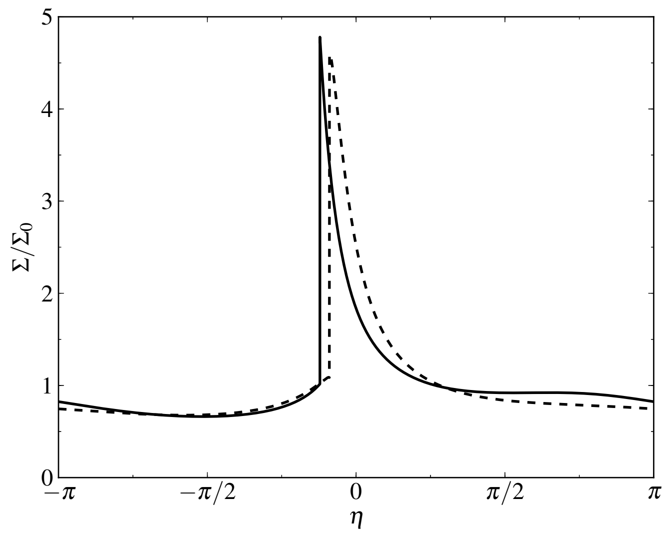

Figure 3.1: Normalized shock profiles with the presence of gas self-gravity (α = 0.13, dashed line) and the case without (α = 0, solid line). The mean surface density is Σ_0 so that the area under each curve is 1. The horizontal axis is the displacement from the minimum location of the stellar spiral potential.

Here we show some results using the same set of galactic parameters of model C in Lubow et al. (1986), with the exception of the parameters, x_{t0}, x_{A0} and α. Because of our adoption of logatropic equation of state, the turbulence pressure in the compression region is lower than the corresponding thermal pressure using the typical value of 8 $\sim$ 10 km s^{-1} of turbulent (or thermal sound) speed. This leads to higher compression at the shock in our calculation (4 $\sim$ 5 times compared to the 2 $\sim$ 3 times of the mean surface density in their paper). In general, the maximum converged values of α in our calculations are lower than the corresponding α = 0.26 in their paper (based on 10% gas mass compared to the stellar spiral arm) unless the magnetic field is strong enough (see Figure 3.2). Note that the limit on α also depends on the strength of stellar spiral potential F, in which stronger stellar spiral potential can support larger amount of gas. Quantitatively, we find that the increase in α leads to a spiral shock at a further downstream location, but does not always enhance the amount of relative peak compression ($\Sigma_{\rm peak}/\Sigma_0$) in the spiral arm (especially for the case with weak magnetic field, e.g., $\beta_0 = 20$ in Figure 3.1). This is one of the reasons why the non-magnetic calculations in Lubow et al. (1986) only show a decrease of relative peak compression for increasing α. However, in terms of dimensional unit (i.e., multiplying with a factor of $\Sigma_{\rm A}$), the peak surface density is generally increasing with α. On the other hand, viscosity and the back-reaction on the stellar spiral potential by the gas in their formulation have been shown to smoothen the shock and lead to weaker compression. In Figure 3.2, we show the shock profiles for different values of Alfvén's speed parameter. The compression is lowered with the presence of the magnetic field. We will discuss the effect of magnetic fields in the next section.

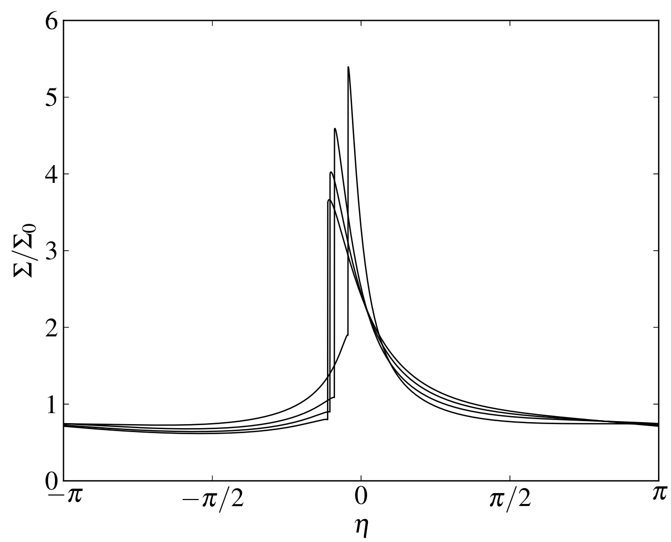

Figure 3.2: The shock profiles for different values of the Alfén's speed parameter ($x_{\rm A0} = 0.01, 0.05, 0.09, 0.13$ from stronger to weaker compression at the shock).

3.4.2 Magnetic Field

The magnetic field lines in the basic state follow with the streamlines due to the freezing-in assumption. As a result, the magnetic field provides extra pressure against the spiral shock compression in the η-direction. Under the tight-winding spiral assumption, the magnetic tension which is proportional to $\sin i$ is ignored in the current formulation, and hence the streamlines are closed. In general, the magnetic field does not have significant effect on the basic state except for the broadening on the density enhancement. Figures 3.3 and 3.4 show the effects of the parameters $x_{\rm A0}$ (magnetic) and α (self-gravity) on the (normalized) peak surface density of the gas and the width of the spiral arm, respectively. We also overlay them with the strengths of average background magnetic field ($B_{\phi 0}$) as the white contours. The blank region on the top-left corner is where no solution is found for the combination of the parameters. Thus, the upper boundary of the color region can be interpreted as the line of maximum allowed values of α along the Alfvén's speed parameter $x_{\rm A0}$. Above the line, the self-gravity of the gas is too strong for a steady-state solution.

For low value of $x_{\rm A0}$, the normalized peak surface density is generally higher and reaches more than 15 times of the average gas surface density. This is expected because the square of effective sound speed as a sum of the turbulent and Alfvén's speed parameters, $x_0 = x_{\rm t0} + x_{\rm A0}$ is smaller. In this region (left of the figure), there is not enough pressure and the maximum value of α is lower as well. In other words, magnetic field has the stabilizing effect against the self-gravity by providing extra pressure. For the width of the gaseous spiral arm (see, Figure 3.4), we use the perpendicular distance between the locations of the shock and the sonic point, which reads

$$W = (\eta_{\rm sp} - \eta_{\rm sh})L_0, \tag{3.16}$$

where $\eta_{\rm sp}$ and $\eta_{\rm sh}$ are the η-coordinates of the sonic point and shock, respectively. In general, the width increases with larger Alfvén's speed ($\propto \sqrt{x_{\rm A0}}$) but has weaker dependence on the gas self-gravity (α). Next, we show the dependence of the shock location, which is given by $\eta_{\rm sh}L_0$, on the two parameters in Figure 3.5. It has a stronger dependence on α than on $x_{\rm A0}$, in which higher value of α trends to shift the shock downstream.

For realistic values of the magnetic field and gas surface density, we should focus on the left-bottom part of the color region. In this particular model with a sharp spiral shock, $L_{\rm arm}$ is 2.25 kpc and the width of the gaseous spiral arm is around 10% or less. Next, we use $(x_{\rm A0}, \alpha) = (0.02, 0.15)$ as the reference. We show the shock profiles by varying α (see Figure 3.6) and $x_{\rm A0}$ (see Figure 3.7) separately, which represent the solutions along a vertical line and a horizontal line on the x_{A0}-α space, respectively.

In Figure 3.6, we show the profiles of the spiral shock for different values of α in dimensional units. The horizontal axis is the displacement from the minimum location of the stellar spiral potential (i.e., ηL_0). The vertical axis is the gas surface density. The area under the curve is proportional to the total gas mass in our calculation region, and therefore proportional to α.

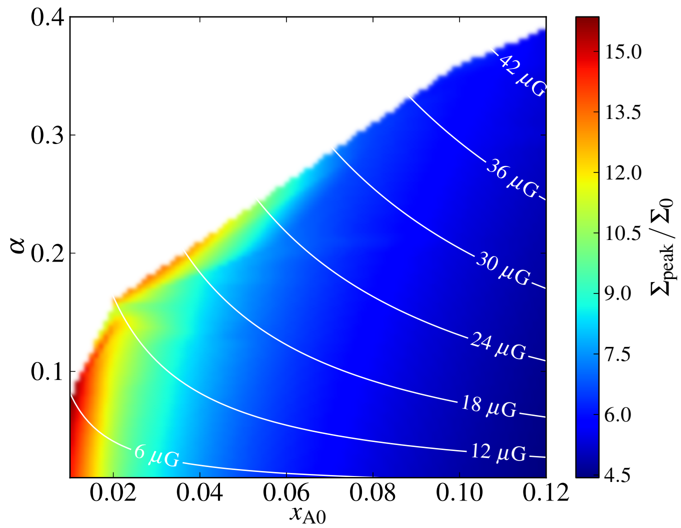

Figure 3.3: The color-coded region shows the normalized peak surface density of the gas (i.e., maximum value of $1+\hat{\sigma}$). The horizontal and vertical axes are the magnetic and self-gravity parameters, respectively. The white contours represent the mean circular magnetic field (μG). The parameters at the left-bottom corner are $\alpha = x_{A0} = 0.01$ and the grid resolution is 0.01 in both parameter directions.

3.4.3 Streaming Motion

The streaming motion is characterized by the non-circular motion of the gas due to the spiral arm. In particular, the post-shock gas velocity determines how strong the spiral shock and the corresponding shear near the spiral arm. The magnitude of such streaming velocity can be defined as the difference between the fluid velocity and the

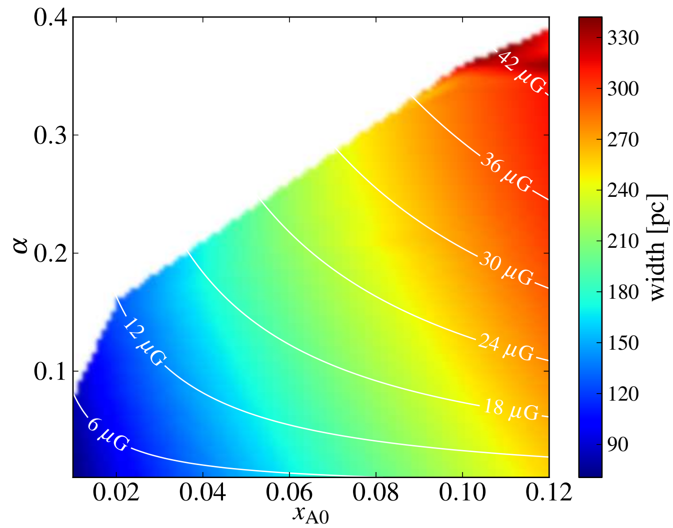

Figure 3.4: At the same parameter space, we show the width of the gaseous spiral arm, defined as the distance from the shock location to the sonic point.

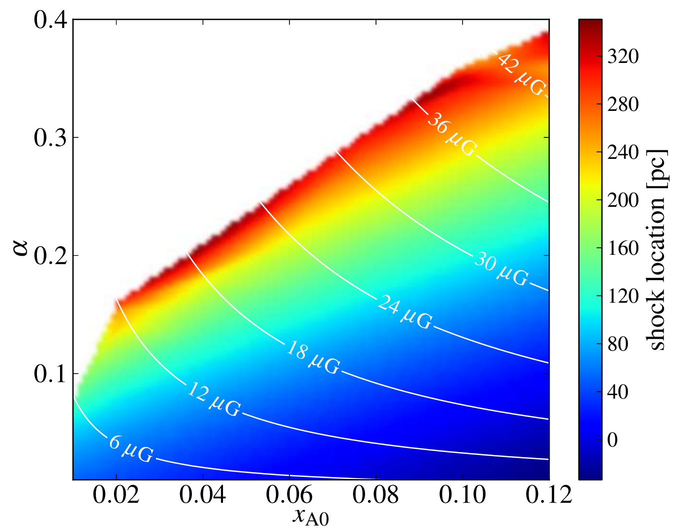

Figure 3.5: At the same parameter space, we show the shock location ($\eta_{\rm sh}$) as the distance of the minimum location of the stellar spiral potential ($\eta = 0$). The arm-to-arm distance $L_{\rm arm} = 2.25\,$kpc.

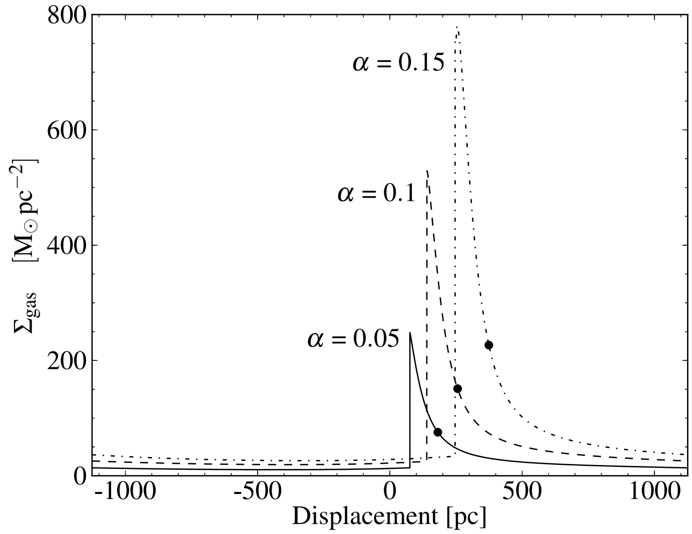

Figure 3.6: Typical spiral shock profiles for different values of α (at $x_{A0} = 0.02$). These curves based the parameters that lie on a vertical line on the parameter space such as in the Figure 3.3. The horizontal axis is the displacement from the minimum location of the stellar spiral potential. The vertical axis is the dimensional gas surface density which makes use of the conversion factor Σ_A. The black dots are the sonic point values.

background circular velocity:

$$u_s = |\mathbf{u} - \mathbf{u}_0| = \sqrt{u_{\eta 1}^2 + u_{\xi 1}^2}, \tag{3.17}$$

where $\mathbf{u}_0 = \varpi(\Omega - \Omega_p)\hat{e}_\varphi$ is the circular velocity in the pattern frame; $u_{\eta 1}$ and $u_{\xi 1}$ are the nonlinear perturbation due to spiral potential in the η- and ξ-directions, respectively. Figure 3.8 shows the profiles of u_s for $f = (0.3, 0.4, 0.5)$. The narrow, sharp peaks correspond to the spiral shock (discontinuity in $u_{\eta 1}$) in this particular model with low effective sound speed ($x_{t0} = 0.022$ and $x_{A0} = 0.03$). Except in the region near the shock, the magnitude of the streaming velocity does not vary significantly before or after the gas passing through the spiral shock. Also, the magnitude of the streaming velocity scales roughly with the measure of the spiral potential, f. This can be a potentially useful measure for estimating f (or F) observationally, in which only averaged quantities are needed. On the other hand, the direction of the streaming motion changes gradually as the gas moves across the spiral arm. This is because u_η accelerates from

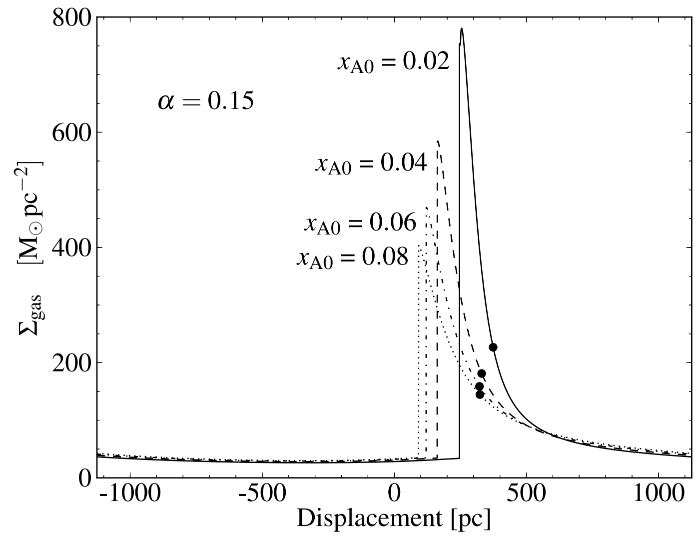

Figure 3.7: Typical spiral shock profiles for different values of x_{A0}, with the black dots indicating the sonic points.

sub-magnetosonic speed to super-magnetosonic speed from one spiral shock to another (without any sign change).

3.4.4 Arm Crossing Time

The time for a fluid to move from one spiral arm to the next arm is determined by the galactic parameters, but does not depend on the Group I parameters. In particular, this total arm-crossing time is a constant given by $t_{cross} = 2\pi/m(\Omega - \Omega_p)$, which is the same as the absence of spiral perturbation. This is indeed an expected result because the reciprocal of the dimensionless η-velocity $1/(-\nu + \hat{u}) = (1 + \hat{\sigma})/(-\nu)$ is a periodic function due to the closure of streamlines. Therefore, the spiral perturbation of the basic state does not change the total arm-crossing time. However, the time for a fluid parcel to displaces from the shock to a particular location η will change. This can be calculated

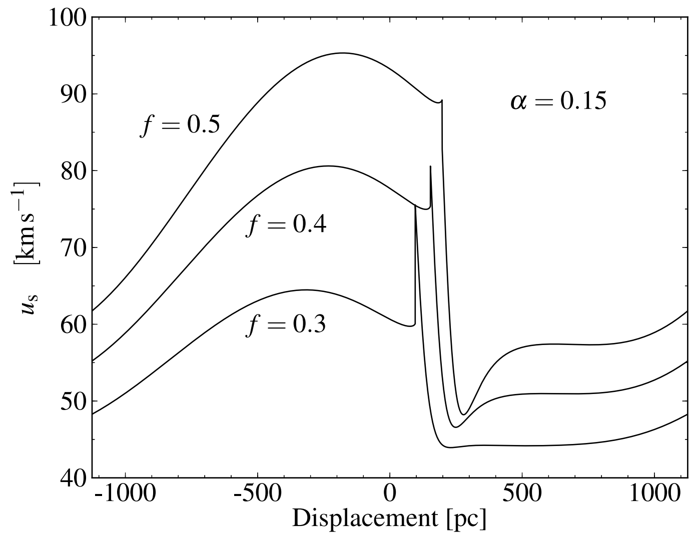

Figure 3.8: Typical profiles for the magnitude of streaming motion along the perpendicular displacement from the spiral arm.

by

$$t(\eta) = \int_{\eta_{\rm sh}}^{\eta} \frac{L_0}{u_\eta(\eta)} d\eta = \frac{1}{m(\Omega - \Omega_{\rm p})} \int_{\eta_{\rm sh}}^{\eta} (1 + \hat{\sigma}) d\eta, \tag{3.18}$$

where $\eta_{\rm sh}$ is shock location. The integral can be further evaluated using the differential equations for the basic state, which gives $(\eta - \eta_{\rm sh}) + [\hat{\rm v}(\eta) - \hat{\rm v}(\eta_{\rm sh})]$, where $\hat{\rm v}$ is the ξ-component of velocity due to the spiral perturbation. The integrand of Equation (3.18) implies that the stronger the shock, the longer the time for the fluid to reach the interarm region. On the other hand, the super-magnetosonic flow in the pre-shock region will compensate the time spent getting out the spiral arm, and keep the total time constant.

In Figure 3.9, we show the fractional arm-crossing time (i.e., $t(\eta)/t_{\rm cross}$) for a test particle moving from the shock to the interarm region. The curves have the same end points because the total arm-crossing times are the same. For the strong spiral shock in this case ($x_{\rm t0} = 0.022$ at $\varpi = 2\,{\rm kpc}$), the test particle would take a long time to move into the interarm region. In particular, it takes around half of the crossing time spending in the spiral arm region (i.e., around 10% of the arm-to-arm distance, labeled by the vertical dashed line). We also show the arm-crossing time due to the circular flow without spiral perturbation as the gray diagonal across the figure. The top horizontal axis shows the corresponding angular scale (in degree) in the perpendicular direction to the spiral arm, such that the perpendicular displacement, d is given by

$$d = \varpi \Delta\Theta_{\perp},$$

where $\Delta\Theta_{\perp}$ is converted into radian. We can see that the presence of spiral shock reduces the flow speed and increases the time for displacement near the shock for a factor of 3-4. This is

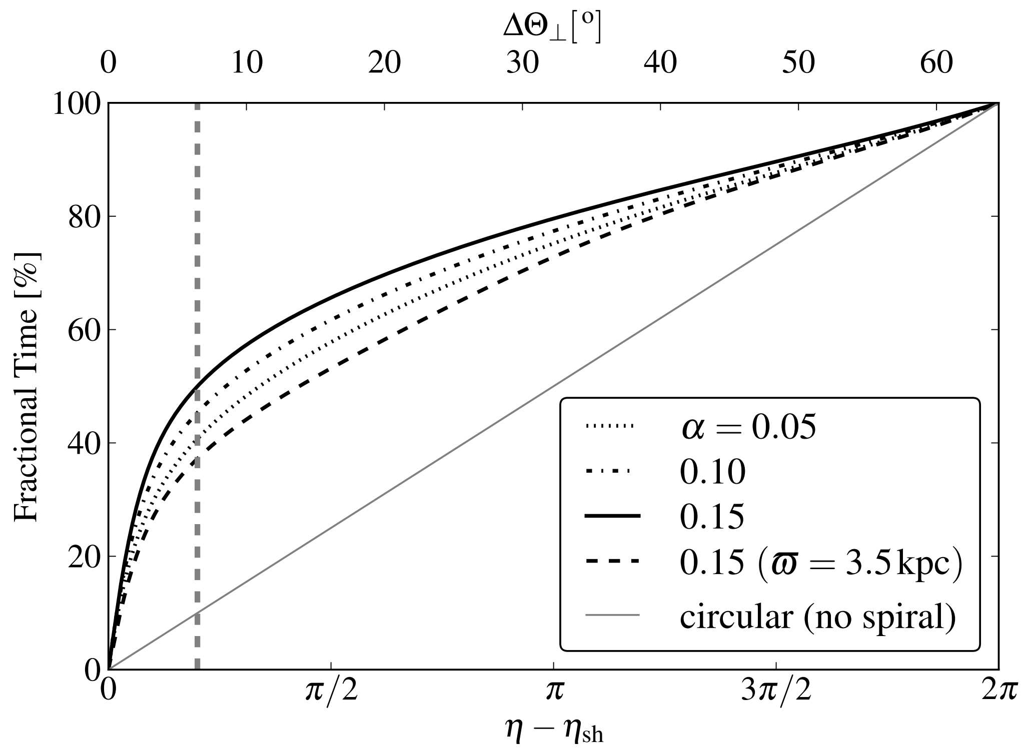

Figure 3.9: A plot of the fractional arm-crossing time for a test particle moving from the shock to the interarm region. The vertical thick gray dashed line locates the position at 10% arm-to-arm distance away from the shock.

3.5 Feathering Instability

In this section, we present the parameter study of the feathering instability. We focus on the effect of the self-gravity and magnetic field. In our linear stability analysis, we study the perturbation for a single ξ-wavenumber, l. Each solution has four components: $\tilde{\sigma}_l$, $\tilde{u}_l$, $\tilde{\mathrm{v}}_l$, and $\tilde{A}_l$, where $\tilde{\sigma}_l$, $\tilde{u}_l$, and $\tilde{\mathrm{v}}_l$ have their usual meanings and $\tilde{A}_l$ is z-component of the perturbational magnetic vector potential. The method of solution is presented previously in Section 2.4.4. Readers may also consult Appendix A for the detail on computing the solution using publicly available numerical solver for boundary value problems.

As we assume the two-dimensional solution is periodic in ξ, a perturbation at a wavenumber l will give the spacing of feathers (i.e., separation between peaks of density enhancement) that reads

$$\lambda_f = \left(\frac{\tilde{L}}{|l|}\right) L_{\mathrm{arm}}, \tag{3.19}$$

where $l/\tilde{L}$ is the effective wavenumber. Note that the wavenumber l takes integer values, and asymptotically equals to the number of feathers can be found on a spiral arm from 0 to 180 degrees for two-arm spiral structure (TASS) (i.e., $360/m$ degrees for m-arm spirals) . In our formulation (c.f., Section 2.4.3), we define $\omega_{\mathrm{T}} \equiv \omega - (l/\tilde{L})\hat{\mathrm{v}}_{\mathrm{T}}$ to be the dimensionless Doppler-shifted frequency in the moving frame of the background flow along the spiral arm. In practice, we take $\hat{\mathrm{v}}_{\mathrm{T}} = -\nu/\tan i$ as we previously did for the background flow. Thus, ω_{T} is an unknown eigenvalue to be determined from the integration. We look for the perturbations with positive growth rate which grow exponentially and lead to nonlinear development of overdense regions.

The reference model used in this section is similar to the one in the last section, which is based on the galactic parameters for the inner part of M51 galaxy (i.e., $\varpi = 2\,\mathrm{kpc}$. As a result, both turbulence and Alfvén's speed parameters are relatively small (i.e., $\lesssim 0.1$). The spiral forcing parameter is $f = 0.5$. The radial dependence of the galactic parameters is discussed in Appendix 3.A.

3.5.1 General Properties

We obtain the solution of the feathering perturbation as a function of η from numerical integration. For each value of l, we calculate the eigenfunctions and the corresponding complex eigenvalues, ω_{T}. In general, there are multiple eigenvalues and eigenfunctions for each value of l. In particular, there are multiple branches of solution (i.e., the complex frequency ω_{T} as a "continuous" function of l that does change rapidly). To ensure that we follow the solution of the same branch when we increase l, the steps of increment are smaller than 1 in practice (e.g., 0.01). Here we study the branch of solution in which $\mathrm{Re}(\omega_{\mathrm{T}}) \to 0$ when $l \to 0$. For the dependence of $\omega_{\mathrm{T}}(l)$ on l, we defer the discussion in the next subsection.

Table 3.2: List of Solutions

$l/\tilde{L}$	$\mathrm{Re}(\omega_{\mathrm{T}})$	$\mathrm{Im}(\omega_{\mathrm{T}})$	Figure #
1.0	0.235	-0.239	3.10
2.0	0.208	-0.655	3.11
2.0	0.0155	0.00553	3.12
4.368	0.187	-0.947	3.13

Next, we present the complex eigenfunctions for a set of l (Figures 3.10-3.13). The complex eigenvalues of ω_{T} are given in Table 3.2. Except for Figure 3.12, which is chosen from a branch of decaying solutions, the other solutions have positive growth rates (-$\mathrm{Im}(\omega_{\mathrm{T}})$), and grow exponentially. The arbitrary complex multiplicative constant of the linear solution is chosen such that $\tilde{\sigma}_l(\eta)$ is $1 + 0i$ at immediately after the shock (i.e., zero of the η-axis). Note that the amplitudes of different eigenfunctions should not be compared directly. In general, the solution varies rapidly in the beginning and decreases slowly for larger η. Also, the end points of the solution are not necessary zero because they are determined by the shock jump conditions.

In addition, higher l generally gives a more oscillatory solution in η. However, this is partly due to the increase in stiffness of the ODEs (c.f., Equation (A.16) in Appendix A). We did not investigate this numerical artifacts in this thesis work, but this is possibly solvable by considering a proper matching condition at the critical point of the ODEs.

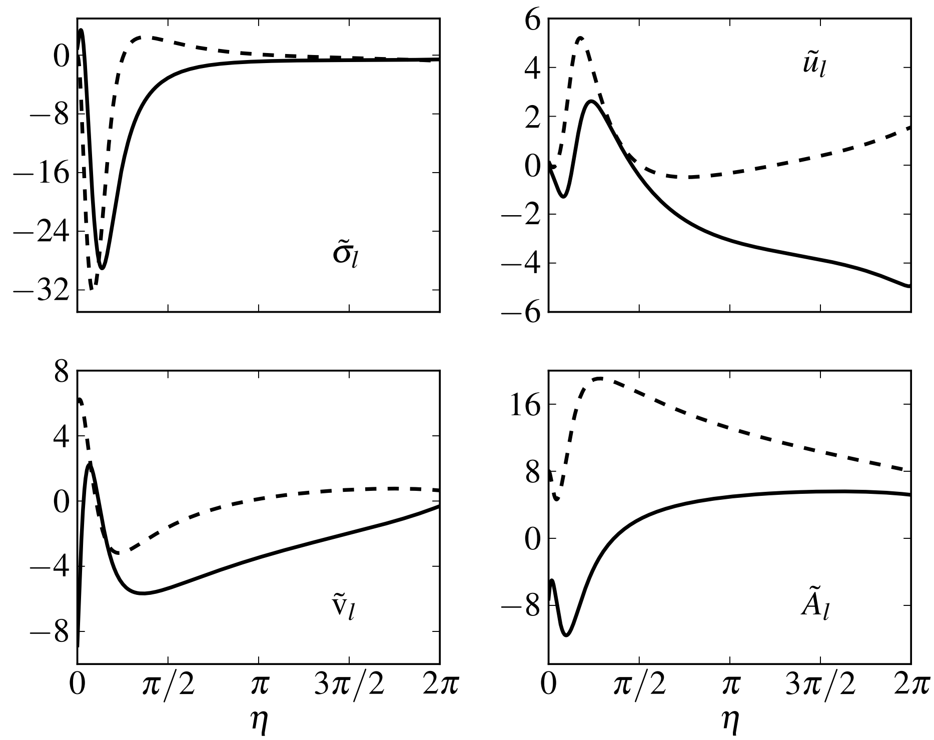

Figure 3.10: An unstable mode for $l/\tilde{L} = 1.0$. The eigenfunctions (from top to bottom, from left to right) are $\tilde{\sigma}_l$, $\tilde{u}_l$, $\tilde{v}_l$, and $\tilde{A}_l$. The solid and dashed lines represent the real and the imaginary parts, respectively. The η-axis is measured from the shock front. The amplitude is chosen such that $\tilde{\sigma}(0) = 1$.

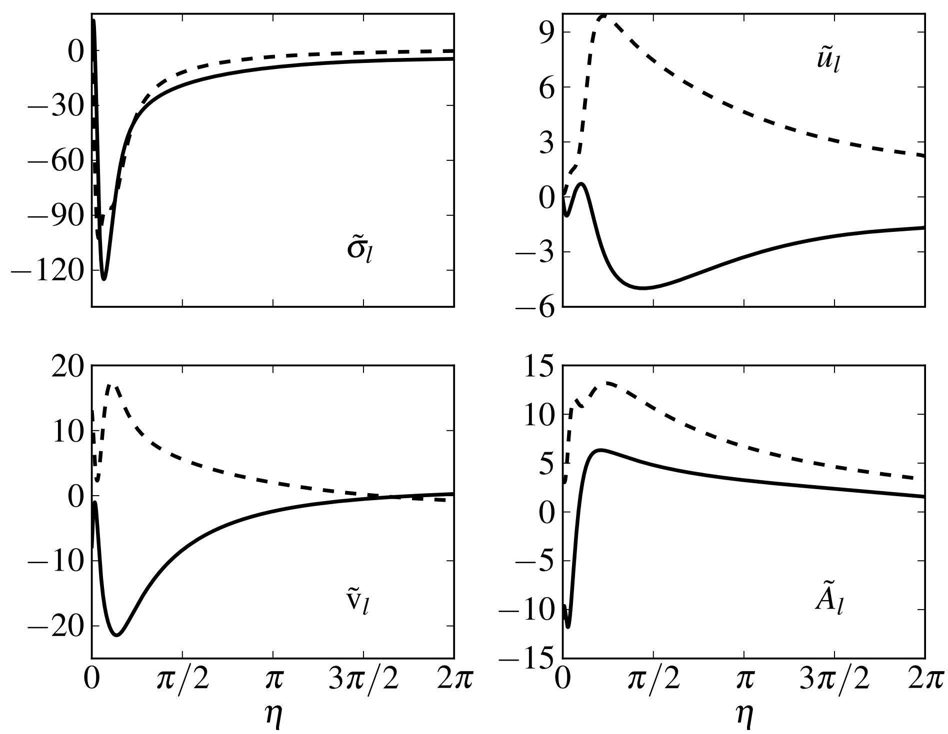

Figure 3.11: Same plot as Figure 3.10 but for an unstable mode at $l/\tilde{L} = 2.0$ (upper branch).

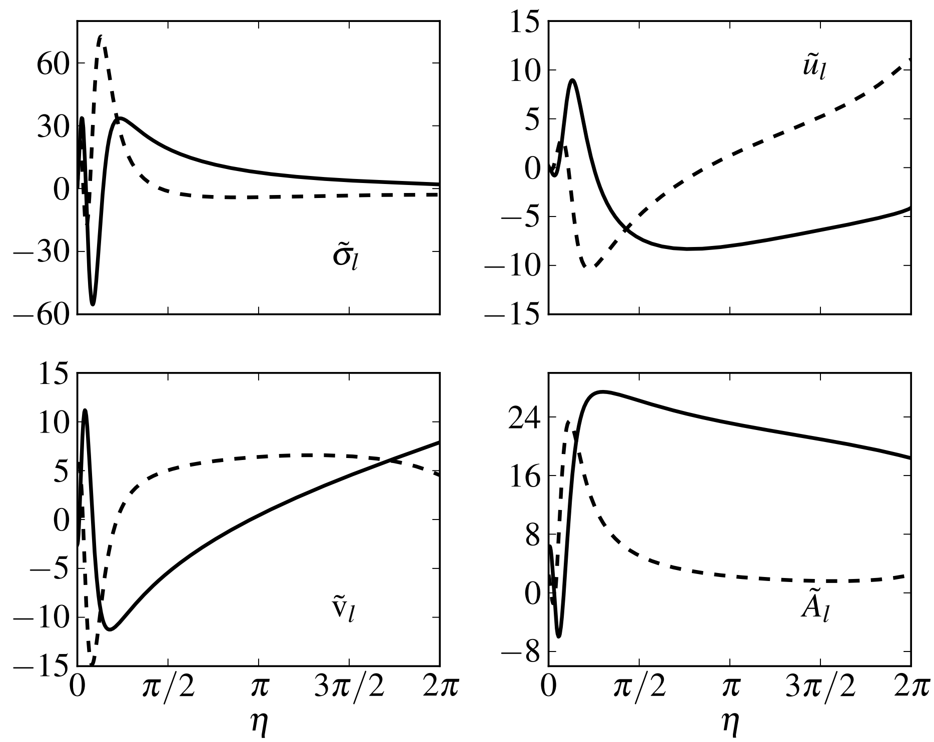

Figure 3.12: Same plot as Figure 3.10 but for a stable mode at $l/\tilde{L} = 2.0$ (lower branch).

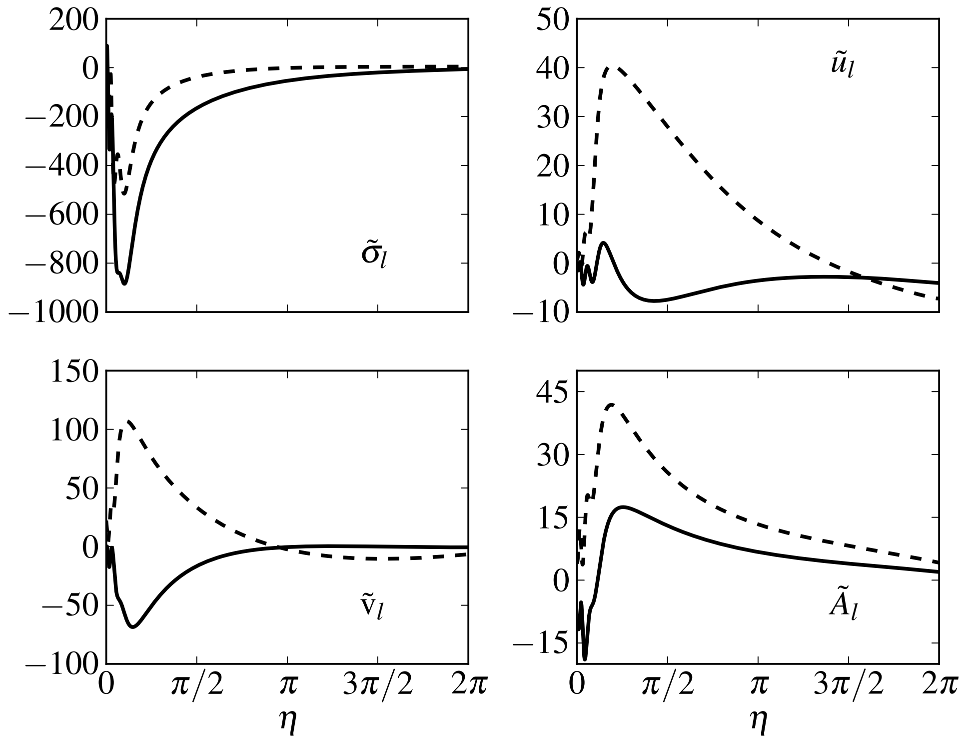

Figure 3.13: Same plot as Figure 3.10 but for an unstable mode at $l/\tilde{L} = 4.368$. This is the mode with the maximum growth rate as shown in Figure 3.15.

3.5.2 Growth Rates

The growth rate of the feathering perturbation depends sensitively on l. In Figures 3.14 and 3.15, we show an example of bifurcation of ω_{T} along l. The lower branch of growth rate decreases with l and starts to become negative around $l/\tilde{L} = 2$ where the solution becomes stable and decays exponentially in time. For the upper branch, the growth rate reaches the maximum at $l = 12$ (i.e., $l/\tilde{L} = 4.368$). The mode with maximum growth rate should grow fastest and provide the characteristic spacing between feathers. We show the eigenfunctions of this mode in Figure 3.13. In this case, with $\varpi = 2\,\mathrm{kpc}$ and $L_{\mathrm{arm}} = 2.25\,\mathrm{kpc}$, the feather spacing is 515 pc. This value agrees with the findings in La Vigne et al. (2006) (e.g., Figure 21 in their paper). Also, this mode has a small group velocity relative to to the local circular flow, which is indicated by the horizontal branch of $\mathrm{Re}(\omega_{\mathrm{T}})$ in Figure 3.14 (i.e., $d\mathrm{Re}(\omega_{\mathrm{T}})/dl \simeq 0$).

3.5.3 Dependence on Self-gravity

The dependence of the characteristic value ω_{T} on the self-gravity and magnetic field is rich in features due to the complexity of the problem. In general, the growth rate of the instability is higher for stronger gas self-gravity. We show a few upper-branch curves of ω_{T} in Figures 3.17 and 3.18 for their real parts and growth rates, respectively. The curves are sensitive to the parameter α. In our particular example, it changes certain behaviors between $\alpha = 0.15$ and 0.12. The branch point at around $l/\tilde{L} = 1$ (as seen in Figure 3.15) disappears for lower α. The curve of $\alpha = 0.12$ passes this point smoothly. We did find a separate lower branch with decaying solution, but it is not attached to other branch at any l. In any case, the general properties of curves are similar and are expected for gravitational instability, namely: for weaker self-gravity, the growth rate decreases and the most unstable mode shifted toward lower l.

3.5.4 Self-gravity with Exact Solution for the Poisson Equation

So far we have adopted a simplified solution (i.e., $\tilde{\phi}_l = -\tilde{\sigma}_l/|l/\tilde{L}|$) for the Poisson equation of the gas (c.f., Appendix 2.A of Chapter 2). In this subsection, we examine the solutions without the assumption that η-wavenumber, n is small compared to the

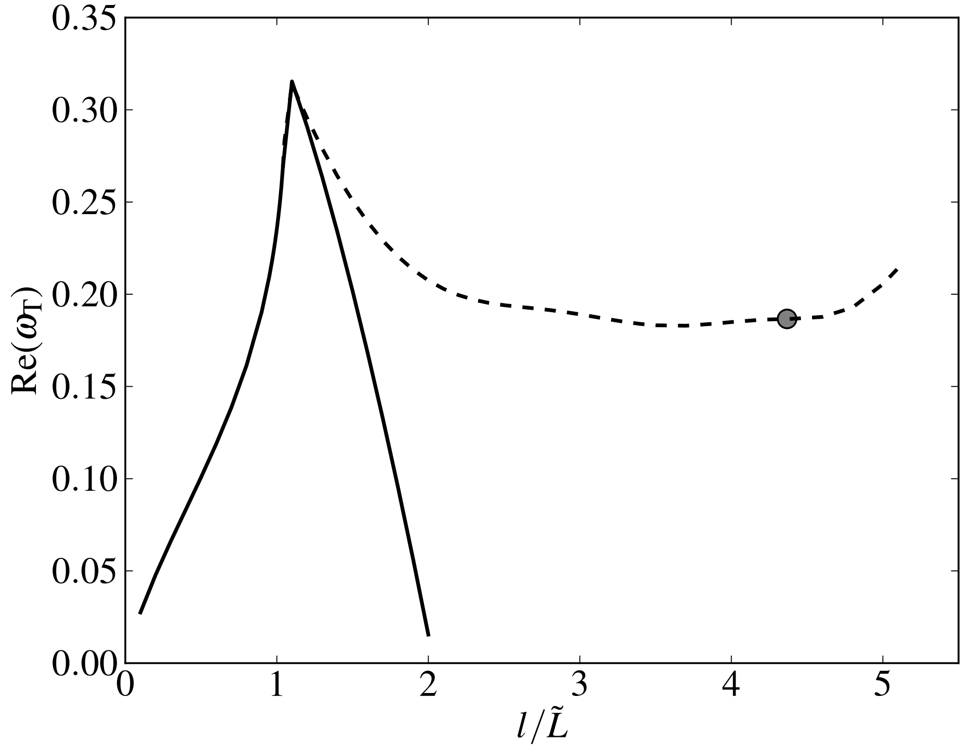

Figure 3.14: Real part of ω_{T} along l. The dashed line corresponds to the upper branch of the growth rate in Figure 3.15. The gray point at $l/\tilde{L} = 4.368$ represents the solution with maximum growth rate.

effective ξ-wavenumber, $l/\tilde{L}$. We demonstrate that the simplified solution is able to capture the overall shape of the perturbational potential $\tilde{\phi}$ by comparing to the exact solution, and its use is justified. The dimensionless, perturbational Poisson equation (Fourier-transformed in ξ) reads

$$\left(\frac{\partial^2}{\partial\eta^2} + \frac{\partial^2}{\partial\zeta^2} - \frac{l^2}{\tilde{L}^2}\right)\tilde{\phi}_l(\eta,\zeta) = 2\tilde{\sigma}_l(\eta)\delta(\zeta), \tag{3.20}$$

where $\zeta = z/L_0$ is the dimensionless coordinate perpendicular to the plane of the disk. The solution to the Poisson equation at the mid-plane ($\zeta = 0$) take the following form

$$\tilde{\phi}_{n,l} = -\frac{\tilde{\sigma}_{n,l}}{\sqrt{n^2 + (l/\tilde{L})^2}}, \tag{3.21}$$

where we require the exponentially decaying solution for the positive and negative ζ-directions. To obtain the gravitational force along η due to the perturbational surface

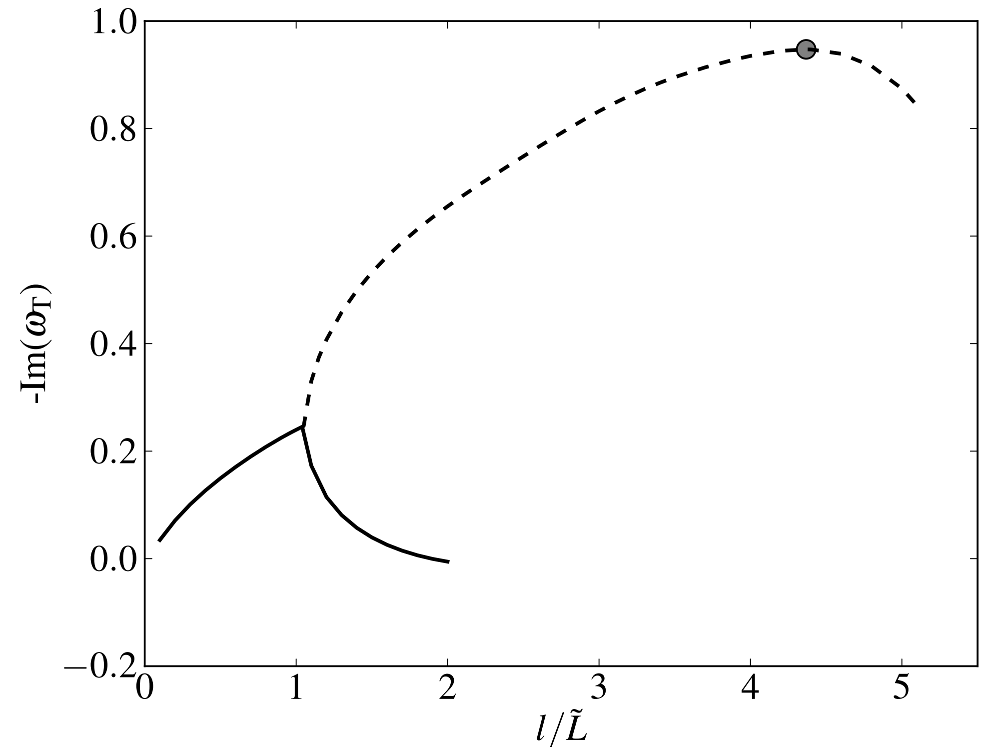

Figure 3.15: Growth rate (-Im(ω_{T})) along l. An upper branch (dashed line) and a lower branch (solid line) appear when $l/\tilde{L} > 1.04$. The gray point at $l/\tilde{L} = 4.368$ represents the solution with maximum growth rate.

density, a large number of terms is required because the Fourier component decays very slowly in n. This is why we seek for a simplified solution even if we choose to solve the equations iteratively. Fortunately, Equation (3.20), which is subject to the doubly periodic boundary conditions in η- and ξ-directions, can be solved exactly using the Green's function method. Readers can consult Appendix 3.B for the full calculation. Here we give the Green's function in the real space:

$$G_l(\eta - \eta', \zeta = 0) = -\sum_{k=-\infty}^{\infty} K_0(|(l/\tilde{L})(\eta - \eta' - 2\pi k)|), \tag{3.22}$$

where K_0 is the zeroth-order modified Bessel function of the second kind. When compared with this exact form, our original approximation captures the overall shape by replacing it with a series of periodic Dirac-delta functions (which leads to the $1/|l|$ factor

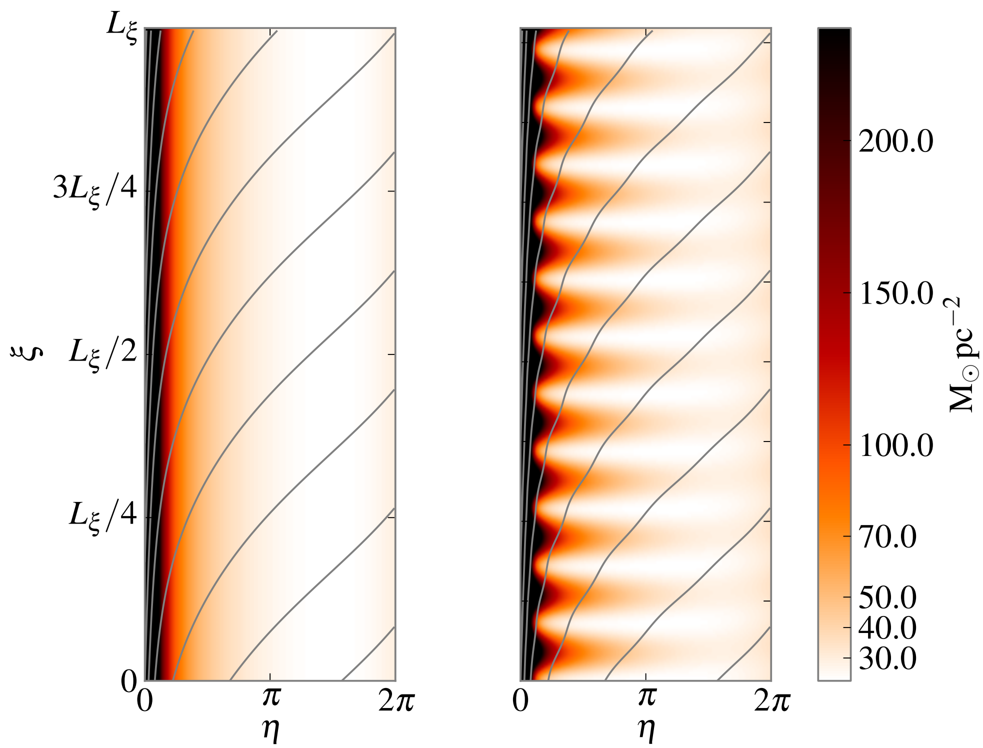

Figure 3.16: Plot of the surface density of the background flow (*left*) and the perturbed flow of the most unstable mode (*right*, $l = 12$). The surface density over $1/4$ of the peak value of the spiral shock is colored as black for better visualization of the feathers. The arbitrary amplitude of the perturbation is 0.002 in this case. The scale of the vertical axis is $L_\xi = L_{\rm arm}/\tan i$, where $i = 20^o$. The grey contours are the magnetic field lines.

in Fourier components). The gravitational force can be obtained from the convolution between the Green's function and the perturbtational gas surface density.

To obtain the solution with exact self-gravity, we calculate the desired solution iteratively with relaxation and use the solution from the simplified self-gravity as an initial guess. A converged solution can usually be obtained in a few iterative steps for each value of relaxation parameter.

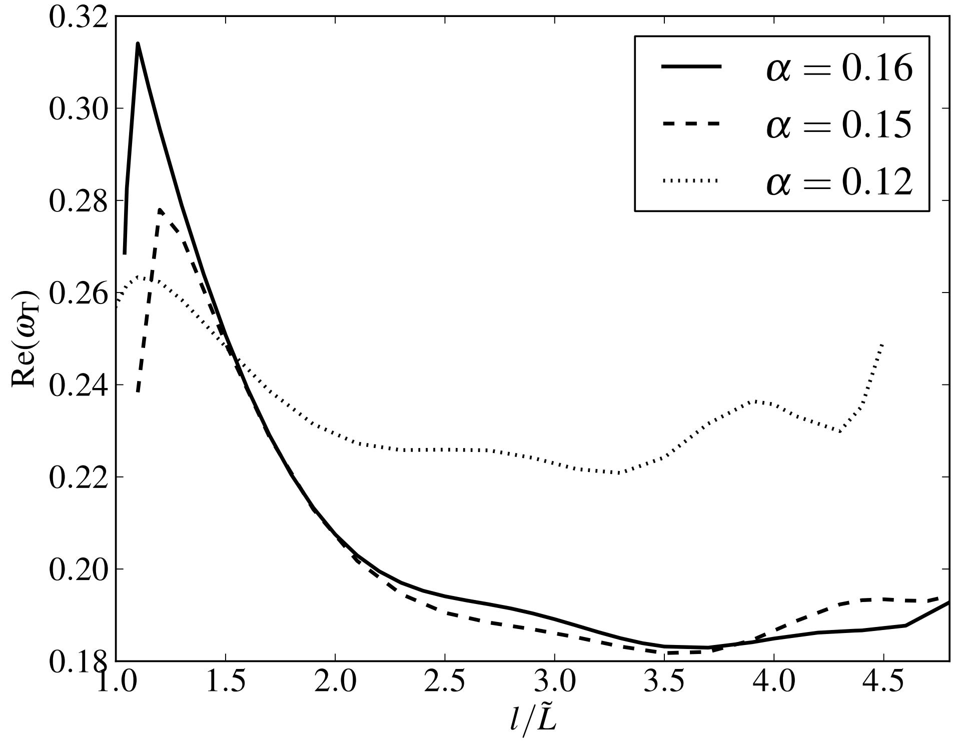

Figure 3.17: Real parts of ω_T along l for different α. The solid, dashed, and dotted lines are the real parts of ω_T for α = 0.16, 0.15, and 0.12, respectively.

3.6 Conclusion

In this chapter, we investigated the dependence of spiral shock and its feather instability on the different parameters in the problem. The self-gravity plays an important role in the feather instability, in which it enhances the growth rate of the unstable mode. We also demonstrated the mode with maximum growth rate gives the desired spacing of feathers, around 500 pc using the galactic parameters of M51 at $\varpi = 2\,$kpc.

Acknowledgments

Chapter 3, in full, is currently being prepared for submission for publication of the material. Lee, Wing-Kit. The dissertation author was the primary investigator and

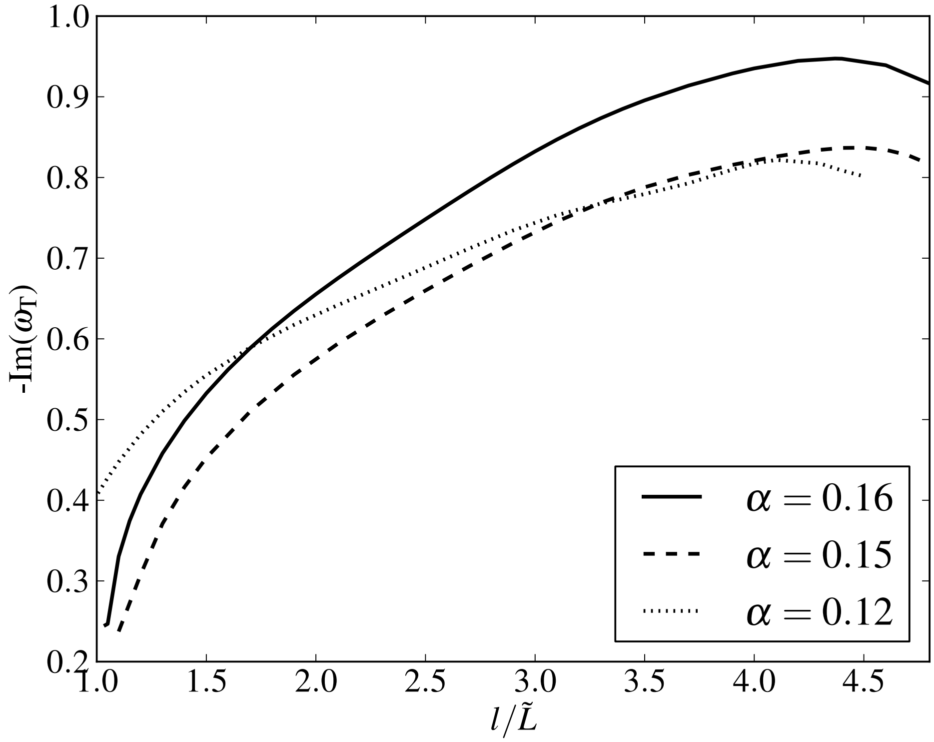

Figure 3.18: Growth rates along l for different α. The solid, dashed, and dotted lines are the growth rates of ω_T for α = 0.16, 0.15, and 0.12, respectively.

author of this material.

Appendix

3.A Radial Dependence of Parameters

In the application to a realistic galaxy, it is useful to compare the solutions at different radius. We examine the parameter space set by the galactic parameters in M51. In particular, we adopt the radial profile of the rotational frequency, $\Omega(\varpi)$ and epicyclic frequency, $\kappa(\varpi)$ in Sofue et al. (1999); the pattern speed, $\Omega_p = 38\,\mathrm{km\,s^{-1}kpc^{-1}}$ obtained by Zimmer at el (2004); a simple exponential form of the gas surface density, Σ_0 from Scoville and Young (1983). In Figure 3.A.1, we show the variation of the rotational and epicyclic frequencies, gas surface density, and the dimensionless parameters, as functions of radius. For the Alfvén's speed parameter, x_{A0}, its radial profile depends on the model. If the Alfvén's speed, v_{A0} is fixed, x_{A0} has the same trend as x_{t0} due to the same radial variation in the normalization. However, the Alfvén's speed, v_{A0} also depends on the magnetic field and the gas surface density.

3.B Derivation of the Solution to the Poisson Equation

In this appendix, we derive the solution to the Poisson equation in the thin-disk geometry, subject to double periodic boundary conditions in the η- and ξ-directions on the disk. The equation links the perturbational gravitational potential $\tilde{\phi}$ and surface density $\tilde{\sigma}$, and is crucial to the understand the role of self-gravity of the gas in the system. The perturbational Poisson equation (c.f. Equation (3.20)) can be solved by finding the appropriate Green's function. Consistent with the formulation of stability analysis, the equation is Fourier-transformed in ξ. The required Green's function is the

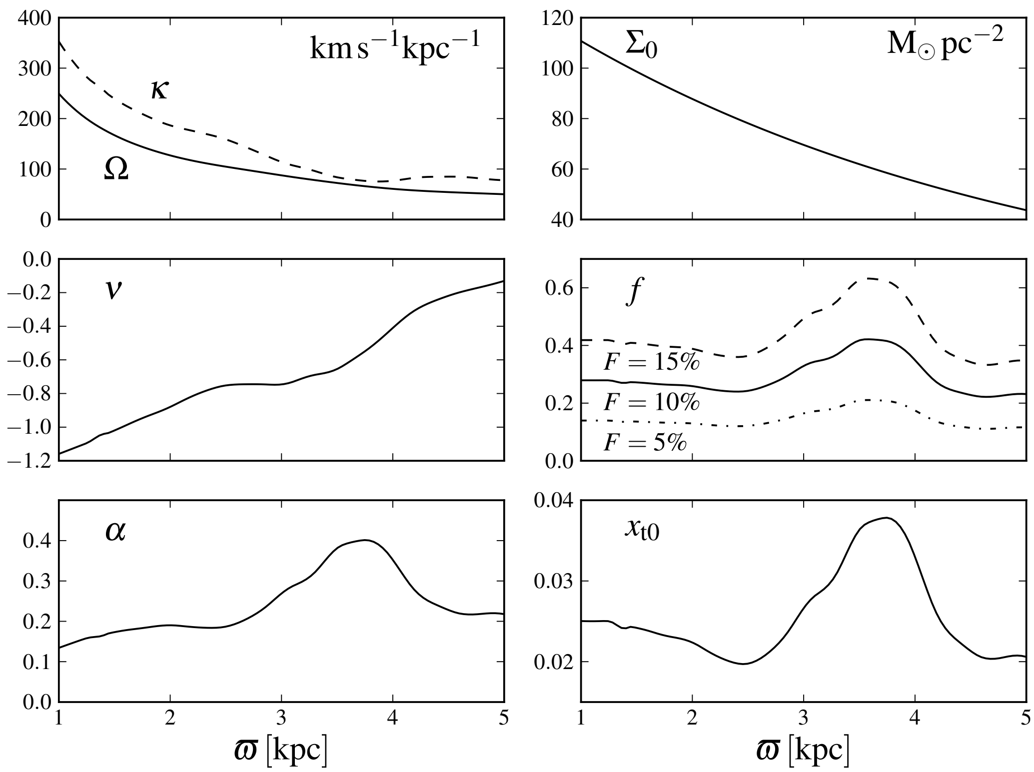

Figure 3.A.1: From top-left, in clockwise direction, the figures show the plots of Ω and κ, gas surface density (Σ_0), f, x_{t0}, α and ν, along the galacto-centric radius, ϖ. We use M51 as a reference for the rotational curve and gas surface density (see text), and adopt $v_{turb} = 10\,\mathrm{km\,s^{-1}}$ for the parameter x_{t0}.

solution to the following equation:

$$\left(\frac{\partial^2}{\partial\eta^2}+\frac{\partial^2}{\partial\zeta^2}-\frac{l^2}{\tilde{L}^2}\right)\tilde{G}_l(\eta-\eta',\zeta-\zeta')=2\delta(\eta-\eta')\delta(\zeta-\zeta'),\tag{3.B.1}$$

where G_l is periodic in η and decaying in ζ. The solution of Equation (3.20) at the mid-plane is thus

$$\tilde{\phi}_l(\eta)=\int_0^{2\pi}G_l(\eta-\eta',\zeta=0)\tilde{\sigma}_l(\eta')d\eta'.\tag{3.B.2}$$

The standard way to obtain G_l is to first solve for the free-space case (where the solution decays to zero at $\eta\to\pm\infty$) and to construct a summation series to match the periodic boundary condition. The free-space Green's function g_l, is the solution to the equation of the same form as Equation (3.B.1), but is subject to the boundary conditions: $g_l\to 0$ where $\eta\to\pm\infty$ or $\zeta\to\pm\infty$. The symmetry in η and ζ permits the use of polar coordinates and the assumption of $g_l=g_l(\rho)$ where $\rho=[(\eta-\eta')^2+(\zeta-\zeta')^2]^{1/2}$ is the radial coordinate. Because of the absence of singularity in angular variable at $\rho=0$, g_l is independent of the angular variable. Therefore, in polar coordinates, the equation for g_l reads

$$\frac{1}{\rho}\frac{\partial}{\partial\rho}\left(\rho\frac{\partial g_l}{\partial\rho}\right)-\frac{l^2}{\tilde{L}^2}g_l=\frac{\delta(\rho)}{2\pi\rho},\tag{3.B.3}$$

where we used the ρ-component of the Laplacian. The solution of Equation (3.B.3) can be found by standard technique, and we shall not discuss further. The free-space Green function g_l reads

$$g_l(\eta-\eta',\zeta-\zeta')=-K_0(|l/\tilde{L}|\sqrt{(\eta-\eta')^2+(\zeta-\zeta')^2}),\tag{3.B.4}$$

where K_0 is the modified Bessel function of second kind in zeroth order.

Periodic Solution Since both $\tilde{\phi}_l$ and $\tilde{\sigma}_l$ are periodic in η-direction with period 2π, i.e.,

$$\tilde{\phi}_l(\eta)=\tilde{\phi}_l(\eta+2m\pi,z)\quad\text{and}\quad\tilde{\sigma}_l(\eta)=\tilde{\sigma}_l(\eta+2m\pi),\tag{3.B.5}$$

where $m=0,\pm1,\pm2,\cdots$, we can express $\tilde{\sigma}_l$ as a sum of integrals of period 2π:

$$\tilde{\sigma}_l(\eta)=\int_{-\infty}^{\infty}\delta(\eta-\eta')\tilde{\sigma}_l(\eta')d\eta'\tag{3.B.6}$$

$$=\left(\cdots+\int_0^{2\pi}+\int_{2\pi}^{4\pi}+\int_{4\pi}^{6\pi}+\cdots\right)\delta(\eta-\eta')\tilde{\sigma}_l(\eta')d\eta'.\tag{3.B.7}$$

Using the periodic property of $\tilde{\sigma}_l$, we obtain

$$\tilde{\sigma}_l(\eta) = \int_0^{2\pi} \delta_c(\eta - \eta')\tilde{\sigma}_l(\eta')d\eta', \tag{3.B.8}$$

where the comb function $\delta_c(\eta) = \sum_{m=-\infty}^{\infty} \delta(\eta + 2m\pi)$ is a series of Dirac-delta functions separated by 2π. Substituting Equation (3.B.8) into Equation (3.20) and using the standard properties of Green's function, we obtain the solution of G_l at the mid-plane as Equation (3.22). Finally, the perturbational gravitational potential can be found by Equation (3.B.2).

Chapter 4

Conclusion and Future Work

4.1 Conclusion

In this thesis, we have formulated a theory for the origin of feathers in the spiral arms. We presented the analytic formulation in Chapter 2 and showed that there are unstable growing modes associated with the feathering instability that lead to feather-like substructure in the post-shock region. Such unstable modes cause the enhancement of surface density which vary along the spiral arm. In Chapter 3, we have investigated the dependence of quasi-one-dimensional spiral shock and the feathering instability on the strength of gas self-gravity and other parameters, such as magnetic field. We showed that, in a model of the inner part of M51 galaxy (at 2 kpc from the center), the fast growing mode of the feathering instability in our linear analysis gives a reasonable estimate for the spacing of feather around 500 pc.

The study of the feathering instability allow us to further test the several competing ideas about the spiral structure and its relation to the star formation. In particular, the theory of feathering instability, as an extension from spiral density wave theory with the quasi-static spiral structure (QSSS) hypothesis (Lin & Shu 1964), provides several testable predictions such as the "wave-like" nature of the feathers. The post-shock gas flows that are distorted by the feathers (c.f., Figure 2.7) may have wrongly interpreted as turbulent flow in an insufficiently angularly resolved images of spiral galaxies (Lee & Shu 2012). The calculation of streaming motion can be compared to the measurements at a higher resolution (e.g., Meidt et al. 2013) that assumes a quasi-steady two-arm spiral structure. The dependence of the phase-shift of the gaseous spiral arm versus the stellar spiral arm on the gas surface density may explain the discrepancy between the pitch angle measurements in these arms (e.g., Kendall et al. 2008; Tamburro et al. 2008; Foyle et al. 2011; Louie et al. 2013). However, many of these require a more careful modeling for comparison.

On the other hand, the formation of the feathers and spurs in the spiral galaxies through the feathering instability which is caused by self-gravity provides a different point of view to the problem. Purely hydrodynamic, non-self-gravitating instability found in numerical simulations (e.g., Wada & Koda 2004, which is of Kelvin-Helmholtz type) depends on the strong shear in the post-shock region. This kind of hydrodynamic instability is not included in our analysis and may not be applicable in the case of realistic magnetic field and gas surface density (e.g., Shetty & Ostriker 2006).

4.2 Future Work

The analytic study presented in this thesis provides a theoretical starting point to understand the formation and dynamics of the spiral arm substructure. Although there are unsolved numerical issues, the analytical formulation of feathering instability in principle provides a framework for investigation through other means, such as numerical simulations and simple models for observational comparison.

So far we have only studied the feathering instability by linear analysis. While this approach provides a basic understanding about the onset of the instability, the galactic substructure is very non-linear as suggested in numerous numerical simulations (e.g., formation of gravitationally bounded structure). Therefore, future effort can be put on numerical simulations to recalculate the problem using the formalism developed in this thesis. In particular, we can readily extend the problem for time-dependent linear calculations using standard technique such as method of lines.

Recalculation of the problem can also be done using astrophysical MHD codes that are publicly available for simulating galaxies. In particular, we should recalculate the non-linear development of feathers and spurs to make comparisons between Lee & Shu (2012) and the magnetized version of Balbus (1988) presented in Kim & Ostriker

(2002). Comparisons can also be done among different substructures found in other numerical simulations (e.g., purely hydrodynamical or non-self-gravitating).

Time-dependent linear calculations accompanied with non-linear simulations will be compared to the linear normal mode analysis to find out: 1) whether the fastest growing normal mode of perturbation indeed dominates the dynamics in the later time, and thus gives the periodic substructures of feathers; 2) how the feathers as a density wave move along the spiral arm (e.g., Kim & Ostriker 2002), and how such dynamic picture fits into the observations; 3) what amplitude of such feathering perturbation is expected to find in a real galaxy. In addition, we should also explore possibilities of implementing more realistic equation of state, or gas energy equation, which may be necessary in the spiral arm where the ISM is inhomogeneous and clumpy (e.g., Dobbs 2008).

Appendix A

Derivation of the Equations for Standard Boundary Value Problem Solver

A.1 Introduction

In this appendix, we derive the governing equations for the feathering instability to facilitate the use of numerical boundary value problem (BVP) solvers that are available to the public (e.g., Boisvert et al. 2013). The derivation transforms the differential algebraic equations in the problem (c.f, Section 2.4 in Chapter 2) into the standard form of BVP. The standard form of BVP in this problem consists of a set of ordinary differential equations (ODEs) with separated boundary conditions and a few unknown parameters.

A.2 Equations for the Feathering Perturbation

Following the formulation in Chapter 2, there are four differential equations for the five perturbation variables, $\mathbf{y} = [\tilde{\sigma}, \tilde{u}, \tilde{\mathrm{v}}, \tilde{A}_1, \tilde{A}_1']^{\mathrm{T}}$ (c.f., Appendix 2.A):

$$\mathbf{A}_{\omega,l}\frac{d\mathbf{y}}{d\eta} = \mathbf{B}_{\omega,l}\mathbf{y}, \tag{A.1}$$

where $\mathbf{A}_{\omega,l}$ and $\mathbf{B}_{\omega,l}$ are 4×5 matrices and consist of the coefficients of the variables (c.f., Appendix 2.C). The fifth equation is the ξ-component of the induction equation. However, it is "un-curled" due to the field-freezing condition which allows us to integrate it directly (c.f., Appendix 2.B). Therefore, in order to solve Equation (A.1), we make use of the induction equation to eliminate $\tilde{A}_1''$ on the left-hand side of Equation (A.1). The aim of the procedure is to derive a set of first-order ODEs for $\mathbf{y} = [\tilde{\sigma}, \tilde{u}, \tilde{\mathrm{v}}, \tilde{A}_1]^{\mathrm{T}}$.

A.3 Reduction of Matrices

First, we express $\tilde{A}_1''$ in terms of other perturbational variables by considering the η-component of the induction equation (4th row of Equation (A.1)):

$$u_{\mathrm{T}}\tilde{A}_1' = \sigma_{\mathrm{T}}\tilde{u} - \frac{\kappa}{2\Omega}\tan i\tilde{\mathrm{v}} - i\omega_{\mathrm{T}}\tilde{A}_1, \tag{A.2}$$

where we introduce the following shorthands for clarity: $\sigma_{\mathrm{T}} = 1 + \hat{\sigma}$; $u_{\mathrm{T}} = -\nu + \hat{u}$; $\mathrm{v}_{\mathrm{T}} = -\nu/\tan i + (\kappa/2\Omega)\hat{\mathrm{v}}$, and finally $\omega_{\mathrm{T}} = \omega - (l/\tilde{L})\mathrm{v}_{\mathrm{T}}$. Note that $\mathrm{v}_{\mathrm{T}} \simeq -\nu/\tan i$ under the tight-winding assumption. After taking the η-derivative, we obtain

$$-\sigma_{\mathrm{T}}\tilde{u}' + \frac{\kappa}{2\Omega}\tan i\frac{d}{d\eta}\tilde{\mathrm{v}} + u_{\mathrm{T}}\tilde{A}_1'' = \hat{\sigma}'\tilde{u} + \frac{il}{\tilde{L}}\left(\frac{\kappa}{2\Omega}\right)\sigma_{\mathrm{T}}\tilde{A}_1 - (\hat{u}' + i\omega_{\mathrm{T}})\tilde{A}_1', \tag{A.3}$$

which is the ξ-component of the induction equation. We can eliminate the last term with $\tilde{A}_1'$ by using Equation (A.2):

$$\begin{aligned} &-\sigma_{\mathrm{T}}\tilde{u}' + \frac{\kappa}{2\Omega}\tan i\tilde{\mathrm{v}}' + u_{\mathrm{T}}\tilde{A}_1'' \\ =&\frac{\sigma_{\mathrm{T}}}{u_{\mathrm{T}}}\left(-2\hat{u}' - i\omega_{\mathrm{T}}\right)\tilde{u} + \frac{(\hat{u}' + i\omega_{\mathrm{T}})}{u_{\mathrm{T}}}\frac{\kappa}{2\Omega}\tan i\tilde{\mathrm{v}} + \left[\frac{il}{\tilde{L}}\left(\frac{\kappa}{2\Omega}\right)\sigma_{\mathrm{T}} + i\omega_{\mathrm{T}}\frac{(\hat{u}' + i\omega_{\mathrm{T}})}{u_{\mathrm{T}}}\right]\tilde{A}_1. \end{aligned} \tag{A.4}$$

To systemically to eliminate the fifth column (i.e., $\tilde{A}_1''$ terms) in $\mathbf{A}_{\omega,l}$, we combine Equation (A.4) into Equation (A.1). The corresponding 5×5 matrix for $\mathbf{A}_{\omega,l}$ is

$$\mathcal{A} = \begin{pmatrix} u_{\mathrm{T}} & \sigma_{\mathrm{T}} & 0 & 0 & 0 \\ \hat{b} & u_{\mathrm{T}} & 0 & -x_{\mathrm{A}0}\hat{\sigma}'/\sigma_{\mathrm{T}} & -x_{\mathrm{A}0} \\ 0 & 0 & u_{\mathrm{T}} & 0 & \hat{h}x_{\mathrm{A}0} \\ 0 & 0 & 0 & u_{\mathrm{T}} & 0 \\ 0 & -\sigma_{\mathrm{T}} & \frac{\kappa}{2\Omega}\tan i & 0 & u_{\mathrm{T}} \end{pmatrix}, \tag{A.5}$$

and the corresponding 5×5 matrix for $\mathbf{B}_{\omega,l}$ is

$$\mathcal{B} =$$

$$\begin{pmatrix} -\hat{u}' - i\omega_{\rm T} & -\hat{\sigma}' & i(l/\tilde{L})(\kappa/2\Omega)\sigma_{\rm T} & 0 & 0 \\ 2x_{\rm T0}\hat{\sigma}'/\sigma_{\rm T}^3 & -\hat{u}' - i\omega_{\rm T} & 1 & -x_{\rm A0}(l/\tilde{L})^2 & 0 \\ (2\Omega/\kappa)(il/\tilde{L})\hat{b} & -(1+\hat{\rm v}') & -i\omega_{\rm T} & (2\Omega/\kappa)x_{\rm A0}/\sigma_{\rm T}\left[\tan i(l/\tilde{L})^2 - \hat{\sigma}'(il/\tilde{L})\right] & 0 \\ 0 & \sigma_{\rm T} & -(\kappa/2\Omega)\tan i & -i\omega_T & 0 \\ 0 & \frac{\sigma_{\rm T}}{u_{\rm T}}(-2\hat{u}' - i\omega_{\rm T}) & \frac{(\hat{u}'+i\omega_{\rm T})}{u_{\rm T}}\frac{\kappa}{2\Omega}\tan i & \left[\frac{il}{\tilde{L}}\left(\frac{\kappa}{2\Omega}\right)\sigma_{\rm T} + i\omega_{\rm T}\frac{(\hat{u}'+i\omega_{\rm T})}{u_{\rm T}}\right] & 0 \end{pmatrix}. \tag{A.6}$$

The Gaussian elimination of fifth column of $\mathcal{A}$ can be done by

$$\mathcal{A}_{ij} \to \mathcal{A}_{ij} - \frac{\mathcal{A}_{i5}}{\mathcal{A}_{55}}\mathcal{A}_{5j}, \tag{A.7}$$

where i and j are the indexes for the row and column, respectively. The corresponding matrix $\mathcal{B}$ should be reduced with the same operation:

$$\mathcal{B}_{ij} \to \mathcal{B}_{ij} - \frac{\mathcal{A}_{i5}}{\mathcal{A}_{55}}\mathcal{B}_{5j}. \tag{A.8}$$

Therefore, the reduced matrix for $\mathcal{A}$ is,

$$\begin{pmatrix} u_{\rm T} & \sigma_{\rm T} & 0 & 0 \\ \hat{b} & u_{\rm T} - x_{\rm A0}\frac{\sigma_{\rm T}}{u_{\rm T}} & \frac{\kappa}{2\Omega}\tan i\frac{x_{\rm A0}}{u_{\rm T}} & -x_{\rm A0}\hat{\sigma}'/\sigma_{\rm T} \\ 0 & \frac{2\Omega}{\kappa}x_{\rm A0}\frac{\tan i}{u_{\rm T}} & u_{\rm T} + \tan^2 i/\nu & 0 \\ 0 & 0 & 0 & u_{\rm T} \end{pmatrix}, \tag{A.9}$$

where we hide the redundant fifth row and fifth column. Since $\mathcal{A}_{15} = \mathcal{A}_{45} = 0$ in Equation (A.5), the first and fourth rows of reduced $\mathcal{B}$ remain the same. We only list the modified entries of the matrix $\mathcal{B}$:

$$\mathcal{B}_{22} = -\hat{u}' - i\omega_{\mathrm{T}} + \frac{x_{\mathrm{A0}}\sigma_{\mathrm{T}}}{u_{\mathrm{T}}^2}\left(-2\hat{u}' - i\omega_{\mathrm{T}}\right), \tag{A.10}$$

$$\mathcal{B}_{23} = 1 + x_{\mathrm{A0}}\frac{(\hat{u}' + i\omega_{\mathrm{T}})}{u_{\mathrm{T}}^2}\frac{\kappa}{2\Omega}\tan i, \tag{A.11}$$

$$\mathcal{B}_{24} = -x_{\mathrm{A0}}\left(\frac{l}{\tilde{L}}\right)^2 - \frac{x_{\mathrm{A0}}}{u_{\mathrm{T}}}\left[\left(\frac{il}{\tilde{L}}\right)\left(\frac{\kappa}{2\Omega}\right)\sigma_{\mathrm{T}} + i\omega_{\mathrm{T}}\frac{(\hat{u}' + i\omega_{\mathrm{T}})}{u_{\mathrm{T}}}\right], \tag{A.12}$$

$$\mathcal{B}_{32} = -\sigma_{\mathrm{T}} - \frac{2\Omega}{\kappa}\frac{x_{\mathrm{A0}}}{u_{\mathrm{T}}^2}\left(-2\hat{u}' - i\omega_{\mathrm{T}}\right)\tan i, \tag{A.13}$$

$$\mathcal{B}_{33} = -i\omega_{\mathrm{T}} - \frac{x_{\mathrm{A0}}}{-\nu}\frac{(\hat{u}' + i\omega_{\mathrm{T}})}{u_{\mathrm{T}}}\tan^2 i, \tag{A.14}$$

$$\mathcal{B}_{34} = \left(\frac{2\Omega}{\kappa}\right)\frac{x_{\mathrm{A0}}}{\sigma_{\mathrm{T}}}\left[\tan i\left(\frac{l}{\tilde{L}}\right)^2 - \hat{\sigma}'\frac{il}{\tilde{L}}\right] - \frac{2\Omega}{\kappa}\frac{x_{\mathrm{A0}}}{\sigma_{\mathrm{T}}}\left[\frac{il}{\tilde{L}}\left(\frac{\kappa}{2\Omega}\right)\sigma_{\mathrm{T}} + i\omega_{\mathrm{T}}\frac{(\hat{u}' + i\omega_{\mathrm{T}})}{u_{\mathrm{T}}}\right]\frac{\tan i}{u_{\mathrm{T}}}. \tag{A.15}$$

Using the reduced matrix $\mathcal{A}$ and $\mathcal{B}$, the governing equation becomes

$$\mathcal{A}(\eta)\frac{d}{d\eta}\mathbf{y}(\eta) = \mathcal{B}(\eta)\mathbf{y}(\eta), \tag{A.16}$$

where $\mathbf{y} = [\tilde{\sigma}, \tilde{u}, \tilde{\mathrm{v}}, \tilde{A}_1]^{\mathrm{T}}$ is a vector of perturbational variables. This equation is subject to the boundary conditions for the perturbational shock jump conditions.

A.4 Boundary Conditions

In the normalized form, the boundary conditions read

$$[(1 + \hat{\sigma})\delta u + (-\nu + \hat{u})\delta\sigma]_1^2 = 0, \tag{A.17}$$

$$\left[(-\nu + \hat{u})^2\delta\sigma + 2(1 + \hat{\sigma})(-\nu + \hat{u})\delta u + \left(\frac{x_{\mathrm{T0}}}{1 + \hat{\sigma}}\right)\delta\sigma + x_{\mathrm{A0}}(1 + \hat{\sigma})\left(\frac{\delta B_{\parallel}}{B_{\xi 0}}\right)\right]_1^2 = 0, \tag{A.18}$$

$$\begin{aligned}&\left[(-\nu + \hat{u})v_{\mathrm{T}}\delta\sigma + (1 + \hat{\sigma})(-\nu + \hat{u})\frac{\kappa}{2\Omega}\delta\mathrm{v}\right.\\ &\left.+(1 + \hat{\sigma})v_{\mathrm{T}}\delta u - x_{\mathrm{A0}}\tan i\left(\frac{\delta B_{\parallel}}{B_{\xi 0}}\right) - x_{\mathrm{A0}}(1 + \hat{\sigma})\left(\frac{\delta B_{\perp}}{B_{\xi 0}}\right)\right]_1^2 = 0,\end{aligned} \tag{A.19}$$

$$[\delta B_{\perp}]_1^2 = 0, \tag{A.20}$$

$$\left[\frac{B_{\perp}}{B_{\xi 0}}\frac{\kappa}{2\Omega}\delta\mathrm{v} - \frac{B_{\parallel}}{B_{\xi 0}}\delta u + \frac{\kappa}{2\Omega}\hat{v}_0\frac{\delta B_{\perp}}{B_{\xi 0}} - \hat{u}_0\frac{\delta B_{\parallel}}{B_{\xi 0}}\right]_1^2 = 0, \tag{A.21}$$

where the δ variables are Lagrangian variables defined by

$$\delta\sigma = \tilde{\sigma} + \epsilon\hat{\sigma}', \tag{A.22}$$

$$\delta u = \tilde{u} + \epsilon\hat{u}' - i\omega_{\mathrm{T}}\epsilon, \tag{A.23}$$

$$\delta \mathrm{v} = \tilde{\mathrm{v}} + \epsilon\hat{\mathrm{v}}' - \frac{2\Omega}{\kappa} il\hat{u}\epsilon, \tag{A.24}$$

$$\delta B_{\perp}/B_{\xi 0} = -il\tilde{A}_1 + il(1+\hat{\sigma})\epsilon, \tag{A.25}$$

$$\delta B_{\parallel}/B_{\xi 0} = -\tilde{A}_1' + \epsilon\hat{\sigma}' + \frac{\kappa}{2\Omega}\frac{\hat{\sigma}}{-\nu}\tan i\epsilon - il\tan i\epsilon. \tag{A.26}$$

Consistent with our formulation for the differential equations, we use δA and $\delta A'$ in place of $\delta B_{\perp}$ and $\delta B_{\parallel}$, respectively. They are defined by

$$\delta A = \tilde{A}_1 - (1+\hat{\sigma})\epsilon, \tag{A.27}$$

$$\delta A' = \tilde{A}_1' - \left[\hat{\sigma}' - \frac{\kappa}{2\Omega}\frac{\hat{\sigma}}{-\nu}\tan i + il\tan i\right]\epsilon. \tag{A.28}$$

The boundary conditions (A.17)-(A.21) can be written as

$$\mathbf{Q}_1\tilde{Y}_1 + \boldsymbol{\beta}_1\epsilon = \mathbf{Q}_2\tilde{Y}_2 + \boldsymbol{\beta}_2\epsilon, \tag{A.29}$$

where $\mathbf{Q}$ is a 4×4 matrix depending on background variables, $\tilde{Y} = [\tilde{\sigma}, \tilde{u}, \tilde{\mathrm{v}}, \tilde{A}_1]^{\mathrm{T}}$ is a vector of perturbational variables and $\boldsymbol{\beta}$ is a constant vector. There are only four equations because we can eliminate the $\tilde{A}'$ terms using the Fourier-transformed equation (c.f., Equation (A.2)):

$$u_{\mathrm{T}}\tilde{A}_1' = \sigma_{\mathrm{T}}\tilde{u} - \frac{\kappa}{2\Omega}\tan i\tilde{\mathrm{v}} - i\omega_{\mathrm{T}}\tilde{A}_1, \tag{A.30}$$

and we have already shown that the last two boundary conditions are consistent with the induction equation for both sides of the shock separately. To obtain $\mathbf{Q}$, we perform the similar reduction procedure as in the last section. After some algebra, we get $\mathbf{Q}$ in the following form:

$$\begin{pmatrix} u_{\mathrm{T}} & \sigma_{\mathrm{T}} & 0 & 0 \\ u_{\mathrm{T}}^2 + x_{\mathrm{T}0}/\sigma_{\mathrm{T}} & -2\nu - x_{\mathrm{A}0}\frac{\sigma_{\mathrm{T}}^2}{u_{\mathrm{T}}} & \frac{\kappa}{2\Omega}\tan i x_{\mathrm{A}0}\frac{\sigma_{\mathrm{T}}}{u_{\mathrm{T}}} & i\omega_{\mathrm{T}}x_{\mathrm{A}0}\frac{\sigma_{\mathrm{T}}}{u_{\mathrm{T}}} \\ 0 & x_{\mathrm{A}0}\tan i\frac{\sigma_{\mathrm{T}}}{u_{\mathrm{T}}} & -\frac{\kappa}{2\Omega}\left(\nu + x_{\mathrm{A}0}\tan^2 i/u_{\mathrm{T}}\right) & x_{\mathrm{A}0}\left(\frac{il}{L}\sigma_{\mathrm{T}} + i\omega_{\mathrm{T}}\tan i/u_{\mathrm{T}}\right) \\ 0 & 0 & 0 & 1 \end{pmatrix}, \tag{A.31}$$

in which it is to be evaluated at the both sides of the shock. Next, we identify the vector $\boldsymbol{\beta}$ with the coefficient of ϵ in the boundary conditions (A.17) - (A.20). Thus, we have

$$\boldsymbol{\beta} = \begin{pmatrix} \sigma_{\mathrm{T}}\hat{u}' + u_{\mathrm{T}}\hat{\sigma}' - i\sigma_{\mathrm{T}}\omega_{\mathrm{T}} \\ \left[u_{\mathrm{T}}^2 + \frac{x_{\mathrm{T0}}}{\sigma_{\mathrm{T}}} + x_{\mathrm{A0}}\sigma_{\mathrm{T}}\right]\hat{\sigma}' - 2\nu\hat{u}' + 2i\nu\omega_{\mathrm{T}} \\ -x_{\mathrm{A0}}\tan i\hat{\sigma}' - \frac{\kappa}{2\Omega}\nu\hat{\sigma} + il\nu\hat{u} - ilx_{\mathrm{A0}}\sigma_{\mathrm{T}}^2 \\ \sigma_{\mathrm{T}} \end{pmatrix} = \begin{pmatrix} -i\sigma_{\mathrm{T}}\omega_{\mathrm{T}} \\ -\left[u_{\mathrm{T}}^2 - \frac{x_{\mathrm{T0}}}{\sigma_{\mathrm{T}}} - x_{\mathrm{A0}}\sigma_{\mathrm{T}}\right]\hat{\sigma}' + 2i\nu\omega_{\mathrm{T}} \\ -x_{\mathrm{A0}}\tan i\hat{\sigma}' - \frac{\kappa}{2\Omega}\nu\hat{\sigma} + il\nu\hat{u} - ilx_{\mathrm{A0}}\sigma_{\mathrm{T}}^2 \\ \sigma_{\mathrm{T}} \end{pmatrix}, \tag{A.32}$$

where the relations of background variables are used to simplify the expression. Again, the vector is to be evaluated for both sides of the shock front.

A.5 Summary

Equation (A.16) with the boundary conditions (A.29) is a set of first-order ODEs that permits the use of standard BVP solver.

Bibliography

Ascher, U. M., Mattheij, R., & Russell, R. D. 1995, Numerical Solution of Boundary Value Problems for Ordinary Differential Equations (Philadelphia, PA: SIAM)

Balbus, S. A. 1988, ApJ, 324, 60

Block, D. L., Bertin, G., Stockton, A., Grosbol, P., Moorwood, A. F. M., & Peletier, R. F. 1994, A&A, 288, 365

Block, D. L., Elmegreen, B. G., & Wainscoat, R. J. 1996, Nature, 381, 674

Block, D. L., & Wainscoat, R. J. 1991, Nature, 353, 48

Boisvert, J. J., Muir, P. H., & Spiteri, R. J. 2013, ACM Trans. Math. Softw., 39, 11:1

Chakrabarti, S., Laughlin, G., & Shu, F. H. 2003, ApJ, 596, 220

Corder, S., Sheth, K., Scoville, N. Z., Koda, J., Vogel, S. N., & Ostriker, E. 2008, ApJ, 689, 148

Dobbs, C. L. 2008, MNRAS, 391, 844

Dobbs, C. L., & Bonnell, I. A. 2006, MNRAS, 367, 873

D'Onghia, E., Vogelsberger, M., & Hernquist, L. 2013, ApJ, 766, 34

Dwarkadas, V. V., & Balbus, S. A. 1996, ApJ, 467, 87

Elmegreen, B. G. 1994, in Astronomical Society of the Pacific Conference Series, Vol. 66, Physics of the Gaseous and Stellar Disks of the Galaxy, ed. I. R. King, 61

Elmegreen, D. M. 1980, ApJ, 242, 528

Foyle, K., Rix, H.-W., Dobbs, C. L., Leroy, A. K., & Walter, F. 2011, ApJ, 735, 101

Goldreich, P., & Lynden-Bell, D. 1965, MNRAS, 130, 125

Julian, W. H., & Toomre, A. 1966, ApJ, 146, 810

Kendall, S., Kennicutt, R. C., Clarke, C., & Thornley, M. D. 2008, MNRAS, 387, 1007

Kim, W., & Ostriker, E. C. 2002, ApJ, 570, 132

Kim, W.-T., & Ostriker, E. C. 2006, ApJ, 646, 213

La Vigne, M. A., Vogel, S. N., & Ostriker, E. C. 2006, ApJ, 650, 818

Lee, W.-K., & Shu, F. H. 2012, ApJ, 756, 45

Lin, C. C., & Shu, F. H. 1964, ApJ, 140, 646

Lizano, S., & Shu, F. H. 1989, ApJ, 342, 834

Louie, M., Koda, J., & Egusa, F. 2013, ApJ, 763, 94

Lubow, S. H., Cowie, L. L., & Balbus, S. A. 1986, ApJ, 309, 496

Lynds, B. T. 1970, in IAU Symp. 38, The Spiral Structure of our Galaxy, ed. W. Becker & G. I. Kontopoulos (Cambridge: Cambridge Univ. Press), 26

Mathewson, D. S., van der Kruit, P. C., & Brouw, W. N. 1972, A&A, 17, 468

Meidt, S. E., et al. 2013, ArXiv e-prints

Mouschovias, T. C., Shu, F. H., & Woodward, P. R. 1974, A&A, 33, 73

Parker, E. N. 1969, Space Science Reviews, 9, 651

Piddington, J. H. 1973, ApJ, 179, 755

Roberts, W. W. 1969, ApJ, 158, 123

Roberts, Jr., W. W., & Yuan, C. 1970, ApJ, 161, 887

Scoville, N., & Rector, T. 2001, HST Press Release

Sellwood, J. A. 2012, ApJ, 751, 44

Shetty, R., & Ostriker, E. C. 2006, ApJ, 647, 997

Shu, F. H. 1992, The physics of astrophysics. Volume II: Gas dynamics. (Mill Valey, CA: Univ. Sci. Books)

Shu, F. H., Allen, R. J., Lizano, S., & Galli, D. 2007, ApJL, 662, L75

Shu, F. H., Milione, V., & Roberts, W. W. 1973, ApJ, 183, 819

Sofue, Y., Tutui, Y., Honma, M., Tomita, A., Takamiya, T., Koda, J., & Takeda, Y. 1999, ApJ, 523, 136

Spitzer, Jr., L. 1968, in Dynamics of Interstellar Matter and the Formation of Stars, ed.

B. M. Middlehurst & L. H. Aller (Chicago, IL: Univ. Chicago Press), 1

Tamburro, D., Rix, H.-W., Walter, F., Brinks, E., de Blok, W. J. G., Kennicutt, R. C., & Mac Low, M.-M. 2008, AJ, 136, 2872

Wada, K., & Koda, J. 2004, MNRAS, 349, 270

Westpfahl, D. J. 1998, ApJS, 115, 203